The Interactions of Graphene with Ionic Solutions and Their Effects on the Differential Capacitance for Sensing Applications

by

Lindsey M. Daniels

A thesis
presented to the University of Waterloo
in fulfillment of the
thesis requirement for the degree of
Doctor of Philosophy
in
Applied Mathematics

Waterloo, Ontario, Canada, 2019

Examining Committee Membership

The following served on the Examining Committee for this thesis. The decision of the Examining Committee is by majority vote.

Supervisors: Zoran Mišković
Professor, Department of Applied Mathematics
University of Waterloo

Matthew Scott
Associate Professor, Department of Applied Mathematics
University of Waterloo

Internal Member: Edward R. Vrscay
Professor, Department of Applied Mathematics
University of Waterloo

Mohammad Kohandel
Associate Professor, Department of Applied Mathematics
University of Waterloo

Internal-External Member: Mark Pritzker
Professor, Department of Chemical Engineering
University of Waterloo

External Examiner: Mahi R. Singh
Professor, Department of Physics
Western University

Abstract

Nano-scale devices continue to challenge the theoretical understanding of microscopic systems. Of particular interest is the characterization of the interface electrochemistry of sensors, which operate as field effect transistors with graphene in contact with the solution. While plenty of experimental research has been conducted in regard to the viability and sensitivity of graphene-based devices, the understanding of the microscopic and macroscopic physics of these sensors has lagged, unlike any other areas of applications for graphene. Although some successful models of these sensors have been developed, relatively little theoretical work to account for the vast extent of experimental work.

Typically operated in a regime of high ion concentration and high surface charge density, dielectric saturation, dielectric decrement, and ion crowding become non-negligible at the interface, complicating continuum treatments based upon the Poisson-Boltzmann equation. Modifications to the standard Poisson-Boltzmann theory are explored, with modifications due to dielectric saturation and dielectric decrement considered in tandem with a Bikerman-Friese model to account for the steric effects of ions. In the case of dielectric saturation, a model proposed by Booth is used to characterize the diffuse layer capacitance for both metallic and graphene electrodes immersed in an electrolyte. The dependence of the diffuse layer capacitance on the surface charge density of the electrode exhibits two peaks, in contrast to the experimental results. For dielectric decrement, a dielectric permittivity dependent on the concentration of positive and negative ions is used to determine the diffuse layer capacitance for both metallic and graphene electrodes. The diffuse layer capacitance shows a strong interplay between ion polarizability and steric effects, while exhibiting a single peak. A self-consistent and parameter-free method for the inclusion of a Stern layer is used in both cases, which eliminates the spurious secondary peak in the case of dielectric saturation and reduces the overall magnitude of the capacitance of the diffuse layer in both dielectric saturation and dielectric decrement. When a graphene electrode is used, the total capacitance in all modifications is dominated by V-shaped quantum capacitance of graphene at low potentials, which is a manifestation of the Dirac cone structure of the graphene π-electron bands. A broad peak develops in the total capacitance at high potentials, which is sensitive to the ion size at dielectric saturation, but is stable with dielectric decrement.

In addition to the interactions of graphene with an electrolyte, considerable interest has recently been shown in studying the electric double layer that arises at the interface of doped graphene and a class of electrolytes known as ionic liquids. Ionic liquids are a class of molten ionic salts at room temperature that have low volatility and high ionic concentration, and are characterized by the overscreening and overcrowding effects in their electric double layer. A mean field model for ionic liquids is presented, which takes into account both the ion correlation and the finite ion size effects, in order to calculate the differential capacitance of the ionic liquid interface with single-layer graphene. Besides choosing ion packing fractions that give rise to the camel-shaped and bell-shaped capacitances of the diffuse layer in ionic liquids, the regimes of "dilute electrolytes" and asymmetric ionic liquids are considered. As in the case of electrolytes, the main effect of a graphene electrode arises due to its V-shaped quantum capacitance. As a result, the total capacitance of a graphene–ionic liquid interface exhibits a camel-shaped dependence on the total applied potential, even for large ion packing fractions and finite ion correlation lengths. While the minimum at the neutrality point in the total capacitance is "inherited" from the quantum capacitance of graphene, the two peaks that occur at applied potentials of $\sim \pm 1$ V are sensitive to the presence of the ion correlation and a Stern layer, which both tend to reduce the height and flatten the peaks in the camel-shaped total capacitance. It is also determined that the largest fraction of the applied potential goes to charging the graphene electrode.

When considering the sensitivity of graphene-based sensors to ion concentration and/or pH of the surrounding environment, a site binding model which allows hydrogen and hydroxyl groups to adsorb onto the surface of the device is proposed. Both a regime in which bare graphene is exposed to the electrolyte and a regime where a functionalized oxide, which contains a density of charged impurities to facilitate ion binding, is situated between graphene and the electrolyte are proposed. With regard to the dependence on ion concentration, comparisons between the model and experimental data show good agreement when the finite size of ions is included in the electrolyte. In the case of pH dependence, comparisons between the model and experimental data show excellent agreement, particularly when steric effects are included in the electrolyte. The favourable comparisons here are the first steps in developing a comprehensive model of graphene based biological and chemical sensors.

Acknowledgements

Thank you to my supervisors Dr. Zoran Mišković and Dr. Matt Scott. This thesis would not have been possible without your expertise, guidance, support, and patience over these last five years, and I am grateful to you both for this journey. Thank you to my Applied Math committee members Dr. Edward Vrscay and Dr. Mohammad Kohandel, who always made time for me when I had questions, particularly when I was studying for my comprehensive exam. Thank you both for all your time, and helpful comments, over the course of my PhD. Thank you to Dr. Mark Pritzker and Dr. Mahi Singh for agreeing to serve on my PhD committee, and your time and consideration when reading this thesis.

Over the last five years, I have had the pleasure of working with several undergraduate students at UW. Thank you to Narsimha Chilkuri, Ahmed Shalabi, Kieana Fana, and Jiangfeng Ding for all your hard work and dedication. You all had a hand in parts of this thesis, and I am grateful to have worked with each of you.

I would also like to thank all of my friends and colleagues in the Applied Math department and at UW for all the advice and enlightening discussions: you all made grad school that much more enjoyable. Thank you to all my friends back home in Thunder Bay who encouraged me and are always there to listen when things were not easy.

Last, but certainly not least, thank you to my family for all their love, support, and encouragement throughout my PhD. You have always supported me through any endeavours I chose to take on, no matter how big or small, and I am very grateful to have such an amazing family.

Table of Contents

List of Tables

List of Figures

List of Acronyms

B	Dielectric Saturation Model via the Booth Model
B+S	Dielectric Saturation Model via the Booth Model with Steric Effects
CVD	Chemical Vapour Deposition
D	Dielectric Decrement Model
D+S	Dielectric Decrement Model with Steric Effects
DH	Debye-Hückel Model
EDL	Electric Double Layer
FET	Field Effect Transistor
IHP	Inner Helmholtz Plane
ISFET	Ion Sensitive Field Effect Transistor
OHP	Outer Helmholtz Plane
PB	Poisson-Boltzmann model
S	Steric Effects model

List of Symbols

a_i	Diameter size of ith ion
α	Ion polarization
α_{fine}	Effective fine structure constant
β	Inverse product of Boltzmann constant and temperature
BZ	Brillouin zone
C_i	Capacitance of ith layer
C_D	Debye capacitance
C^{∞}	High potential capacitance
$c_{\pm}$	Positive/negative ion concentration
c_{∞}	Bulk concentration
δ	Ratio of dissociation constants
δ_c	Dimensionless ion correlation length for ionic liquid
e	Elementary charge
E	Electric field
ε	Band energy
ε_D	Dirac point energy
ϵ_w	Dielectric permittivity of water
ϵ_{Booth}	Dielectric permittivity due to Booth model
ϵ_{dec}	Dielectric permittivity due to dielectric decrement
F	Free energy
$\gamma_{\pm}$	Packing fraction of positive/negative ions
γ_{sat}	Dielectric saturation
h	Thickness of Stern layer
$\hbar$	Reduced Planck's constant
k_B	Boltzmann constant
K_i	Dissociation constant of ith reaction
ℓ_c	Ionic liquid correlation length

λ_B	Bjerrum length
λ_D	Debye screening length
n	Refractive index of water
n_c	Electrode charge
N_S	Number of binding sites
ν	Bulk volume fraction of ions
ϕ	Potential
ϕ_N	Nernst potential
ρ	Charge density
S	Entropy
σ_i	Surface charge density on ith surface
T	Temperature
t	Oxide thickness
U	Internal energy
μ	Chemical potential
V	Potential drop
v_F	Fermi speed
w_e	Self-energy of electric field
z_i	Valence charge on ith ion

Chapter 1

Introduction

1.1 Motivation

The miniaturization of technology has given rise to the need for more compact, highly efficient materials. Initial efforts to scale down electrical devices saw highly doped silicon as a preferred and promising material [1]. However, as the interest in applications to medicine and biology grew, it became evident that doped silicon would not be a viable material due to its chemical instability and reactivity with some electrolytic solutions [1, 2, 3]. In an effort to bridge the gap between nanoscale sensors and their potential biological and chemical applications, new materials were sought out which would be chemically stable and not corrode or react with the local environment.

One such material which shows great promise is the 2-dimensional material of graphene. Graphene is a single layer lattice of hexagonally bonded carbon atoms, and therefore, the thinnest material in existence [4, 5]. Its unique band and crystal structure give it some distinctive characteristics. Graphene has a high charge carrier density and high thermal and electrical conductivity. Coupled with its thinness and flexibility, this makes it an ideal material for nanoscale electronic devices such as solar cells, light emitting diodes, and wearable technology where graphene is intertwined with fabric [1, 4, 5, 6, 7, 8, 9]. Due to its strong non-linear optical conductance, graphene is also a popular material in the fabrication of terahertz detectors and emitters in defence telecommunications and technology [10, 11].

A significant technological and manufacturing issue with silicon-based electronic devices is their chemical instability in some environments, as well as their lack of flexibility [1]. Unlike many metallic electrodes, graphene is a chemically inert, flexible material [1, 5, 6].

Therefore, in recent years, graphene has risen to be one of the key materials of interest in the development of nanoscale biological and chemical sensors [12, 13, 14, 15]. Graphene-based sensors show great promise in their ability to accurately detect changes to their environment, such as specific concentrations of molecules of interest or to acidity [16, 17, 18, 19, 20, 21], which makes them ideal for future applications in medicine, chemistry, and biology.

Perhaps the application of most interest is as a biomedical sensor, where graphene acts as the conducting channel in a field-effect-transistor (FET), in contact with an aqueous solution containing mobile charged ions [1, 22]. A transistor is an electronic device that utilizes the unique properties of semiconductors to amplify or switch electrical power or signals. Transistors are three-terminal devices, having a source, drain and back gate terminal, where the current between the source and drain can be controlled by small changes in the voltage of the back gate [23]. A special type of transistor which uses electrons and holes for conduction is referred to as an FET, which is voltage-controlled and has a high input impedance, so that it uses a relatively small amount of current [24].

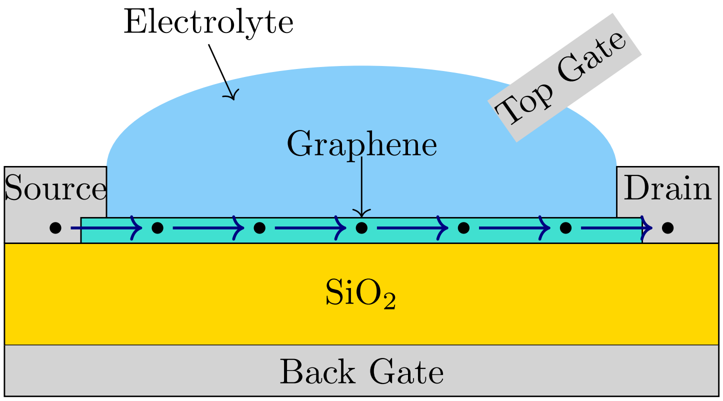

Figure 1.1: Model of a graphene electrolyte FET. Adapted from [22, 25].

In a graphene FET (Figure 1.1), a single layer of graphene is placed on top of an insulator, in this case silicon dioxide (SiO_2), and a source is connected to one end and a drain to the other. A back gate is also placed on the other side of the insulator. This silicon dioxide layer makes the input impedance of the FET much higher than a normal FET [24]. When a potential difference is applied, graphene acts as a conducting channel between the source and drain, due to the high mobility of its π electrons [26].

Graphene-based FETs have been shown to be more efficiently controlled by an electrochemical gate immersed in a solution than by a typical metal back gate through an insulating oxide layer (e.g. SiO_2) [19, 27]. Ohno *et al.* showed experimentally that the gate voltage necessary for electrolytically gating graphene-based FETs was on the order of −0.5 to 0.5 V, whereas their back gating counterparts required −40 to 40 V to produce a full conductance curve (Figure 1.2). When the gate voltage is applied, an electric double layer (EDL) forms at the graphene-solution interface due to the presence of ions [28]. This EDL can vary in thickness due to the concentration of electrolyte, and may only be a few nanometers thick. Nevertheless, it can still shield the graphene channel and may result in the capacitance of the EDL being larger than that of the back gate [28]. Therefore, electrochemical gating gives more control over the graphene surface potential [19]. The applied voltage results in a shift in the minimum of the graphene conductance, due to a change in its chemical potential. It is this shift in the conductance that is used to measure the ion concentration or pH of the solution [1, 12, 19, 21, 22].

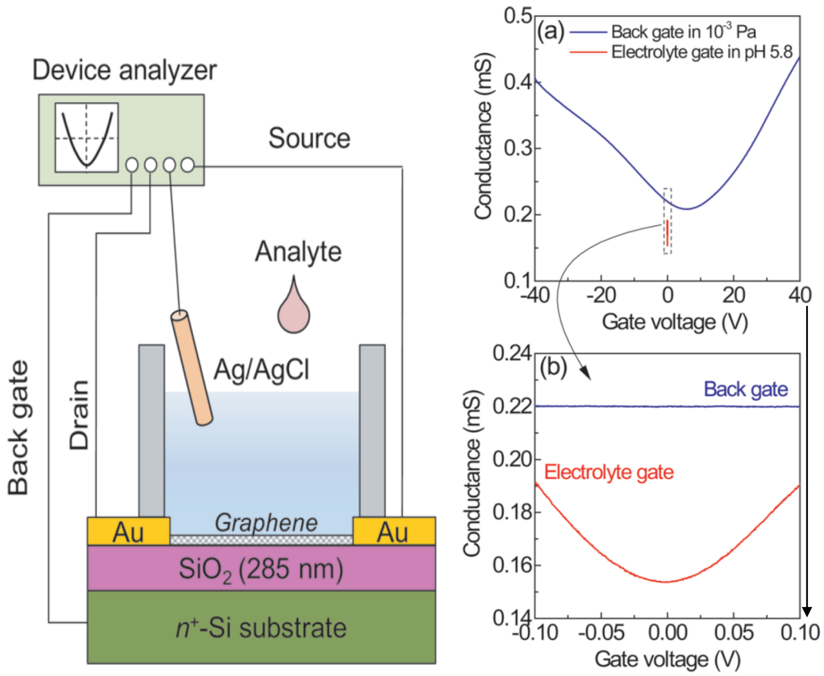

Figure 1.2: Comparison of the electrolytic and back gating of a graphene-based sensor. Experiments confirm that electrolyically gating graphene FETs is more efficient than the typical back gating. Adapted from [27].

When a graphene FET is operated in capacitance mode, experiments show the device is more sensitive to changes in ion concentration and/or the pH of the surrounding solution

[29]. This is attributed to the fact that the so-called quantum capacitance of graphene (defined in Chapter 2) is much smaller than the capacitance of the electrolyte, and therefore dominates the system [28, 30] unlike its metallic electrode counterpart. Thus, the capacitance mode of a graphene-based FETs has become the focus of experimental work.

Experimental work measuring the dependence of the capacitance on pH has shown conflicting results (Figure 1.3). Some groups claim that graphene is highly sensitive to pH, with a sensitivity of approximately 100 meV/pH [27, 31], which is almost twice the Nernstian maximum allowed shift of 59 meV/pH (Figure 1.4). Other groups claim that the behaviour of clean, defect-free graphene is insensitive to pH, and that atomic defects or impurities in graphene give rise to the observed effects [21, 32, 33]. Therefore a functionalized layer or aromatic molecules may be used to help enhance the dependance on pH [32]. In either case, the sensitivity of the configuration is driven by the binding of protons (H^+) to the surface of either graphene or a functionalized graphene [34, 35, 36] and results in an adsorption layer on the interface, which can affect the surface potential depending on the extent of adsorption [34, 35, 36].

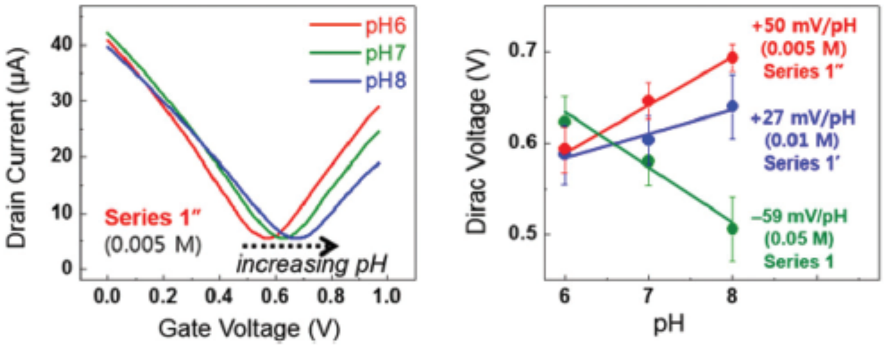

Figure 1.3: Shift in the conductivity minimum due to increasing pH at three different concentration settings. Here, solutions of sodium hydroxide (NaOH), hydrochloric acid (HCl), and potassium hydroxide (KOH) were used to tune the pH in the experiment. Adapted from [20].

When measuring the ion concentration (Figure 1.4), experimental work has shown that the conductivity and capacitance of graphene are dependent on the ion concentration of the electrolyte [37]. As the concentration is increased, the shift from a gate voltage of zero is reduced [17, 38]. Experimental work has also suggested that sensitivity to ion concentration may be dependent on the type of liquid gate electrode used. Some electrodes exhibit little to no sensitivity, while others are much more sensitive [20], see Figure 1.4 b).

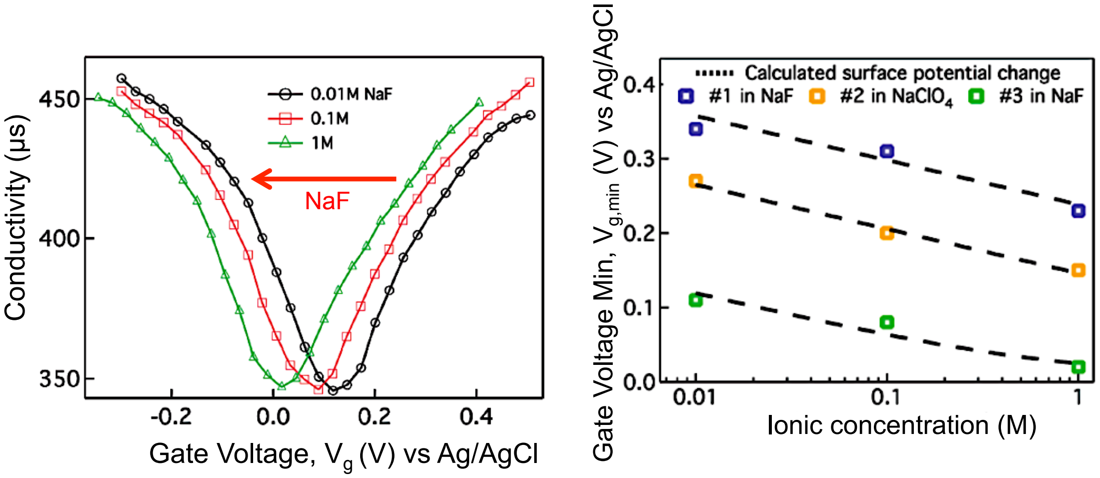

(a) Shift in the conductivity minimum due to different ion concentrations of sodium fluoride (NaF). The sensitivity, or slope, of the minima are fairly consistent for different sodium solutions. Left shows the full conductivity curves and right shows the shift in the minimum point of the conductance. Adapted from [30].

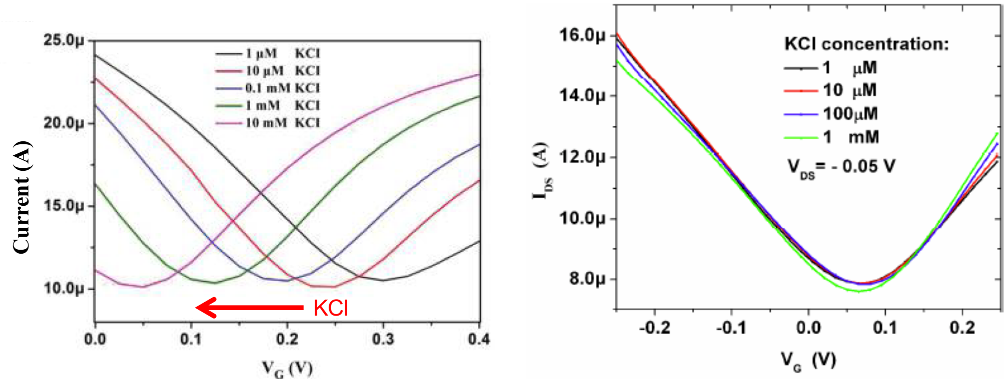

(b) Left: shift in the conductivity when an Ag/AgCl gate is used. Right: Shift in the conductivity when a Gold gate is used. Note how the sensitivity is dependent on the type of gate used, where a gold gate yields relatively no shift in the minimum. Adapted from [38].

Figure 1.4: The shifts in conductivity and capacitance for increasing concentrations of sodium fluoride, NaF, and potassium chloride, KCl, for two experimental groups.

While the interest in of experimental research on the viability and sensitivity of graphene-based devices has surged, relatively little theoretical work on the microscopic and macroscopic physics of these sensors has been reported, which is unlike any other areas of applications for graphene [12, 13, 14]. While some successful models have been reported [25, 39, 40, 41], much of the experimental work has yet to be theoretically modelled. Without a full theoretical understanding of the role graphene plays in these sensors, the development and implementation of these devices has been delayed.

In addition to promising biomedical application, graphene-based devices have been contacted with room temperature ionic liquids [37]. Ionic liquids are chemically stable, chemically inert, and have a Debye screening length of approximately zero [37]. They show great promise in solar cells [42], supercapacitors [43, 44, 45, 46], and gates [47]. Experimental work shows that the capacitance of these devices has a similar shape to those found when immersed in aqueous solutions [30, 37]. Also, the minimum in the capacitance shifts with increasing ion concentration [37]. The EDL that arises in an ionic liquid has shown effects of ion crowding and overscreening [48, 49]. Models of the EDL that account for ion crowding and overscreening have been reported [48, 49], but the interactions between an ionic liquid and graphene have yet to be described.

One possibility for the lag in theoretical understanding could be due to the interdisciplinary nature of the problem. A successful theoretical model must tie together concepts from chemistry, electrochemistry, engineering, solid state physics, and quantum mechanics, as well as the mathematical analysis tools to bridge the fields. In an effort to understand how these areas contribute to the overall theoretical modelling, it is useful to note some preliminary topics which will be the basis for discussion in later chapters.

1.2 Electrolytic Solutions

In the configuration of electrochemical sensors, the conducting channel (or graphene) is directly in contact with a solution which contains mobile ions (or charges). A build of up ions at the solution-graphene interface, which is referred to as the electric double layer (EDL), occurs when an applied potential is passed through the FET due to charge attractions/repulsions (Figure 1.5). Some models to describe the structure of the EDL will be briefly explored below [28]. It is worthwhile to note that it is necessary to have a reference electrode for electrochemical experiments, which has a known potential, in order to be able to experimentally measure quantities in the system (e.g. overall potential) [28], and therefore, many experimental results are reported with respect to some reference electrode.

Perhaps the first formal attempt at modelling the EDL was made by Helmholtz [50]. He proposed that that counter-charge species in the solution also exist at the interface of the electrode, forming two oppositely charged layers separated by a small distance, called the EDL. This configuration is similar to that of a parallel-plate capacitor, with a charge density of the EDL: $\sigma = \frac{\epsilon\epsilon_0}{d}V$, where V is the voltage drop between the charged surfaces, ϵ is the dielectric constant of the medium between the charged surfaces, ϵ_0 is the permittivity of free space, and d is the spacing between the charged surfaces. The Helmholtz model unfortunately predicts a constant differential capacitance, $C_d = \frac{\partial\sigma}{\partial V} = \frac{\epsilon\epsilon_0}{d}$. For real systems, it has been shown that the differential capacitance varies with potential and concentration changes [28].

One of the modifications to the model proposed by Helmholtz was the inclusion of a diffuse layer proposed by Gouy and Chapman [51, 52]. In this diffuse layer, the greatest concentration of excess charge would be at the electrode and the concentration of excess charge would decay as the distance away from the electrode increases. Thus, a model would need to include an average distance of separation, which would be dependent on potential and electrolyte concentration (since an increase in electrolyte concentration and a more highly charged electrode would cause the diffuse layer to decrease in size). This model is more successful than the Helmholtz model at predicting the differential capacitance of the system as it predicts the correct shape of the capacitance; however, experimental measurements show that the capacitance is usually much lower than the capacitance predicted by the Gouy-Chapmann model. Furthermore, as the concentration of the electrolyte is increased, the predicted behaviour deviates greatly from that of the actual behaviour [28].

A flaw in the model proposed by Gouy and Chapman is that the ions in the solution are treated as point charges that are able to be arbitrarily close to the surface. As a result of this assumption, it is possible for the distance between the ions and the electrode surface to go to zero at high polarizations. Stern noted that ions have finite (non-zero) size and thus are not able to approach the electrode surface arbitrarily closely [53]. The closest distance between any ion and the surface is its ionic radius, with the closest distance of adsorbed ions being the inner Helmholtz plane and the closest distance of solvated ions called the outer Helmholtz plane (Figure 1.5) [28]. These two planes form an inner layer, which is referred to as the Stern layer. For systems at low electrolyte concentrations, this restriction would have little effect since the thickness of the diffuse layer is much larger than that of the Stern layer. However, for systems with high electrolyte concentrations, the charges become more tightly compressed at the Stern layer and the system begins to resemble the Helmholtz model [28].

While each improvement to the Helmholtz model has had some success in reproducing experimental results of electrolytic solutions, the models are rather empirical in nature, with the governing equations being designed from electrochemical phenomena rather than from fundamental principles. A more fundamental approach to modelling these electrolytic

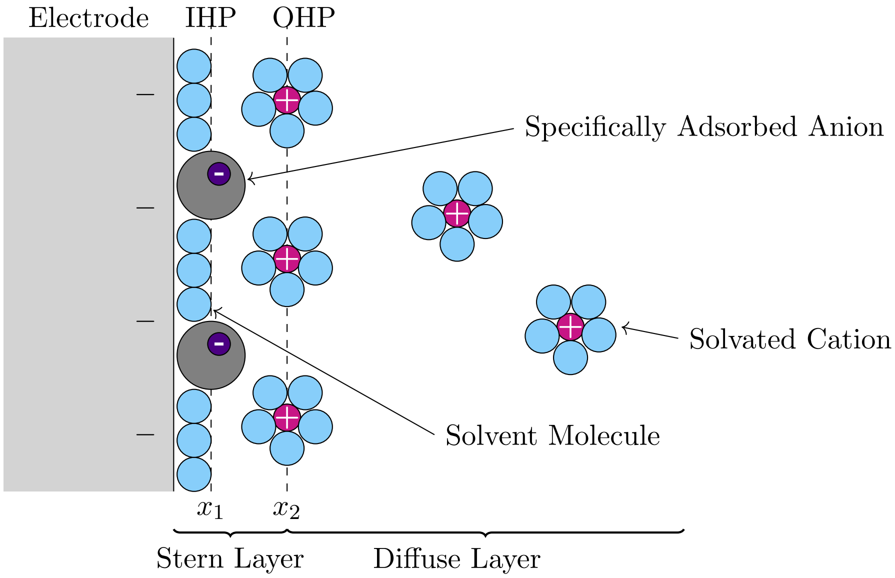

Figure 1.5: Schematic diagram of the electric double layer, where IHP denotes the inner Helmholtz plane at a distance x_1 from the electrode surface and OHP denotes the outer Helmholtz plane at a distance x_2 from the electrode surface. Adapted from [28].

solutions in contact with an electrode will become one of the foci of the work discussed in later chapters.

1.3 Ionic Liquids

While electrolytes have a long and well-documented history in experimental and theoretical electrochemistry, a new class of compounds has recently become of interest for its applications in miniaturized electronics, that is, ionic liquids [54, 55]. Ionic liquids are salts which have a melting point below 100°C, in contrast to molten salts which have a melting point above 100°C [55]. The key difference here is the presence of the solvent. In an electrolytic solution, water or other polar liquids play the role of the solvent which helps to break apart the salt into its respective ions whereas an ionic liquid is devoid of any solvent and the ions exists in a spatial 'matrix' where they are free to move about or form ion pairs [28, 54, 55] (Figure 1.6). Due to the fact that ionic liquids are comprised entirely of positive and negative ions, these solutions often have a high conductivity [56] and are less volatile and more stable than standard electrolytes [54, 56].

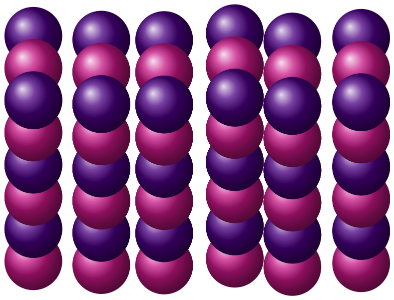

Figure 1.6: Schematic diagram of an idealized ionic liquid lattice matrix, where each ion occupies a 'lattice box'. The purple spheres represent negatively charged ions and the magenta spheres represent positively charged ions. In some cases, the positive and negative ions can form neutral ion pairs [57, 58].

One of the first recorded experiments of a room temperature ionic liquid was by Paul Walden in 1914, who found the melting point of ethylammonium nitrate ($[C_2H_5NH_3][NO_3]$) to be 12°C [59]. In the 1970s and 1980s, significant experiments advancing the understanding of ionic liquids were published, with particular interest in applications to batteries [60, 61]. More recently, ionic liquids have been investigated for their applications in supercapacitors [43, 44, 45] or pseudocapacitors (materials which form a supercapacitor when in combination with an EDL) [62]. Some groups have also experimented with mesoporous electrodes which allow ions to adsorb into the electrode, which allows for improved pseudocapacitance of those electrodes [63]. On the other hand, nanoporous carbon electrodes were found to be ionophobic when immersed in ionic liquids, meaning that the electrode repels ions and can lead to a boost in the energy storage of such supercapacitors [64].

Often, the charged ions will form ion pairs in the liquid lattice, which are neutral aggregates, and therefore do not contribute charge effects to the system [57, 58]. Due to this phenomenon, an on-going debate in the literature concerns whether or not ionic liquids can be modelled as a "dilute electrolyte", because the presence of ion pairs of the ionic liquid may be considered as a background dielectric constant and the unpaired ions to some concentration of charge [57, 58]. While this theory has yet to be confirmed or debunked with computational and experimental results, the idea of modelling ionic liquids in a similar fashion to electrolytes has gained traction.

In 2007, Kornyshev published an analysis of the capacitance of the EDL in ionic liquids by following a similar approach to modelling of an electrolytic EDL by adjusting for the lack of solvent in the ionic liquid. He utilized a mean-field theory that takes into account the short-ranged correlations and finite ion size near the electrified interface of the electrode and the ionic liquid [65]. Kornyshev's analysis has sparked further studies of an ionic liquid in contact with a charged surface in the last decade. All of these approaches apply mean-field theory to analyze the differential capacitance of an ionic liquid in contact with a charged surface [49, 57, 66, 67, 68, 69, 70, 71, 72]. The predictions from these mean-field theory models have also been verified through computational studies of the EDL capacitance of ionic liquids [56, 66, 73].

Many of the recently published studies have only considered an ionic liquid in contact with a metallic electrode. Graphene exhibits a unique band structure which allows for a clear minimum in both the capacitance and conductivity of such electronic devices [28, 17]. Theoretical modelling of an ionic liquid with a graphene electrode is of interest for understanding the capabilities of such electronic devices. Therefore, it is important to develop a full theory and understanding of the mechanisms of an ionic liquid in contact with a graphene electrode.

1.4 Ion Adsorption and Sensing Applications

In the 1970s, Piet Bergveld introduced the idea of an ion sensitive FET (ISFET), which allowed for accurate measurements of ion activities in an electrochemical and biological environments [74]. Bergveld's configuration combined the well known metal-oxide-semiconductor FET with a glass electrode and exposed the oxide to the surrounding environment [74]. This configuration has sparked numerous improvements and modifications over the years, and ultimately, miniaturization of the device to allow for micro- and nano-sensing devices [1, 14, 17, 21, 30, 75]. Regardless of the setting and configuration, all these sensors detect changes via the same mechanism: ions adsorbing onto the electrode, which could be protons (H^+), hydroxide (OH^-), cations (e.g. Na^+, K^+), and/or anions (e.g. Cl^-, F^-) [21, 75, 76] (Figure 1.7). For illustrative purposes, an electrolyte solution of NaCl (table salt) dissolved in water will be considered [77].

Two general approaches for modelling such systems have followed: use of an adsorption isotherm approximation or use of site-binding theory. Adsorption isotherms are normally empirical in nature and describe the variations of the surface charge density with concentration of the solution at constant temperature to obtain a relation between the two quantities [78]. Many well-known isotherms such as the Langmuir and Frumkin isotherms have been developed; however, the favoured isotherm in the literature for ion sensing device configurations is the Langmuir-Freundlich isotherm [75, 78, 79]. Although some success

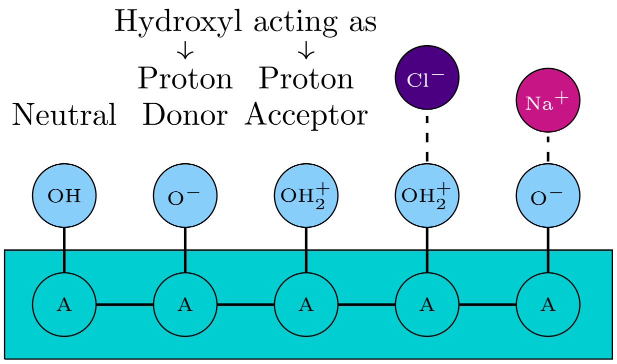

Figure 1.7: Possible structure of the electrode-electrolyte interface with adsorbed ions Na^+ and Cl^- and where A represents the atoms of the electrode. Note that the bonding distance for the Na^+ and Cl^- are different than that of OH, O^-, and OH_2^+ . The formation of complexes AO^- - Na^+ and AOH_2^+ - Cl^- on the surface of the electrode affect the original equilibrium due to a build-up of localized charge near the electrode and the removal of charge from the bulk solution. Adapted from [77].

has been achieved in utilizing isotherms to reproduce experimental results due to their empirical nature, many groups favour site binding theory as the appropriate method for modelling surface interactions as it comes from the fundamental idea of chemical reactions.

Site binding theory is based on surface sites acting as sites where surface chemical reactions can occur [35]. Each binding site is considered to be either neutral, an H^+ donor (acidic reactions) or an H^+ acceptor (basic reactions) [34, 35, 80]. Since 'free' hydrogen plays a key role in the pH of the overall system, the surface charge density of bound protons is determined by the pH of the bulk solution [2, 34, 35, 78]. Since the pH of the system is of interest for sensors, it is common to view OH groups as 'neutral' binding sites [34, 35] and that ions prefer to bind to sites of opposite charge, since this is energetically favoured [79].

An attraction, mediated by both electrostatic and Van der Waals forces, between the ions and substrate must be present for ion specific effects to occur, e.g. surface reactions to occur. This attraction will lead to an equilibrium of the adsorbed ions and the solution ions [81]. Often in sensor devices, a thin oxide layer or polymer layer is added on top of the electrodes (or conducting channel) to help promote the adsorption of ions to the surface [21, 75]. This is called a functionalized layer. For graphene-based devices, this has become a necessary component of engineering design to help improve the overall sensitivity of devices [21, 75, 82]. The oxide or polymer layer is typically only a few nanometers in thickness. Most experimental groups have found layers that are between $2 - 10$ nm thick are the optimal in sensing devices [21, 75, 82].

In the case of a graphene electrode, this oxide layer helps to promote the binding of these ionic species [75], while making the surface hydrophilic. Typical functional layers for graphene devices are aluminium oxide (Al_2O_3) and tantalum pentaoxide (Ta_2O_5), which have been quite successful in boosting the adsorption of ions to the electrode surface and ultimately, increasing the sensitivity of the device [21, 82]. These oxides are chosen for their chemical inertness, insolubility in most solutions (notably water), high dielectric constants which inhibit electron leakage from the conducting channel, ability to be easily manufactured and interfaced with graphene, and most importantly, their ability to bind to graphene to preserve its unique properties [7, 83, 84].

While numerous experimental studies on sensitivity measurements of graphene-based nano-sensors have been reported, very little theoretical modelling to support the experimental results has been done [1, 21, 76, 82]. For further advancement in nano-scale graphene sensors to be achieved, it is necessary to develop a full working model of the relevant mechanisms.

1.5 Outline of Thesis

This thesis is divided as follows: In Chapter 2, a brief overview of the electrical and structural properties of the graphene–electrolyte interface is provided. In Chapter 3, several modifications to the Poisson-Boltzmann equation are analyzed, including modifications due to finite ion size, dielectric saturation, and dielectric decrement in the electrolyte. Numerical solutions for the dependence of ionic concentration profiles on the distance from the electrode surface are also presented. Chapter 4 details the numerical method used in this research and results for the case of an ionic liquid configuration. In Chapter 5, a model for the dependence of graphene-based devices on pH and/or ion concentration is derived. Finally, in Chapter 6, a summary of results is presented, along with some future avenues for modelling of graphene-based FETs.

Unless otherwise stated, Gaussian electrostatic units, where $4\pi\epsilon_0 \equiv 1$ and ϵ_0 is the dielectric permittivity of a vacuum, will be used throughout this thesis.

Chapter 2

Theoretical Background

2.1 Graphene

Carbon is one of the most abundant materials on earth and is one of the building blocks for all organic compounds. When carbon atoms bond to each other, they can form various structures such as diamonds, carbon nanotubes, buckyballs, and graphite. Graphite consists of 2-dimensional sheets of hexagonally bonded carbon atoms, which are arranged in a honeycomb lattice, stacked on top of each other [85]. In 1947, Peter Wallace published work in which a tight binding approximation was applied to the band theory of solids in an effort to investigate the electronic properties of graphite and provided the underlying theory for graphene [86]. In 2004, Andre Geim and Konstantin Novoselov utilized the 'scotch tape' method, whereby adhesive tape is placed on top of graphite and lifted off to remove a single sheet of graphene, and were able to prove that it is possible to isolate incredibly thin 2-dimensional materials [87, 88, 89]. For their work, they were awarded the Nobel Prize in Physics in 2010, and ultimately sparked a fast-growing interest in graphene and its potential in electronics.

Since Geim and Novoselov's development of the 'scotch tape' method in 2004, many new techniques have been developed to reliably isolate pristine, single sheets of graphene. A popular technique is to use chemical vapour deposition (CVD) wherein silicon carbide (SiC) is heated to upwards of 1100°C under low pressure to reduce the compound to graphene [1, 7, 90]. A variant of the CVD method involves depositing graphene onto another metal (e.g. copper foil), which is then dissolved after the graphene sheet has formed. While this method is generally successful at producing pristine sheets of graphene, it can be quite expensive [1, 7, 90]. Another more direct technique to obtain graphene is exfoliation of graphite sheets. This is done by intercalating the graphite sheets with large molecules and separating the sheets via a surfactant, sonification (use of sound waves to break apart the layers), or electrochemical solution [7, 27, 32, 76]. Recently, the use of microwave ovens to produce sheets of graphene, has shown promise for low-cost and precise manufacturing [91]. The technique utilizes microwave radiation to ionize silicon dioxide (SiO_2) and dissociate methane (CH_4) to form graphene and molecular hydrogen. This process is referred to as ‘snowing’ as it yields high-quality graphene flakes which ‘snow’ down on to any substrate [91].

While experimentalists work to perfect a low-cost method of graphene isolation, theoretical groups have been working to unlock the physics behind the numerous properties of graphene. To date, many of these properties have been well documented, such as metal-like conductance, zero-energy band gap, and linear energy dispersion for electrons and holes [26]. These properties make graphene ideal for use in electronic devices since a minimal applied voltage will be required to excite the electrons into the conduction band [85]. Coupling the theoretical modelling of graphene with low-cost manufacturing techniques give graphene a significant edge in the nanoelectronic industry.

2.2 Structure of Graphene

To understand the unique properties that graphene brings to sensor applications, a discussion of its structure is detailed below.

2.2.1 Crystal Structure of Graphene

Many of the unique features of graphene are derived from its hexagonal lattice. Unlike many other materials, graphene has two carbon atoms per primitive cell, which are repeated periodically throughout the lattice (Figure 2.1). These two carbon atoms are labelled A and B, and separated by a distance between of approximately $a \approx 1.42$ Å[8]. The Bravais lattice of graphene is formed via the two vectors

$$\vec{a}_1 = \frac{a}{2}(3, \sqrt{3}), \tag{2.1}$$

$$\vec{a}_2 = \frac{a}{2}(3, -\sqrt{3}), \tag{2.2}$$

and the following translational vectors

$$\vec{t}_1 = \frac{a}{2}(1, \sqrt{3}), \tag{2.3}$$

$$\vec{t}_2 = \frac{a}{2}(1, -\sqrt{3}), \tag{2.4}$$

$$\vec{t}_3 = -a(1, 0). \tag{2.5}$$

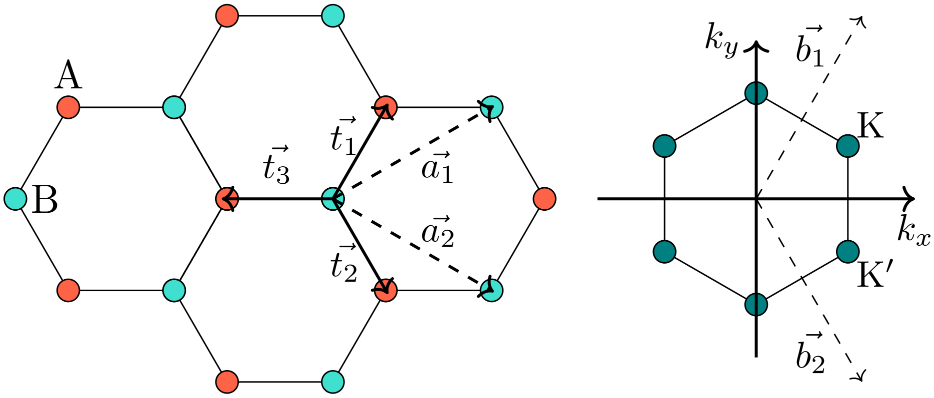

Figure 2.1: Left: Schematic of the crystal structure of graphene. The Bravais lattice can be formed from $\vec{a_1}$ and $\vec{a_2}$ and the nearest carbon atom neighbours from $\vec{t_1}, \vec{t_2}$, and $\vec{t_3}$. Right: Schematic of the first Brillouin zone of graphene. Here, $\vec{b_1}$ and $\vec{b_2}$ are the vectors which form the reciprocal lattice. [8]

In the lattice, each A atom is surrounded by 3 B atoms and vice versa. The translational vectors define the crystal structure of graphene. From here, it can be shown that the reciprocal lattice is given by

$$\vec{b}_1 = \frac{2\pi}{3a}(1, \sqrt{3}), \tag{2.6}$$

$$\vec{b}_2 = \frac{2\pi}{3a}(1, -\sqrt{3}), \tag{2.7}$$

and can be utilized to construct the first Brillouin zone of graphene. Two important points in the reciprocal lattice are:

$$K = \frac{2\pi}{3a}(1, \sqrt{3}) \tag{2.8}$$

$$K' = \frac{2\pi}{3a}(1, -\sqrt{3}). \tag{2.9}$$

2.2.2 Energy Band Structure of Graphene

The band structure is derived via a tight binding approximation, with a detailed derivation provided by Wallace [86]. Each carbon atom consists of six electrons, two of which lie in the $1s$ orbital and are tightly bound to the carbon atom. Since these two electrons have very limited mobility in the graphene lattice, they do not play a role in the electrical properties. The remaining four electrons are distributed in the $n = 2$ electron shell, and can be found in either the $2s$ or $2p$ orbitals. Since the electrons have similar energies, their orbitals become hybridized, whereby the s orbital combines with two p orbitals (i.e. the p_x and p_y orbitals) to form the hybridized sp^2 orbitals in the $x - y$ plane. This hybridization gives rise to strong covalent bonds between the carbon atoms, namely σ bonds, and is responsible for the mechanical strength and viability of graphene. In the first Brillouin zone, 6 σ-bonds form: 3 in the valence band and 3 in the conduction band, and the Fermi energy lies between these two bands in neutral graphene [92] (Figure 2.2).

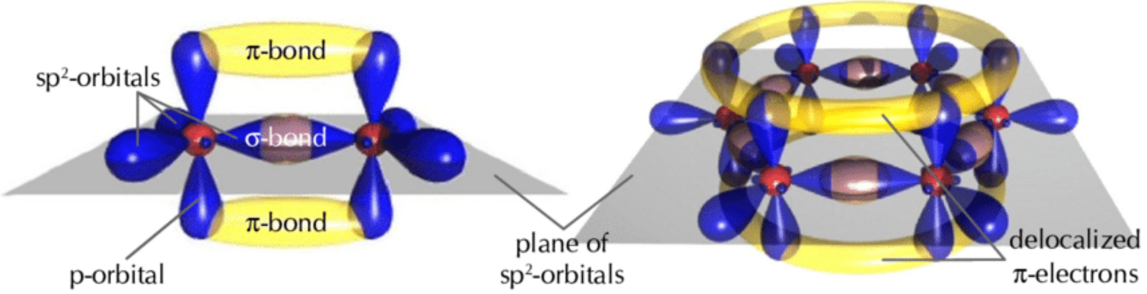

Figure 2.2: Orbital structure of graphene, where a σ-bond occurs between carbon atoms and π-bonds occur in the valence and conduction bands. Adapted from [93].

The third p_z orbital remains well separated, both spatially and energetically, from the hybridized sp^2 orbital, and forms valence and conduction π-bonding bands in graphene. It is these two π-bonds that are responsible for the unique electronic features of graphene. Graphene has 6 valence electrons: the $1s$ orbital containing 2 electrons, the hybridized sp^2 orbitals containing 3 electrons, and the p_z orbital containing 1 electron.

The points K and K' denote the points in the lattice where the conduction band and the valence band meet leaving a zero-energy band gap. These points are known as Dirac points since the energy dispersion for the π electrons in this region can be described by two conic surfaces, enabling low-energy excitations of π electrons akin to the massless Dirac fermions in 2-dimensions [8] (Figure 2.3). While a full derivation of the band structure is not provided here, full details can be found in [94, 92].

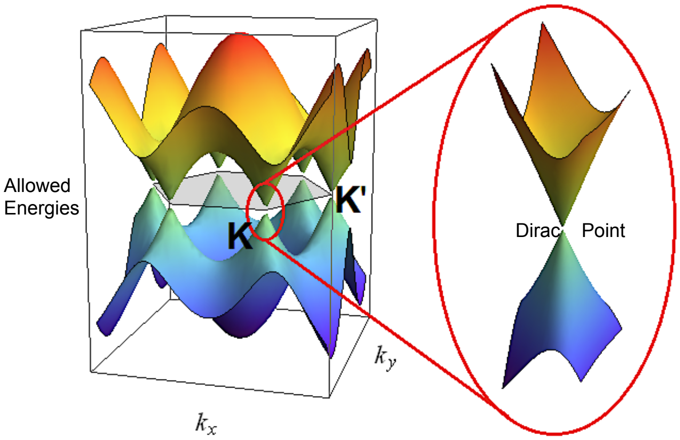

Figure 2.3: Band structure of π electrons of graphene showing points where the conduction band and the valence band meet at the Dirac points. Adapted from [8].

2.2.3 Charge Carriers in Graphene

One of the useful quantities for any semiconductor is the density of states as it gives a direct link to the number density of charge carriers in a system (i.e. the number of electrons or holes in the valence/conduction band) [85]. The density of states is a measure of the number of accessible energy states for electrons at any given energy level. For graphene, the density of states is given by [8, 95]:

$$D(\varepsilon) = \iint_{\mathrm{BZ}} \frac{g}{(2\pi)^2}\delta(\varepsilon - \varepsilon(\vec{k}))d^2\vec{k}, \tag{2.10}$$

where BZ denotes the Brillouin zone, g is a degeneracy factor and $\varepsilon(\vec{k})$ is the band energy of the π electrons in graphene. In the case of graphene, $g = 4$ since there are two spin states (spin up and spin down) for the electrons and since there are two complete Dirac cones in a hexagon of the graphene lattice. Using the Dirac cone approximation, the band energy of the π electrons is $\varepsilon(\vec{k}) = \pm\hbar v_F k$, where $v_F = \frac{c}{300}$ (where c is the speed of light) is the Fermi speed and $\hbar$ is the reduced Planck's constant. Interestingly, the band energy for graphene is independent of the electron mass [8]. Then, the density of states for graphene is given as [8, 95]:

$$D(\varepsilon) \approx \frac{g}{(2\pi)^2}\int_0^{2\pi} d\phi \int_0^{\infty} k\delta(\epsilon \pm \hbar v_F k)dk \tag{2.11}$$

$$= \frac{2|\varepsilon|}{\pi(\hbar v_F)^2}, \tag{2.12}$$

which is a linear function of energy ε and symmetric about the Dirac point energy, $\varepsilon = 0$. Note that the reference level, ε_D, for the above density of state is the Dirac point energy. For convenience, define ε_D with respect to the local vacuum level, and thus the electron energy can be expressed as $E = \varepsilon - \varepsilon_D$. If the Fermi level, ε_F, is also defined with respect to the vacuum level, then the density of states can be used to calculate the equilibrium number density of charge carriers in doped graphene as follows [25, 39]:

$$n(\mu) = \int_{-\infty}^{\infty} D(\varepsilon)\left[\frac{1}{1+e^{\beta(\varepsilon-\mu)}} - \frac{1}{1+e^{\beta\varepsilon}}\right]d\varepsilon, \tag{2.13}$$

where $\beta = \frac{1}{k_B T}$ and $\mu = \varepsilon_F - \varepsilon_D$ is the chemical potential of graphene with respect to its intrinsic (neutral) state [25, 39]. When $\mu > 0$, graphene becomes doped with excess electrons and thus the number of charge carriers is $n > 0$ (graphene is negatively charged), whereas when $\mu < 0$, graphene becomes doped with excess holes and the number of charge carriers is $n < 0$ (graphene is positively charged).

For low doping levels, that is when $|\mu| \lesssim 1$ eV, the linear approximation for the density of states, Equation (2.12), may be used. Using the approximation in Equation (2.13) gives the number density as

$$n(\mu) = \frac{2}{\pi(\hbar v_F \beta)^2}\Big(\mathrm{dilog}(1+e^{-\beta\mu}) - \mathrm{dilog}(1+e^{\beta\mu})\Big), \tag{2.14}$$

where dilog is the standard dilogarithm function [25, 39], given by $\mathrm{dilog}(x) \equiv \int_x^0 \frac{\ln(1-x')}{x'}dx'$. Then the surface charge density of graphene is given by [25, 39]:

$$\sigma_g = \frac{2e}{\pi(\hbar v_F \beta)^2}\Big(\mathrm{dilog}(1+e^{-\beta\mu}) - \mathrm{dilog}(1+e^{\beta\mu})\Big). \tag{2.15}$$

This density of states is directly linked to the charge carrier density in graphene-based electronic and electrochemical systems.

2.3 Poisson-Boltzmann Equation

When a salt is dissolved in the solvent to create the electrolyte, the dissolved ions become surrounded by a layer of solvent molecules (Figure 1.6). These solvated ions exist in the diffuse layer of the system, where they are free to move. Due to the charged electrode immersed in the electrolyte, solvated salt ions of opposite charge will be attracted to the surface and ions of similar charge will be repelled. As discussed earlier, this attraction of oppositely charged ions to the surface creates an electric double layer (EDL) that contains a distribution of charges that is determined through the equilibrium positions of the mobile charged ions. To take into account the bulky size of the hydrated ions and any specifically adsorbed species, a modification to the structure of the diffuse layer is proposed where a Stern layer is introduced adjacent to the electrode [53]. The Stern layer is considered to be charge-free and its thickness is set to be the radius of the solvated ions. The simplest models of the diffuse layer give rise to unreasonable ion concentrations at the interface of the charged electrode and the addition of a Stern layer helps to lower the concentrations by accounting for the effect of ion crowding at the electrode [53]. While many models have been proposed with varying degrees of success, a more fundamental approach to modelling the diffuse layer is presented here.

To be able to accurately describe and account for all the mechanisms in complex electrochemical systems, models with a foundation derived from fundamental principles is necessary. For a self-consistent model of electrochemical sensors, an approach from thermodynamics is proposed, beginning with the Helmholtz free energy of the system: $F = U - TS$ [51, 52, 96]. In the simplest setting, by treating mobile ions in the electrolyte as point charges, the internal energy of the system is:

$$U = \iiint \left[-\frac{\epsilon_w}{8\pi}(\nabla\phi)^2 + (z_+ec_+ - z_-ec_-)\phi \right] d^3\vec{r}, \tag{2.16}$$

where ϵ_w is the dielectric permittivity of the solvent (in this case water), ϕ is the electrostatic potential, z_ie the charge on the i^{th} ionic species, and c_+ and c_- are the concentrations of positive and negative ions, respectively. Using an entropy of an ideal gas of point-like ions [97], the entropic contribution is:

$$-TS = \frac{1}{\beta}\iiint \left[c_+ \ln\left(\frac{c_+}{c_\infty}\right) + c_- \ln\left(\frac{c_-}{c_\infty}\right) - c_+ - c_- \right] d^3\vec{r}, \tag{2.17}$$

where c_∞ is the bulk concentration of each ionic species and $\beta = \frac{1}{k_BT}$ with k_B being the Boltzmann constant and T the temperature. Note that the integrand of the free energy is a Lagrangian, which is obtained as the negative of the functional U (Appendix D).

Minimizing the free energy with respect to concentrations c_+ and c_- gives:

$$\begin{aligned}\frac{\delta F}{\delta c_\pm} &= \iiint \left[\pm z_\pm e\phi + k_B T \ln\left(\frac{c_\pm}{c_\infty}\right)\right] v\, d^3\vec{r} = 0 \\ \implies c_\pm &= c_\infty e^{\mp z_\pm e\beta\phi}, \end{aligned} \tag{2.18}$$

which is the well-known Boltzmann distribution of ions. Here, v is a function that belongs to the set of all admissible variations of the free energy; see Appendix A for the full details of finding the stationary points of the free energy. Similarly, minimizing the free energy with respect to potential ϕ gives Poisson's equation:

$$\begin{aligned}\frac{\delta F}{\delta \phi} &= \iiint \left[e(z_+c_+ - z_-c_-) + \frac{2\epsilon}{8\pi}\nabla^2\phi\right] v\, d^3\vec{r} = 0 \\ \implies \epsilon\nabla^2\phi &= -4\pi\rho, \end{aligned} \tag{2.19}$$

where $\rho = z_+c_+ - z_-c_-$. Since the concentrations are given by the Boltzmann distribution (Equation 2.18), Equation 2.19 is known as the Poisson-Boltzmann equation in the diffuse layer of the EDL.

For a symmetric electrolyte solution ($z_+ = z_- = z$), with $c_+ = c_- = c_\infty$ in the bulk, the system described by the Poisson-Boltzmann equation is [48],

$$\epsilon\nabla^2\phi = -4\pi ze(c_+ - c_-) = 8\pi zec_\infty \sinh(ze\beta\phi). \tag{2.20}$$

This Poisson-Boltzmann equation has an analytic solution for the potential ϕ as a function of x for 1D Cartesian geometry, given by

$$e^{\frac{ze\beta\phi}{2}} = \frac{e^{\frac{ze\beta\phi_0}{2}} + 1 + \left(e^{\frac{ze\beta\phi_0}{2}} - 1\right)e^{-\lambda_D^{-1}x}}{e^{\frac{ze\beta\phi_0}{2}} + 1 - \left(e^{\frac{ze\beta\phi_0}{2}} - 1\right)e^{-\lambda_D^{-1}x}}, \tag{2.21}$$

where ϕ_0 is the potential at the surface ($x = 0$) and $\lambda_D^{-1} = \sqrt{\frac{8\pi\beta z^2e^2c_\infty}{\epsilon_w}}$ is the Debye length (derived below). Using the solution for the Poisson-Boltzmann equation, the surface charge in the diffuse layer is then given as

$$4\pi\sigma_{PB} = \epsilon_w \left.\frac{d\phi}{dx}\right|_{x=0} \tag{2.22}$$

$$= -\frac{2\epsilon_w}{ze\beta\lambda_D}\sinh\left(\frac{ze\beta\phi_0}{2}\right), \tag{2.23}$$

where ϵ_w is the dielectric permittivity of water. Equation (2.23) is known the Grahame equation [98]. The differential capacitance of the diffuse layer using the Poisson-Boltzmann model is then

$$C_{PB} = -\frac{d\sigma_{PB}}{d\phi_0} \tag{2.24}$$

$$= \frac{\epsilon_w}{4\pi\lambda_D} \cosh\left(\frac{ze\beta\phi_0}{2}\right). \tag{2.25}$$

Debye-Hückel Limit

By assuming that the variation in the potential is small and/or the temperature is high, $|ze\beta\phi| \ll 1$, the ion concentration can be linearized to $c_i(\phi) \approx c_\infty(1 - ze\beta\phi)$. This yields the Debye-Hückel approximation or linearized Poisson-Boltzmann equation. Further assuming that the dielectric permittivity of the solvent is independent of position gives the Helmholtz equation [28, 48]

$$\nabla^2\phi = \lambda_D^{-2}\phi, \tag{2.26}$$

where λ_D is the Debye screening length defined as

$$\lambda_D^{-1} = \sqrt{\frac{8\pi\beta z^2 e^2 c_\infty}{\epsilon_w}}. \tag{2.27}$$

The Debye screening length gives the measure of the depth of penetration of the electrostatic effect. For every Debye screening length, the electric potential drops off by a factor of $1/e$ [28, 48]. Solving Equation (2.26) for $\phi(x)$ with the boundary condition that $\phi(x \to \infty) = 0$ gives:

$$\phi(x) = \phi_0 e^{-\frac{x}{\lambda_D}}, \tag{2.28}$$

where $\phi_0 = \phi(0)$ is the potential at $x = 0$. Here, the other mathematically possible solution $e^{\frac{x}{\lambda_D}}$ is discarded as it is unphysical for the potential to increase exponentially in the bulk with increasing distance away from the electrode. From Gauss' Law, the surface charge of the diffuse layer in the Debye-Hückel limit, σ_d^{DH}, can be related to the potential at the electrode-electrolyte interface by:

$$4\pi\sigma_d^{DH} = \epsilon_w \left.\frac{d\phi}{dx}\right|_{x=0} \tag{2.29}$$

$$= \epsilon_w \left(-\frac{\phi_0}{\lambda_D}\right), \tag{2.30}$$

upon substitution of Equation (2.28). Then, using the definition of differential capacitance, the Debye-Hückel diffuse layer capacitance in given by:

$$C_d^{DH} = -\frac{d\sigma_d^{DH}}{d\phi_0} \tag{2.31}$$

$$= \frac{\epsilon_w}{4\pi\lambda_D}, \tag{2.32}$$

upon substitution of Equation (2.30).

The Poisson-Boltzmann equation was one of the first ‘successful’ attempts at modelling electrochemical systems. While this model is too primitive to be able to fully describe all the nuances of a graphene-based system, it is the basis from which more accurate models are derived, particularly in the case of graphene-based sensors.

2.4 Graphene-Based Field-Effect Transistors

A more recent configuration of a graphene FET includes a top gate in the bulk of the liquid electrolyte, which is of interest to biomedical applications (Figure 1.1) [22]. When the gate voltage is applied through the electrolyte, a redistribution of the ions occurs and an EDL forms at the graphene-electrolyte interface [28]. This EDL can vary in thickness depending on the ion concentration, and has a the capacitance that is higher than the capacitance due to the back gate [99]. As a consequence, the surface potential on the graphene layer can be controlled more effectively, while requiring a lower operating voltage than currently used with back-gated graphene FETs [99]. By applying a voltage, the conductance of graphene changes due to the variation in the chemical potential, which can be used to sense the ion concentration and pH of the solution [27, 32, 85].

A cross-sectional view of the EDL at the interface with an infinite planar graphene electrode immersed in electrolyte is shown in Figure 2.4. Several useful equations are identified using Gaussian pillboxes for the electric field:

$$-\epsilon_w E_s = 4\pi\sigma_d \tag{2.33}$$

$$\epsilon_s E_g = 4\pi\sigma_g, \tag{2.34}$$

and the continuity condition for dielectric displacement $\epsilon_s E_g = \epsilon_w E_s$. Adding (2.33) and (2.34) results in the charge neutrality condition for the system:

$$\sigma_g(V_g) + \sigma_d(V_d) = 0, \tag{2.35}$$

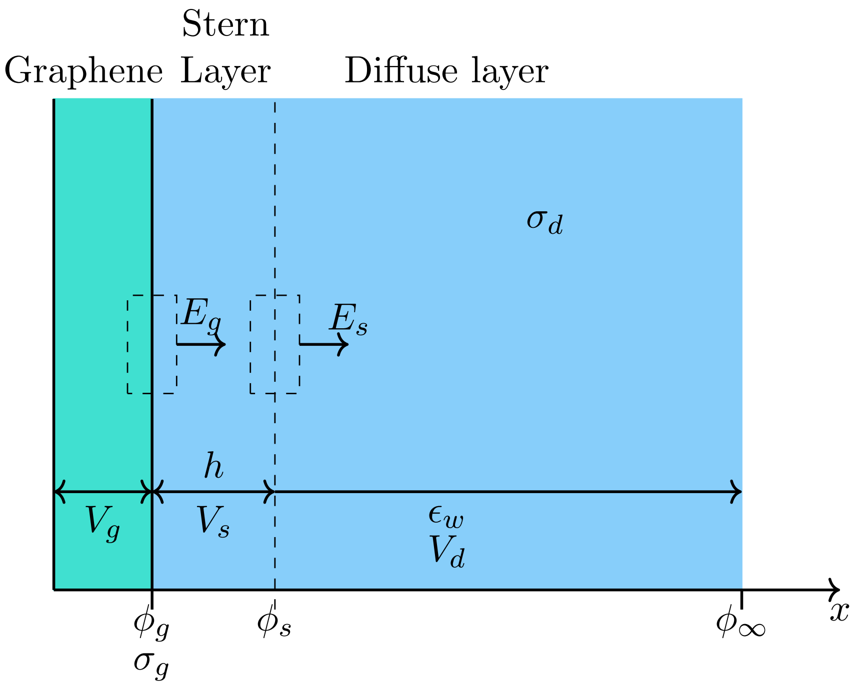

Figure 2.4: Schematic representation of the layered system with labelled surface charges, potentials, electric fields, and dielectric constants. Also shown are the potential differences that occur across the Stern layer, $V_s = \phi_s - \phi_g$, and across the diffuse layer, $V_d = \phi_\infty - \phi_s = -\phi_s$ due to $\phi_\infty = 0$, as well as the total applied potential, $V_a = V_g + V_s + V_d$.

where V_g is the potential drop across graphene and V_d is the potential drop across the diffuse layer.

Furthermore, using Equation (2.33) and the continuity condition gives:

$$C_s V_s = \sigma_d, \tag{2.36}$$

where $C_s = \epsilon_s/(4\pi h)$ is the Stern layer capacitance, with h being the Stern layer thickness, and the surface charge in the diffuse layer σ_d is given by Equation (2.23) in the case of point charges. The following chapters will mostly consider modifications of the Poisson-Boltzmann equation, taking into account effects of finite ion sizes, or steric effects in the Boltzmann distribution, as well as generalizations that go beyond the assumption of constant dielectric permittivity in the electrolyte.

When the Stern layer is discarded, $h \to 0$ so that the diffuse layer becomes adjacent to the electrode. When the graphene electrode is replaced with a metallic electrode, $V_g = 0$ so that $\sigma_g = 0$ (comes from Equation (2.15)).

2.4.1 Total Capacitance

To understand the electrochemical charging of a graphene FET through the EDL, the electrostatic capacitance becomes an important quantity. Experimentally, the capacitance is determined as the differential capacitance per unit area (normally in microFarads per square centimetre, $\mu F/cm^2$), and theoretically, is the rate of change in the surface charge density through the respective region. The capacitance in a graphene FET has two origins: the classical electrostatic capacitance where the double layer is treated as a planar capacitor and the quantum capacitance in graphene. The double layer capacitance arises from the Coulomb repulsion of electrons, which gives a non-zero potential drop across the diffuse layer and is associated with the charging of the graphene electrode. The quantum capacitance arises from forcing electrons to occupy all energy levels up to the Fermi level by the Pauli exclusion principle.

The inverse of the total differential capacitance of the electrolytically gated graphene is given by

$$C_{dsq}^{-1} \equiv -\frac{dV_a}{d\sigma_g} = -\frac{dV_d}{d\sigma_g} - \frac{dV_s}{d\sigma_g} - \frac{dV_g}{d\sigma_g} \tag{2.37}$$

$$= \frac{1}{C_d(V_d)} + \frac{1}{C_s} + \frac{1}{C_q(V_g)}, \tag{2.38}$$

where the charge neutrality condition, Equation (2.35), has been used to obtain the quantum capacitance term and $V_a = V_g + V_s + V_d$ is the total applied potential, with V_d the potential drop across the diffuse layer, V_s the potential drop across the Stern layer, and V_g the potential drop across graphene, see Figure 2.4. Here, $C_d = -\frac{d\sigma_d}{dV_d}$ is the diffuse layer capacitance, $C_s = \frac{d\sigma_d}{dV_s}$ is the Stern layer capacitance, and $C_q = -\frac{d\sigma_g}{dV_g}$ is the quantum capacitance of graphene. This total capacitance corresponds to a series connection of the diffuse layer capacitance, Stern layer capacitance and graphene quantum capacitance. It should be stressed that the values of the diffuse layer potential V_d and the graphene potential V_g, which are used in the calculations of the capacitances of graphene, C_q, and the diffuse layer, C_d, are determined self-consistently by solving the charge neutrality condition, Equation (2.35), of the structure. The expression for $\sigma_g(V_g)$ is given in Equation (2.15), whereas $\sigma_d(V_d)$ can be related to the values of the dielectric permittivity of the diffuse layer and the Stern layer by Gauss' law, $\epsilon_h E_h = -4\pi\sigma_d$ in a manner that depends on the model used for modifying the Poisson-Boltzmann equation. In the case of point charges in the diffuse layer, $\sigma_d(V_d)$ is given by Equation (2.23).

To discard the Stern layer, let $h \to 0$ so that $C_s \to \infty$ in Equation (2.38), giving the total capacitance as a series connection of the diffuse layer capacitance and the graphene quantum capacitance. Similarly, replacing graphene by a metallic electrode with its surface at $x = 0$ would have $V_g = 0$ giving $C_q \to \infty$ in Equation (2.38), so that the total capacitance of the electric double layer is a series connection of the diffuse layer capacitance and the Stern layer capacitance. This is corroborated by the fact that ideal metallic electrodes have a high density of charge carriers at their Fermi energy, so adding or removing charge on the metal electrode does not shift that energy. Hence, the capacitance of an ideal metallic electrode is mathematically infinite and plays no role in any parallel connection of capacitors involving other systems.

2.4.2 Quantum Capacitance and Conductivity

Capacitance in the graphene layer arises from the Pauli exclusion principle which forces electrons to occupy all the energy levels up to the Fermi level and causes an increase in graphene internal electrical potential $V_g = \frac{\mu}{e}$. This is known as the quantum capacitance, which can be calculated as the rate of change in the surface charge density on graphene, σ_g (Equation (2.15)), [25, 39],

$$\begin{aligned} C_q &= -\frac{d\sigma_g}{dV_g} && (2.39) \\ &= e^2 \frac{dn(\mu)}{d\mu} && (2.40) \\ &= e^2 \frac{4}{\pi} \frac{1}{\beta(\hbar v_F)^2} \ln\left(2\cosh\left(\frac{\beta e V_g}{2}\right)\right), && (2.41) \end{aligned}$$

upon substitution of Equation (2.14) into Equation (2.40). Note that this expression for quantum capacitance is valid for $|\mu| \lesssim 1$ eV.

Similarly, the electrical conductivity for graphene may be derived using Boltzmann transport theory [8, 95]. The capacitance and conductivity are the main observables in experimental work, and are also used to show the sensitivity of the electrolytically gated graphene FET (Figure 1.1) to ion concentration and pH. For sensor applications, this quantum capacitance is generally much smaller than the capacitance of the other layers and dominates in the system [28, 30], making graphene an ideal electrode for these electronic configurations.

Chapter 3

Modifications of the Poisson-Boltzmann Equation in Electrolyte

3.1 Theory

The standard Poisson-Boltzmann equation assumes that the ions are point-like charges and that the dielectric permittivity of solvent is constant, as on Page 19 in Section 2.3. This assumption allows unrealistically large ion concentrations at the electrode–electrolyte interface. Bare ions are typically on the order of $0.6-2$ Å and hydrated ions on the order of $2-4$ Åin radius, which are much larger than the point-charge assumption [78]. At high ion concentrations and/or high electric fields in particular, the finite (non-zero) size of the ions must be taken into account as only a finite number of ions, either bare or hydrated, can pack at the electrode–electrolyte interface. In addition, at such high concentrations and fields, the electrolyte also contributes because the dielectric permittivity can become influenced by the alignment of the water dipoles with the electric field and/or with the charged solvated ions in the solution. In this chapter, modifications to take into account the finite ion size and the effects on the dielectric permittivity are considered. The results shown in this chapter have been published in *Journal of Chemical Physics* [40] and *Chemical Physical Letters* [41].

3.2 Steric Effects

While it is recognized that Stern [53] was the first to introduce the idea of the finite size of ions into the model of the double layer, the first complete model including the finite size of ions in the context of the Poisson-Boltzmann equation was proposed by Bikerman in 1942 [96]. Bikerman applied a continuum volume constraint to the existing Poisson-Boltzmann theory, in order to arrive at a model which included ion size. Bikerman's model is based on the entropic contribution to the free energy of the system, where the lattice gas is occupied by three types of quantities: positive ions, negative ions, and water molecules [96]. This modification from Bikerman and Freise [48, 96, 97, 100, 101] is necessary in dense electrolytes and/or when a large voltage (potential drop) is applied which results in a highly charged electrode that is able to attract more oppositely charged ions to the interface, giving rise to ion crowding at the electrode [48]. The Bikerman-Freise model contains a Fermi-like modification to the Boltzmann distribution of the ions in the electrolyte and introduces an effective ion size parameter to the standard Poisson-Boltzmann theory [40, 48, 96, 100]. This inclusion of finite ion size in the electrolyte is called steric effects.

To calculate the entropic contribution, the lattice (see Appendix B) consists of cells with size a. Note that the entropy S is $k_B \sum_i p_i \ln p_i$, where p_i is the probability that species i occupies the lattice site where $p_i = a^3 c_i$ and subject to the constraint that $a^3 c_- + a^3 c_+ + a^3 c_w = 1$, where c_w is the concentration of water molecules. For simplicity, it is assumed that the size of the positive and negative ions, as well as the water molecules, are the same and equal to a. Then the entropic term, $-TS$, is [97]

$$\begin{aligned} -TS = \frac{k_B T}{a^3} \iiint \Big[& a^3 c_- \ln(a^3 c_-) + a^3 c_+ \ln(a^3 c_+) \\ & + (1 - a^3 c_- - a^3 c_+) \ln(1 - a^3 c_- - a^3 c_+) \Big] d^3\vec{r}. \end{aligned} \tag{3.1}$$

The 3 terms on the right hand side of Equation (3.1) correspond to the contributions of the negative ions, positive ions, and solvent molecules, respectively [97]. Note that the free energy of the standard Poisson-Boltzmann model can be recovered by taking the limit $a \to 0$, and that the free energy now is a function of potential ϕ and concentrations $c_\pm$.

Finite ion size is only one modification in the electrolyte. The electric field induces additional structure on the orientation of molecules, resulting in a deviation of the apparent dielectric permittivity from its bulk value ($\epsilon_w \approx 80$). In subsequent sections, two contributions to the shift in apparent dielectric permittivity, dielectric saturation and dielectric decrement, will be investigated, while being coupled with the finite size of ions.

3.3 Modifications for Dielectric Permittivity

The Bikerman-Freise modification to the Poisson-Boltzmann equation has had some success in reproducing experimental results, in particular, that the potential remains finite (particularly when close to the electrode interface). However, further improvements and additional effects can be considered. In particular, the inclusion of a finite ion size in the electrolyte made modifications to the entropic term of the free energy, while the internal energy portion of the free energy is unaltered.

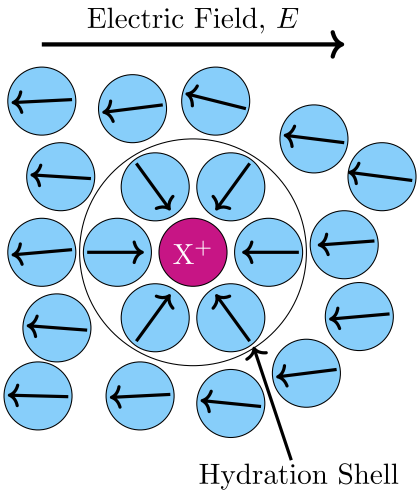

Figure 3.1: Schematic diagram showing water molecules near a cation X^+ in the presence of an electric field E. Water molecules (blue circles) close to the ion form a hydration shell and have their dipoles (represented by the arrows inside the water molecules) oriented along the local electric field generated by that positive ion. The farther away water molecules are from this hydration shell, the less they are affected by the cation, and their dipoles align with the direction of the external electric field. Adapted from [102].

In the unmodified Poisson-Boltzmann model, the solvent is represented as a pure material with a constant dielectric permittivity. Under the application of an electric field, the electric field and the structure of the dissolved ions forces solvent dipoles into specific orientations, resulting in the solvent having less freedom (Figure 3.1). The solvent is not able to act as an unconstrained, uniform material, and modifications to the dielectric permittivity are introduced to take into account the deviations from the dielectric permittivity of pure solvent. These modifications are introduced through the internal energy of the system where the dielectric permittivity implicitly dependents on position through its explicit dependence on the electric field and ion concentrations.

The electrostatic energy, U, can then be expressed as [97]

$$U = \iiint \Big[-w_e(\|\nabla\phi\|, c_+, c_-) + ze(c_+ - c_-)\phi - \mu_+ c_+ - \mu_- c_- \Big] d^3\vec{r}. \tag{3.2}$$

The first term, $w_e(\|\nabla\phi\|, c_+, c_-)$, is the self-energy of the electric field (i.e. the electrostatic potential energy), which, in general, is a function of the electric field ($||\nabla\phi||$) and, possibly, of the ion concentration (c_+ and c_-). The next term, $ze(c_+ - c_-)\phi$, is the electrostatic energies of the positive and negative ions. The last two terms, $\mu_\pm c_\pm$, are the constraints for the conservation of the number of ions, where $\mu_\pm$ is the chemical potential of the bulk electrolyte and act as Lagrange multipliers to ensure that the ions in the electrolyte are coupled to the bulk ionic solution [97]. Note that the integrand of the free energy plays the role of a Lagrangian, which is obtained as the negative of the functional U (Appendix D). In the following sections, two modifications to the dielectric permittivity in the electrolyte will be analyzed, where exact forms of w_e will be given. Since no reliable models are available to describe the joint dependence of dielectric permittivity of the solvent, $w_e(\|\nabla\phi\|, c_-, c_+)$, on the local electric field, $\|\nabla\phi\|$, and on the local ion concentrations, c_+ and c_-, the cases of dielectric saturation, where w_e only depends on the electric field, and dielectric decrement, where w_e only depends on the ion concentrations shall be considered separately.

3.3.1 Dielectric Saturation

At the electrolyte–electrode interface, the potential drops over a short distance due to ion screening, and hence, a strong electric field develops [48]. In the diffuse layer, this corresponds to a reduction in the local dielectric permittivity due to the strong electric fields and high ion concentrations [25, 39, 48, 98, 103]. This strong electric field causes the dipoles of the solvent (water) molecules to align in the direction of that field, which results in a field dependent self-energy, i.e. $w_e(\|\nabla\phi\|)$ in Equation (3.2) (see Figure 3.1).

Sandberg and Edholm [104] pointed out that the energy density of the electric field, $w_e = \frac{\epsilon}{8\pi}\|\nabla\phi\|^2$, which holds for a system with a field-independent dielectric permittivity, should be replaced in the regime of non-constant dielectric response by an integral expression:

$$w_e(\|\nabla\phi\|) = \frac{1}{4\pi}\int_0^{\|\nabla\phi\|} \epsilon(E)\, E\, dE, \tag{3.3}$$

where $\epsilon(E)$ is the dielectric permittivity expressed as a function of the local electric field E. Combining Equations (3.1), (3.2), and (3.3) yields a fully modified free energy functional. The thermodynamic equilibrium state can then be found by minimizing the above free energy functional. Using the variation of the free energy with respect to $c_\pm$, a generalized Boltzmann distribution of ions in the presence of a non-constant electrical potential ϕ may be found from [101, 102, 105, 106]

$$\frac{\delta F}{\delta c_\pm} = \iiint \left[\pm ze\phi - \mu_\pm + k_B T \ln(a^3 c_\pm) - k_B T \ln(1 - a^3 c_- - a^3 c_+)\right] v d^3\vec{r} = 0, \tag{3.4}$$

where v is a function that belongs to the set of all admissible variations of the Helmholtz free energy, which follows a similar method to that outlined in Appendix A. The size-modified chemical potentials at equilibrium in the bulk electrolyte are then

$$\mu_\pm = \frac{1}{\beta} \ln\left(\frac{a^3 c_\infty}{1 - 2a^3 c_\infty}\right), \tag{3.5}$$

which comes from solving Equation (3.4) for $\mu_\pm$ in the bulk electrolyte (i.e. $c_\pm \to c_\infty$ and $\phi(x \to \infty) = 0$) and defining the bulk concentration as c_∞. Then, the ion concentrations are given by:

$$c_\pm = \frac{c_\infty e^{\mp ze\beta\phi}}{1 - \nu + \nu\cosh(ze\beta\phi)}. \tag{3.6}$$

Defining the bulk volume fraction of ions as $\nu = 2a^3 c_\infty$, gives the expression for the equilibrium charge density in the electrolyte, $\rho = ze(c_+ - c_-)$ as [48, 96, 100]:

$$\rho = \frac{-2zec_\infty \sinh(\beta ze\phi)}{1 + 2\nu\sinh^2(\frac{ze\beta\phi}{2})}. \tag{3.7}$$

Note that the standard Poisson equation (Equation 2.19 on Page 20) is obtained in the limit $\nu \to 0$, whereas for densely packed ionic structures one expects $\nu \lesssim 1$ [56]. For sufficiently large potentials when ν is finite, i.e. $\exp(ze\beta|\phi|) \gg 2/\nu$, the charge density in Equation (3.7) approaches a constant value, $\rho \to -zec_{\max}\text{sign}(\phi)$, where $c_{\max} = 1/a^3$ is the maximum concentration of ions of either kind (i.e. cations or anions).

Minimizing the free energy with respect to the potential ϕ yields

$$\frac{\delta F}{\delta \phi} = \iiint \left[\nabla \cdot \left[w'_e(||\nabla\phi||)\frac{\nabla\phi}{||\nabla\phi||}\right] + ze(c_+ - c_-)\right] v d^3\vec{r} = 0, \tag{3.8}$$

where $w'_e(\|\nabla\phi\|)$ is the derivative of the self-energy with respect to $\|\nabla\phi\|$ and v is a function belonging to the set of all admissible variations of the Helmholtz free energy (Appendix

A). Setting the charge density $\rho = ze(c_+ - c_-)$ and substituting Equation (3.3) for the self energy, w_e, gives an expression which is similar to that of the original expression for the Poisson-Boltzmann equation:

$$\nabla \cdot [\epsilon_{sat}(||\nabla\phi||)\nabla\phi] = -4\pi\rho, \tag{3.9}$$

where $\epsilon_{sat}(||\nabla\phi||)$ is the electric field dependent dielectric permittivity. If the effects of the electric field are ignored, the dielectric permittivity will revert back to a constant, i.e. $\epsilon_{sat}(||\nabla\phi||) \to \epsilon_w$. In this case, the original expression for the Poisson-Boltzmann equation (Equation (2.19) on Page 20) is recovered.

Other groups have proposed an alternative derivation based upon a free energy minimization [107, 108]. Instead of utilizing the expression for the self-energy as given in Equation (3.3), those authors used $w_e(\|\nabla\phi\|) = \epsilon(\|\nabla\phi\|)\|\nabla\phi\|^2/(8\pi)$, which is only valid when the dielectric permittivity of solvent ϵ does not depend on the electric field, i.e., in the regime of linear dielectric response. The Poisson-Boltzmann equation obtained from this approach is essentially equivalent to Equation (3.9), where the dielectric permittivity $\epsilon(\|\nabla\phi\|)$ is replaced by $\epsilon(\|\nabla\phi\|) + \frac{1}{2}\|\nabla\phi\|\,\epsilon'(\|\nabla\phi\|)$. Here, $\epsilon'(\|\nabla\phi\|)$ denotes the first derivative of the function $\epsilon(\|\nabla\phi\|)$. It is worthwhile to note that while this approach yields a similar result to that discussed above, this approach is inconsistent for the regime of non-linear dielectric response, i.e. when $\epsilon(\|\nabla\phi\|)$ is a function of the magnitude of the electric field [104], and hence, many other groups [25, 109, 110, 111, 112] have utilized the approach taken above.

Booth Model

The effect of dielectric saturation of solvents in the presence of high electric fields near a charged surface may be described by a model due to Booth. In this model, the dielectric permittivity of solvent is given as a non-linear function of the magnitude of the local electric field [113]. Booth's model has shown very good agreement with the molecular dynamics simulations of the dielectric constant of water at high electric fields [114, 115], as well as with a lattice Monte-Carlo simulation of dielectric saturation in ion-containing liquids [116].

While the Booth model is derived by considering the microscopic orientational degrees of freedom of the solvent dipole molecules [105, 113], a phenomenological model for dielectric saturation in diffuse layers was developed by Grahame [98], which is sometimes used in conjunction with a Stern layer [117, 118] or with the Bikerman-Freise model [48]. Macdonald, for example, used a combined Grahame-Stern model to fit a series of experimental data for the differential capacitance of metallic electrodes in aqueous solutions as a function of the applied potential, which typically exhibit strong asymmetry with respect to the neutrality point [117, 118].

The Booth model for dielectric saturation results in a diffuse layer dielectric permittivity given by [113]:

$$\epsilon_{Booth}(E) = n^2 + \left(n^2 - \epsilon_w\right) \frac{3}{\gamma_{sat} E} \left[\coth\left(\gamma_{sat} E\right) - \frac{1}{\gamma_{sat} E}\right], \tag{3.10}$$

where $n \approx 1.33$ is the refractive index of water, $\epsilon_w \approx 80$ is the bulk dielectric permittivity of water, and $\gamma_{sat} = \alpha_d \beta \mu_d$ is the parameter that defines a critical electric field $E_{sat} = 1/\gamma_{sat}$ for which the dielectric saturation occurs with $\beta = 1/(k_B T)$. Here, $\alpha_d = \sqrt{73}\left(n^2 + 2\right)/6 \approx 5.4$ and μ_d is the effective dipole moment of water molecules. Adopting the value $\mu_d \approx 2$ Debye at room temperature, gives $\gamma_{sat} \approx 9$ nm/V [105, 109, 110, 111, 112, 113, 114]. Note that $\epsilon_{Booth}(E)$ in Equation (3.10) is an even function of $E = -\frac{d\phi}{dx}$. The Booth model shows that the dielectric permittivity of water is greatly reduced by increasing electric field (Figure 3.2). Sine the field magnitudes for which the reduction occurs are well within the range for the graphene-based FET considered in this work, inclusion of the saturation effect into the Poisson-Boltzmann model is necessary. A full derivation of the Booth model is presented in Appendix C.

3.3.2 Dielectric Decrement

The strong electric field not only affects the solvent molecules at zero ion concentration, but also the solute (salt) ions. The electrolytic solution contains dissociated ions and normally has a smaller dielectric constant than the solvent (in this case water). When the ions dissolve, they create dielectric “holes” in the solution, which result in an overall decrease in the dielectric permittivity [120]. Because the ions also have charge, they create a local electric field. The dipole moment of the water molecule now not only orients with the macroscopic electric field, but it will also tend to reorient due to local charged ions giving rise to the excess polarizabilities α_+ for positive solvated ions and α_- for negative solvated ions (Figure 3.1). As a result, fewer solvent molecules are available to provide dielectric screening of the macroscopic electric fields in the solution with increasing ion concentration. This effect is known as dielectric decrement in the solvent and is especially prevalent in concentrated electrolytes, where crowding at the charged electrode interface occurs [102, 103, 108, 120, 121, 122, 123].

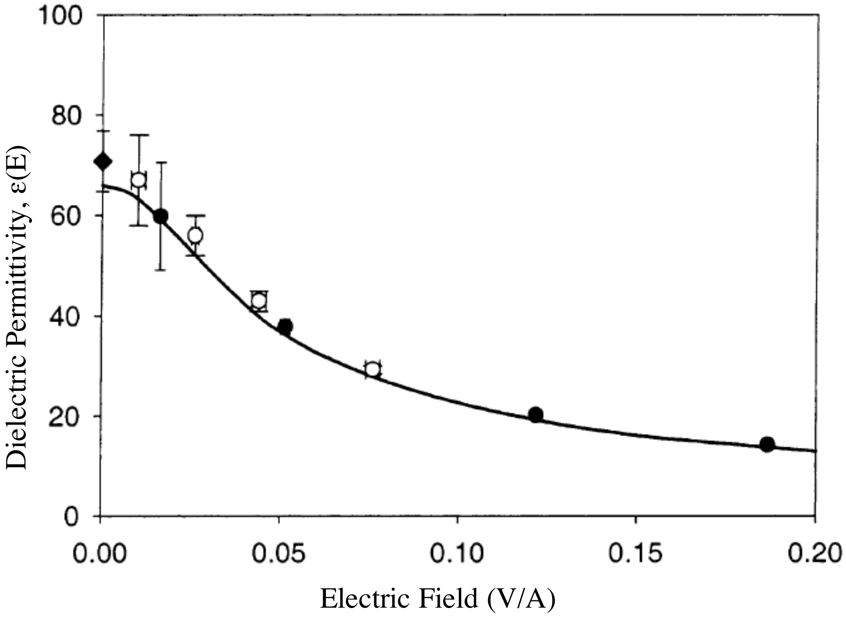

Figure 3.2: Comparison of the relative dielectric permittivity of water. Solid line shows the prediction from the Booth model, Equation (3.10) and the dots show the predictions from molecular dynamics simulations. The dipole moment for water was taken to be 1.85 Debye. Adapted from [119].

Again, following the work by Sandberg [104], the self-energy of the electric field is:

$$w_e(\|\nabla\phi\|, c_+, c_-) = \frac{1}{4\pi} \int_0^{\|\nabla\phi\|} \epsilon(c_+, c_-) E \, dE \tag{3.11}$$

$$= \frac{\epsilon_{\text{dec}}(c_+, c_-)\|\nabla\phi\|^2}{8\pi}, \tag{3.12}$$

where in contrast to Equation (3.3) above, the dielectric decrement effect results in an ion concentration dependent dielectric permittivity. Cations and anions are assumed to be the same size, $a_+ = a_- = a$, and the excess polarizabilities of positive and negative ions are assumed to be the same, $\alpha_+ = \alpha_- \equiv \alpha \geq 0$, so that the linearized model for dielectric decrement may be written as [103, 120, 121, 122, 124]

$$\epsilon_{\text{dec}}(c_+, c_-) = \epsilon_w - \alpha(c_+ + c_-). \tag{3.13}$$

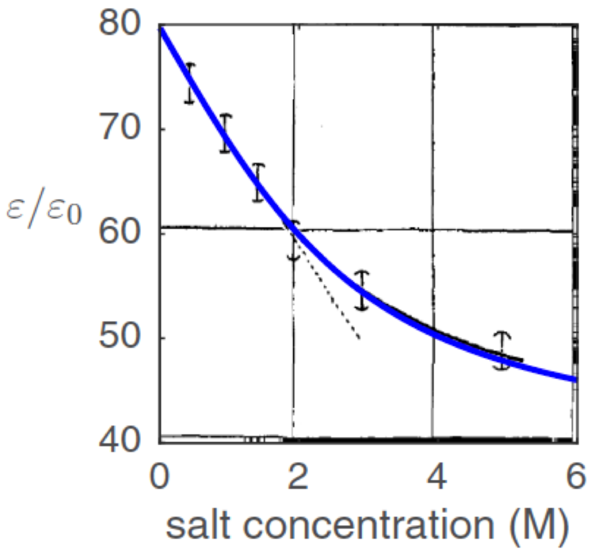

Figure 3.3: Comparison between the predicted dielectric permittivity and the experimentally measured dielectric permittivity as a function of ion concentration. The thin dotted line shows the linear approximation for dielectric decrement given by Equation (3.13). The data shown here is for an electrolytic solution of sodium chloride, NaCl. Adapted from [108].

Figure 3.3 shows the comparison between the linear approximation for dielectric decrement and experimental data for the dielectric decrement. Note that the linear approximation shows good agreement for concentrations up to 2 M, and that the dielectric permittivity becomes greatly reduced with increasing ion concentration.

Typical ion polarization values $\alpha_{\pm}$ are given in Table 3.1. The majority of the experimental data for aqueous electrolytes [16, 18, 99, 125] are obtained at ionic concentrations below 2 M, where a linearized decrement model is valid [124]. Under these conditions, an analytic solution for the capacitance is possible[41]. It is interesting to note that some work to utilize a non-linearized model for dielectric decrement was done by Nakayama *et. al* [121].

Minimizing the free energy, Equations (3.1) and (3.2), with respect to ion concentrations yields a generalized Boltzmann distribution of ions in the presence of a non-constant

Cation	$4\pi\alpha_+$ (M^{-1})	Anion	$4\pi\alpha_+$ (M^{-1})
H^+	17	F^-	5
Li^+	11	Cl^-	3
Na^+	8	I^-	7
K^+	8	OH^-	13

Table 3.1: Measured values of ion polarization for cations and anions that are common in experiments [102, 124].

electrical potential ϕ may be found from [101, 102, 105, 106]

$$\frac{\delta F}{\delta c_\pm} = \iiint \Bigg[\frac{\partial w_e(||\nabla\phi||, c_+, c_-)}{\partial c_\pm} \pm ze\phi - \mu_\pm \\ + k_B T \ln(a^3 c_\pm) - k_B T \ln(1 - a^3 c_- - a^3 c_+)\Bigg] v d^3\vec{r} = 0, \quad (3.14)$$

with v belonging to the set of all admissible variations of the Helmholtz free energy (Appendix A). Substitution of the concentration modified self-energy (Equation (3.12)) and the concentration dependent dielectric permittivity (Equation (3.13)) into Equation (3.14) gives modified ion concentrations of

$$c_\pm = \frac{c_\infty e^{\mp ze\beta\phi} e^{-\frac{\alpha\beta}{8\pi}\|\nabla\phi\|^2}}{1 - \nu + \nu e^{-\frac{\alpha\beta}{8\pi}\|\nabla\phi\|^2}\cosh(ze\beta\phi)}, \quad (3.15)$$

and charge density of

$$\rho = \frac{-2zec_\infty e^{-\frac{\alpha\beta}{8\pi}\|\nabla\phi\|^2}\sinh(ze\beta\phi)}{1 - \nu + \nu e^{-\frac{\alpha\beta}{8\pi}\|\nabla\phi\|^2}\cosh(ze\beta\phi)}. \quad (3.16)$$

Note that the unmodified Boltzmann distribution for point ions with zero excess polarizability (Equation 2.18 on Page 20) is obtained by $\nu \to 0$, where the ions become point charges, and $\alpha \to 0$, where the effects of dielectric decrement are removed.

The generalized Poisson-Boltzmann equation in the presence of dielectric decrement and steric effects is obtained by minimizing the free energy, Equations (3.1) and (3.2), with respect to potential ϕ,

$$\nabla \cdot [\epsilon_{\mathrm{dec}}(c_+, c_-)\nabla\phi] = -4\pi\rho, \quad (3.17)$$

where the volume charge density, $\rho = ze(c_+ - c_-)$, is expressed using Equation (3.15). If ϵ_{dec} is constant, i.e. $\alpha = 0$, then Equation (3.17) is reduced to the modified Poisson-Boltzmann model with ion steric effects described by the Bikerman-Freise model [65, 126], given by Equation 2.19 on Page 20.

3.4 Analytic Solution to the First Integral

A key quantity of interest in experiments is the differential capacitance, as it is and plays a key role in supercapacitor applications. In order to obtain expressions for the capacitance of the diffuse layer, it is necessary to have a relation between the potential ϕ and the electric field, $\|\nabla\phi\|$, which can be readily linked to the charge density via Gauss' law. As a consequence, the first integral of the modified Poisson-Boltzmann equations is necessary. Due to the large area of the electrode with planar surface relative to the overall size of the system, the expressions for the modified Poisson-Boltzmann equations may be reduced from 3D partial differential equations to 1D ordinary differential equations. From now on, the substitution $\|\nabla\phi\| = |E|$ and $\frac{d\phi}{dx} = -E$ will be made for the electric field, as the derivative of the potential is only with respect to the distance from the electrode–electrolyte interface x.

Solving the generalized Poisson-Boltzmann equation in Equations (3.9) and (3.17) in one dimension (1D) for diffuse layer (i.e. the region $x \in [0,\infty)$), requires two boundary conditions for the potential $\phi(x)$: one at the interface with the electrode (graphene) at $x = 0$, where the potential is the value at the interface, i.e. $\phi(0) = \phi_0$, and one in the bulk of the electrolyte where the potential goes to zero, $\phi(x) \to 0$ (Figure 3.4).

For details on the derivation of the Euler-Lagrange equations from the free-energy Lagrangian, see Appendix D. Owing to the fact that the free energy functional (Equations (3.1) and (3.2)) is not explicitly dependent on the position of the ions, x, the first integral is obtained from the Euler-Lagrange equations via Beltrami's identity. To arrive at an analytic solution for the first integral, the alternate form of the Euler-Lagrange equation may be used:

$$\frac{\partial f}{\partial x} - \frac{d}{dx}\left(f - y_x \frac{\partial f}{\partial y_x}\right) = 0, \tag{3.18}$$

where f is a known function of $y(x)$, $y_x(x)$, and x. If the Lagrangian is independent of the position variable, x, and x is explicitly absent, the Euler-Lagrange equation further simplifies to the Beltrami Identity:

$$f - y_x \frac{\partial f}{\partial y_x} = C, \tag{3.19}$$

where C is a constant determined by the boundary conditions. In this work, the function f will be the integrand in the free energy of the system, $y(x) = \phi(x)$, and $y_x = \frac{d\phi(x)}{dx}$. To keep the notation compact, the explicit position-dependence in the potential $\phi(x)$ and the concentrations $c_\pm(x)$ will be suppressed in what follows.

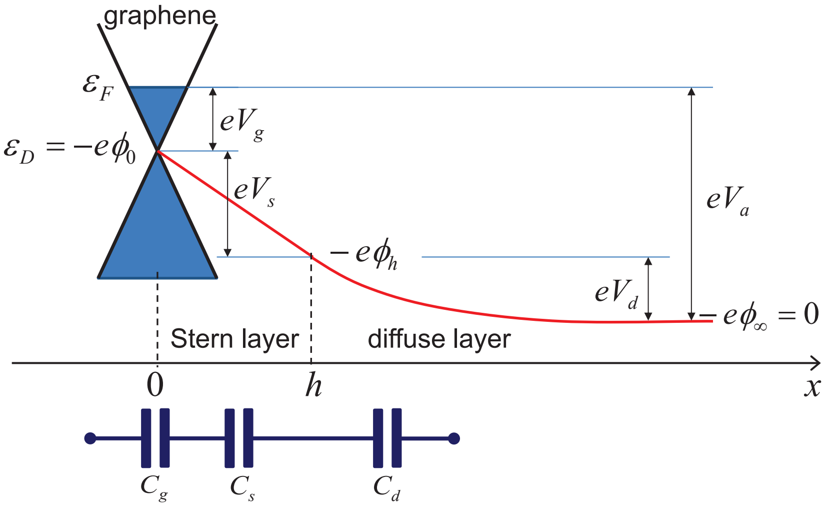

Figure 3.4: Schematic diagram showing the electrostatic potential $\phi(x)$ (red curve) as a function of distance x in an electrolytically top-gated graphene, along with electron energies at: the Fermi level ε_F in graphene, the Dirac point $\varepsilon_D = -e\phi(0) \equiv -e\phi_0$, the Stern plane $-e\phi(h) \equiv -e\phi_h$ and deep in the bulk electrolyte $-e\phi(\infty) \equiv -e\phi_\infty$, taken to be zero. Also shown are the potential differences that occur: inside graphene at $x = 0$ giving rise to its doping, $V_g = \phi_0 + \varepsilon_F/e$, across the Stern layer, $V_s = \phi_h - \phi_0$ for $0 \leq x \leq h$, and across the diffuse layer, $V_g = -\phi_h$ for $x \geq h$, so that the total applied top gate potential is $V_a = \varepsilon_F/e = V_d + V_s + V_g$. Here, $e > 0$ is the proton charge.

Dielectric Saturation

In the case of dielectric saturation, the Beltrami identity gives:

$$\begin{aligned}\Big[- w_e(|E|) + ze(c_+ - c_-)\phi - \mu_+ c_+ - \mu_- c_- \Big] \\ + \frac{k_B T}{a^3}\Big[a^3 c_+ \ln(a^3 c_+) + a^3 c_- \ln(a^3 c_-) + (1 - a^3 c_+ - a^3 c_-) \ln(1 - a^3 c_+ - a^3 c_-) \Big] \\ + E\left[\frac{\epsilon_{Booth}}{4\pi} E \right] = C. \qquad (3.20)\end{aligned}$$

By imposing the boundary condition $\phi = 0$ at $x \to \infty$, substituting in Equations (3.5), and (3.6), and rearranging, the final expression is:

$$-4\pi w_e(|E|) + \epsilon_{Booth}E^2 = \frac{8\pi c_\infty}{\beta\nu}\ln\left(1 + 2\nu\sinh^2\left(\frac{ze\beta\phi}{2}\right)\right). \tag{3.21}$$

By applying the Booth model for dielectric saturation for ϵ_{Booth} and the equation for the self energy (Equation (3.3)), the left hand side becomes:

$$\frac{n^2\,(E)^2}{2} + \frac{3(\epsilon_w - n^2)}{\gamma_{sat}}\left[\ln\left(\frac{\sinh(\gamma_{sat}E)}{\gamma_{sat}E}\right) - \gamma_{sat}E\coth\left(\gamma_{sat}E\right) - 1\right], \tag{3.22}$$

which is consistent with [40] where separation of variables was used to compute the first integral. Making the substitution for the potential drop across the diffuse layer $V_d = \phi_\infty - \phi_h = -\phi_h$ (due to $\phi_\infty = 0$), Equations (3.21) and (3.22) can be solved for V_d in the case of dielectric saturation (DS) as:

$$V_d^{DS} = 2\text{arcsinh}\left[\sqrt{\frac{1}{2\nu}\left(e^{\frac{\nu}{g^2}G(E_h)} - 1\right)}\right], \tag{3.23}$$

where $g = \gamma_{sat}/(e\beta\lambda_D) \approx 0.7\sqrt{c}$, E_h is the electric field at $x = h_+$, and

$$G(E_h) = \frac{1}{2}\left(\gamma_{sat}E_h\right)\left(\frac{n^2}{\epsilon_w} + 6\left(1 - \frac{n^2}{\epsilon_w}\right)\left(\coth\left(\gamma_{sat}E_h\right) - \frac{1}{\gamma_{sat}}E_h\ln\left(e\frac{\sinh(\gamma_{sat}E_h)}{\gamma_{sat}E_h}\right)\right)\right). \tag{3.24}$$

Note that the potential drop across the diffuse layer due to dielectric saturation, V_d^{DS}, is now a function of the electric field E_h evaluated at the interface of that layer with the Stern layer, or with the electrode in the case $h = 0$. Using Gauss' law, E_h can be related to the total charge density per unit area in the diffuse layer, σ_d.

Dielectric Decrement

In the case of dielectric decrement, the Beltrami identity gives:

$$\begin{aligned}
&-\frac{\epsilon_{\text{dec}}}{8\pi}E^2 + ze(c_+ - c_-)\phi - \mu_+c_+ - \mu_-c_- \\
&\qquad + \frac{k_BT}{a^3}\left(a^3c_+\ln(a^3c_+) + a^3c_-\ln(a^3c_-) + (1 - a^3c_+ - a^3c_-)\ln(1 - a^3c_+ - a^3c_-)\right) \\
&\qquad - E\left[-\frac{\epsilon_{\text{dec}}E}{4\pi} - \frac{E^2}{8\pi}\left(\frac{4\alpha c_\infty(\frac{\alpha\beta}{8\pi})e^{\frac{\alpha\beta}{8\pi}E^2}\cosh(ze\beta\phi)(1-\nu)}{(1 - \nu + \nu e^{\frac{\alpha\beta}{8\pi}E^2}\cosh(ze\beta\phi))^2}\right)E\right] = C.
\end{aligned} \tag{3.25}$$

Applying the same boundary conditions as in the saturation case (i.e. $\phi = 0$ at $x \to \infty$) and rearranging gives the final expression as:

$$\frac{E^2}{8\pi}\left[\epsilon_w - 2\alpha\rho_+\right] = \frac{2c_\infty}{\beta\nu}\ln\Big[1-\nu+\nu e^{-\frac{\alpha\beta}{8\pi}E^2}\cosh(ze\beta\phi)\Big]\,, \tag{3.26}$$

where

$$\begin{align} \rho_+ &= c_+ + c_- \tag{3.27} \\ &= \frac{2c_\infty e^{-\frac{\alpha\beta}{8\pi}E^2}\cosh(ze\beta\phi)}{1-\nu+\nu e^{-\frac{\alpha\beta}{8\pi}E^2}\cosh(ze\beta\phi)}. \tag{3.28} \end{align}$$

Making the substitution for the potential drop across the diffuse layer $V_d = \phi_\infty - \phi_h = -\phi_h$ (due to $\phi_\infty = 0$), Equation (3.26) can be solved for V_d in the case of dielectric decrement (DD) as

$$V_d^{DD} = \frac{1}{ze\beta}\,\mathrm{arccosh}\left(\frac{1-\nu}{\nu}\,\mathrm{e}^{\tilde{\alpha}\tilde{E}^2}\left[-1+\frac{2\tilde{\alpha}\tilde{E}^2}{\mathcal{L}(\tilde{E})}\right]\right)\,, \tag{3.29}$$

where $\mathcal{L}(\tilde{E}) = \mathrm{W}\Big(2\tilde{\alpha}\tilde{E}^2(1-\nu)\mathrm{e}^{\left(2\tilde{\alpha}-\frac{\nu}{2}\right)\tilde{E}^2}\Big)$, with W being the Lambert-W function. Here, auxiliary dimensionless variables $\tilde{\alpha} = \alpha c_\infty/\epsilon_w$, and $\tilde{E} = E_h/E_c$, where $E_c = \sqrt{8\pi c_\infty/\left(\beta\epsilon_w\right)}$ comes from normalizing the potential by $\phi_c = ze\beta$ and distance from the electrode interface, x, by the Debye length, i.e. $x_c = \lambda_D = \sqrt{\epsilon_w/8\pi\beta z^2e^2c_\infty}$ (the distance into the electrolyte for which a charge carrier is felt).

3.5 Diffuse Layer Capacitance

The differential capacitance of the diffuse layer per unit area is defined to be $C_d = \frac{d\sigma_d}{dV_d}$, where σ_d is the total charge density per unit area in diffuse layer and $V_d = -\phi_h$ is the potential drop across that layer [40]. Using Gauss' law, the charge density in the diffuse layer is $\sigma_d = -\epsilon_h E_h/\left(4\pi\right)$, where E_0 is the value of the electric field E in the diffuse layer evaluated at $x = h^+$, the interface between diffuse layer and the Stern layer, ϵ_h is the dielectric permittivity at the interface, set to $\epsilon_{Booth}(x = h)$ when considering dielectric saturation alone, and $\epsilon_{dec}(x = h)$ when considering dielectric decrement alone. In the case of a vanishing Stern layer, $h = 0$ so that E_0 and $\epsilon(x = 0)$ then refer to values evaluated at the interface between the diffuse layer and electrode (graphene).

Bazant *et al.* [48] showed that the diffuse layer capacitance may be generally expressed as $C_d = -\rho_h/E_h$, where $\rho_h = ze\left(c_+(E_h) - c_-(E_h)\right)$ is the volume charge density in the electrolyte evaluated at the interface $x = 0$. The form comes from exploiting the definition of the surface charge density of the diffuse layer, $\sigma_d = \int\limits_0^\infty \rho(\phi, E)dx$, and making a change of variables from position x to potential ϕ. Equations (3.21) and (3.26) can then be solved numerically for E_h in terms of ϕ_h and then used in the expressions for ion concentrations at $x = h$ to evaluate the diffuse layer capacitance C_d for any given value of the potential, $\phi_h = -V_d$. Then, the diffuse layer capacitances are written as

$$C_d^{DS} = \frac{C_D}{\tilde{E}} \frac{\sinh(ze\beta V_d^{DS})}{1 - \nu + \nu \cosh(ze\beta V_d^{DS})} \tag{3.30}$$

$$C_d^{DD} = \frac{C_D}{\tilde{E}} \frac{e^{-\tilde{\alpha}\tilde{E}^2} \sinh(ze\beta V_d^{DD})}{1 - \nu + \nu e^{-\tilde{\alpha}\tilde{E}^2} \cosh(ze\beta V_d^{DD})}, \tag{3.31}$$

where $C_D = \epsilon_w / (4\pi\lambda_D)$ is the Debye capacitance. In the limit of large diffuse layer potential, the capacitance for all cases exhibit a universal square root dependence on the potential. This limit can be found by replacing $\cosh(ze\beta V_d)$ by $e^{ze\beta|V_d|}/2$ and $\sinh(ze\beta V_d)$ by $e^{ze\beta|V_d|}/2$, and neglecting the terms which are not exponentially large [48, 65, 102]. For the case of steric effects, the large potential limit is $C_d^* \sim 1/\sqrt{ze\beta|V_d| + \ln(\nu/2)}$, for dielectric saturation and steric effects, the large potential limit is $C_d^{DS*} \sim 1/\sqrt{2ze\beta\nu|V_d|}$, and for dielectric decrement and steric effects, the large potential limit is $C_d^{DD*} \sim 1/\sqrt{ze\beta|V_d| + \ln(2\tilde{\alpha})}$ [41, 48, 65]. Interestingly, the high potential limits for steric effect and for dielectric decrement are quite similar.

Results & Discussion

In Figures 3.5, 3.6, and 3.7, the diffuse layer capacitance, C_d is explored for several model combinations. Physically, C_d is the differential capacitance of the interface of the diffuse layer and an ideal metallic electrode without a Stern layer between them. When expressing the bulk concentration of ions, c_∞, molar units are used, where M=mole/litre, and denote the numerical value of the concentration by c. Similarly, ion polarizability α is expressed in units of M^{-1}.

Figure 3.5 shows the Poisson-Boltzmann capacitance given by Equation (2.25) on Page 21 and the capacitance in the case of steric effects, which is given by Equation (3.30) with the corresponding potential V_d for steric effects. The Poisson-Boltzmann equation gives capacitances which are "U"-shaped at both large and small concentrations. When the ions are considered to have a finite size, i.e. in the case of steric effects, the capacitance exhibits a maximum value, and gives rise to either camel-shaped or bell-shaped capacitances. In the

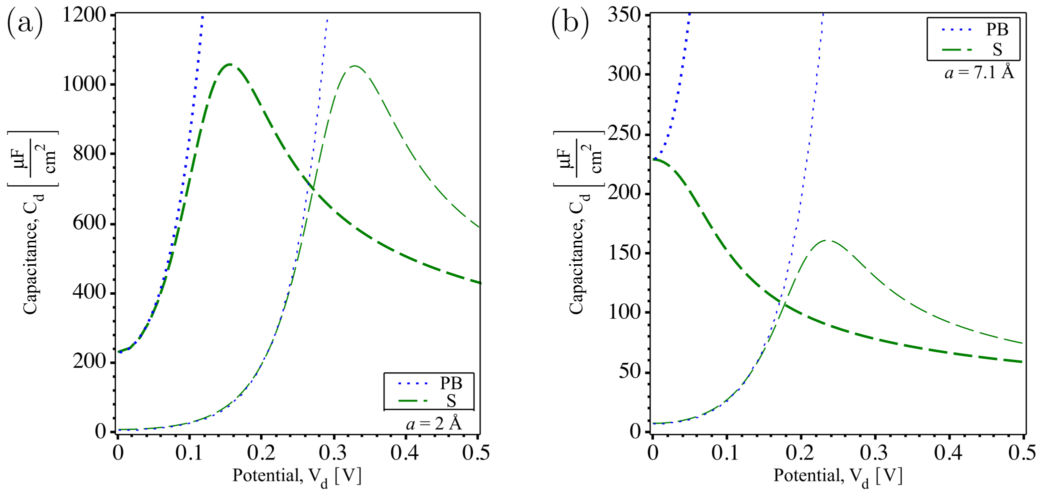

Figure 3.5: Comparisons of the diffuse layer capacitance for the case of the Poisson-Boltzmann model, where ions are treated as point charges, and the case of steric effects, where the finite size of ions is considered. The thin lines show a concentration of $c = 10^{-3}$ M and the thick lines a concentration of $c = 1$ M. Panel (a) shows the results for when the ion size is $a = 2$ Å and panel (b) shows the results for when the ion size is $a = 7.1$ Å.

case of smaller ions, "camel" shaped capacitances occur, with maxima much larger than the corresponding maxima in the case of large ions. In the case of large ion size, panel (b), the maximum in the capacitance occurs at the minimum of the "U"-shaped capacitance of the Poisson-Boltzmann model, yielding a transition from a local minimum in the capacitance to a local maximum for large ion concentrations. In the case of lower concentrations, "camel"-shaped capacitance occur with the maxima shifted to slightly lower potentials for larger ion sizes.

In panel (a) of Figure 3.6, the case of dielectric saturation without steric effects is shown (B curve), along with the Poisson-Boltzmann (PB curve) capacitance. The Booth model only gives an offset to the U-shaped capacitance of the Poisson-Boltzmann model in the form of a closely-spaced local peak-and-valley pair. In panels (b) and (c), finite ion size is introduced into the dielectric saturation model (B+S curves) for two ion sizes: $a = 2$ Å in panel (b) and $a = 7.1$ Å in panel (c). The capacitance in these panels becomes "camel"-shaped, except in the case of large concentration, $c = 1$ M, and large ion size, $a = 7.1$ Å, where the capacitance is bell-shaped and forms a local maximum at $V_d = 0$. Note how for small ions, two peaks occur in the capacitance: one primary peak, evident in all panels,

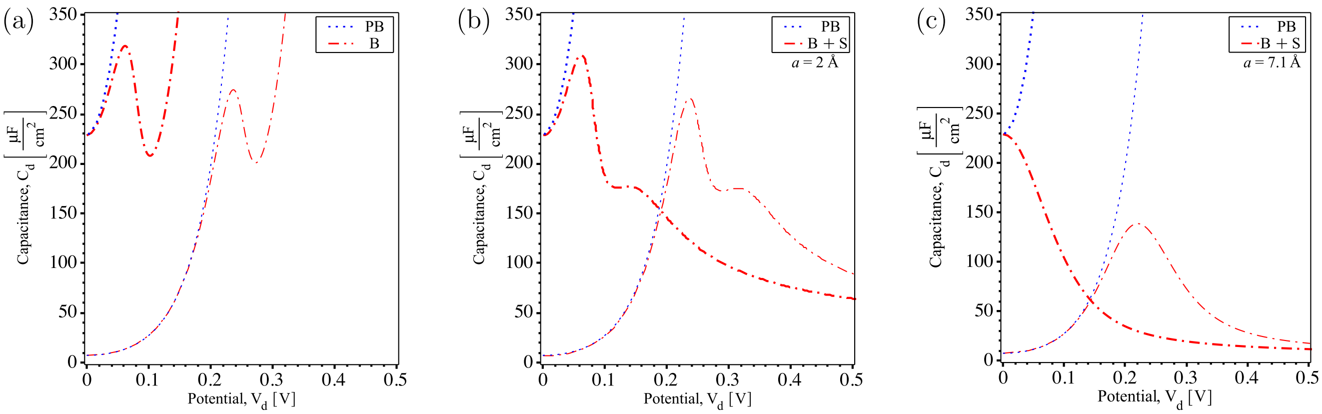

Figure 3.6: Comparisons between the Poisson-Boltzmann (PB) capacitance and the capacitance arising from the case of dielectric saturation via the Booth model (B). Panel (a) shows the case for point ions, where only the Booth model is considered in the case of dielectric saturation. Panels (b) and (c) show the case of dielectric saturation with steric effects (B+S) for two ion sizes: a small ion size of $a = 2$ Å and a large ion of $a = 7$ Å. The thin lines indicate a small ion concentration of $c = 10^{-3}$ M and the think lines indicate a large ion concentration of $c = 1$ M.

due to the dielectric saturation effects, and a secondary peak due to steric effects in the diffuse layer [40]. In the case of larger ions, the secondary peak is removed, suggesting that for high enough potentials and small enough ion sizes, a secondary peak is possible. While currently no experimental evidence for a secondary peak has been reported, a set of data for a sodium fluoride, NaF, aqueous solutions showed “camel-shaped” capacitance, which is converted to a “bell-shaped” capacitance with increasing ion concentration, with a clear upturn of the capacitance for large values of the potential [117, 118]. In contrast, a set of data for a potassium hexafluorophosphate (KPF_6) aqueous solution only showed a “camel-shaped” capacitance with no upturn for large potentials [127]. If the upturn for the NaF data is considered to be an onset of the secondary peak, which is not fully resolved because of a limited range of the applied potential in the experiment [117, 118], then the size of hydrated ions in the NaF solution maybe small enough to be comparable to the critical ion size [40], whereas the size of hydrated ions in the KPF_6 solution is sufficiently larger than the critical a and hence no upturn is observed [127]. While this seems like a plausible hypothesis, it should be mentioned that all the attempts at modelling these experiments included some form of a Stern layer, either in combination with the Grahame model for dielectric saturation, [117, 118] or in combination with the Bikerman-Freise model for steric effects [48, 103, 122].

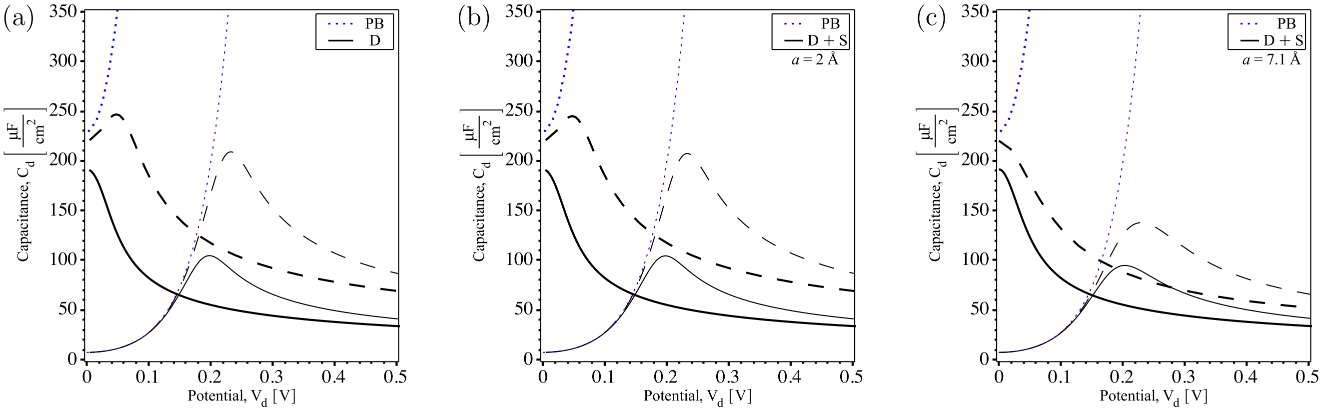

Figure 3.7: Comparisons between the Poisson-Boltzmann (PB) capacitance and the capacitance arising from the case of dielectric decrement (D) for two ion polarizations: $\alpha = 3$ M^{-1} (black dashed lines) and $\alpha = 12$ M^{-1} (black solid lines). Panel (a) shows the case for point ions, where only the Booth model is considered in the case of dielectric saturation. Panels (b) and (c) show the case of dielectric decrement with steric effects (D+S) for two ion sizes: a small ion size of $a = 2$ Å and a large ion of $a = 7$ Å. The thin lines indicate a small ion concentration of $c = 10^{-3}$ M and the thick lines indicate a large ion concentration of $c = 1$ M.

Figure 3.7 shows a comparison between the Poisson-Boltzmann capacitance and the case of dielectric decrement (D) without steric effects for a low polarizability of $\alpha = 3$ M^{-1} (black dashed lines) and high polarizability of $\alpha = 12$ M^{-1} (black solid lines). In all panels, the dielectric decrement gives rise to camel-shaped capacitances, with increasing polarizability giving peaks which are smaller in magnitude. Increasing the ion size from panel (b) to panel (c) shows that for lower polarizations, the peak in the capacitance sees a larger reduction in magnitude, showing that for lower polarizations (black dashed lines), a strong interplay between the dielectric decrement and steric effects occurs. For larger polarizations (solid black lines), panels (b) and (c) show little difference in capacitance magnitude, suggesting that the dielectric decrement effect prevails over ionic steric effects. The characteristic"U"-shaped capacitance of the Poisson-Boltzmann model is changed to a camel-shaped capacitance at low ion concentrations, $c = 10^{-3}$ M, and for low ion polarizabilities when the ion size is small enough. At large concentrations and high polarizabilities, the capacitance is bell-shaped, with a local maximum at potential $V_d = 0$.

To explore the behaviour of the transition between the camel- to bell-shaped capacitance in the case of dielectric saturation, the differential capacitance C_d^{DS}, Equation (3.30) is expanded for small potential V_d, Equation (3.23), and then the second derivative is taken to find the criteria for the transition from a local minimum to a local maximum. This gives a generalized condition of:

$$3\nu - 1 + (\epsilon_w - n^2)\frac{16\pi c_\infty}{5\beta E_{sat}^2} > 0, \tag{3.32}$$

where $E_{sat} = 1/\gamma_{sat} \sim 1$ V/nm is the critical electric field at which dielectric saturation occurs within the Booth model [113], which is valid for small diffuse layer potentials $|V_d^{DS}| \ll 1$ V. For an ion size of $a = 7.1$ Å, the critical ion concentration for the cross-over from camel- to bell-shaped capacitance occurs at $c > 0.66$ M. In the case of steric effects alone, i.e. $\gamma \to 0$ the condition for the cross-over becomes $\nu > 1/3$, confirming the result derived by Kornyshev [65]. For this case, when $a = 7.1$ Å, the critical concentration is $c > 0.77$ M, which is slightly higher than the critical concentration for dielectric saturation and steric effects. This critical concentration is confirmed in Figure 3.8, where the critical concentration falls between the dashed green and dashed black lines in both panels.

Using the parametric representation of the relation between the dielectric decrement capacitance C_d^{DD} in Equation (3.31) and the diffuse layer potential V_d^{DD} in Equation (3.29), a generalized condition for the transition from camel- to bell-shaped capacitance for dielectric decrement can be expressed as

$$48\nu\tilde{\alpha}^2 - 40\tilde{\alpha}^2 - 24\nu\tilde{\alpha} + 16\tilde{\alpha} + 3\nu - 1 > 0, \tag{3.33}$$

where $\tilde{\alpha} = \alpha c/\epsilon_w$, and is valid for small potential $|V_d^{DD}| \ll 1$ V. This cross-over criterion is found in the same way as the dielectric saturation criteria, where Equations (3.29) and (3.31) are expanded for small potential V_d, and then the second derivative is taken to find the critical point. Using an ion size of $a = 7.1$ Å, the critical ion concentrations for the "camel" to "bell" transition is $c > 0.61$ M for $\alpha = 3$ M^{-1} and $c > 0.34$ M for $\alpha = 12$ M^{-1}. These critical concentration values are corroborated by the curves in Figure 3.8, where for small polarizations, the transition occurs between the solid green and solid black lines in panel (a) and for high polarizations, the transition occurs between the solid blue and solid green lines in panel (b).

Figures 3.5, 3.6, 3.7, and 3.8 showcase that the effects added to the Poisson-Boltzmann model, cause a transition in the diffuse layer capacitance C_d from a "U"-shaped dependence to either a camel-shaped or bell-shaped capacitance. The latter arises only for large ion concentrations and large ion sizes, where a maximum is obtained at $V_d = 0$. In the case of

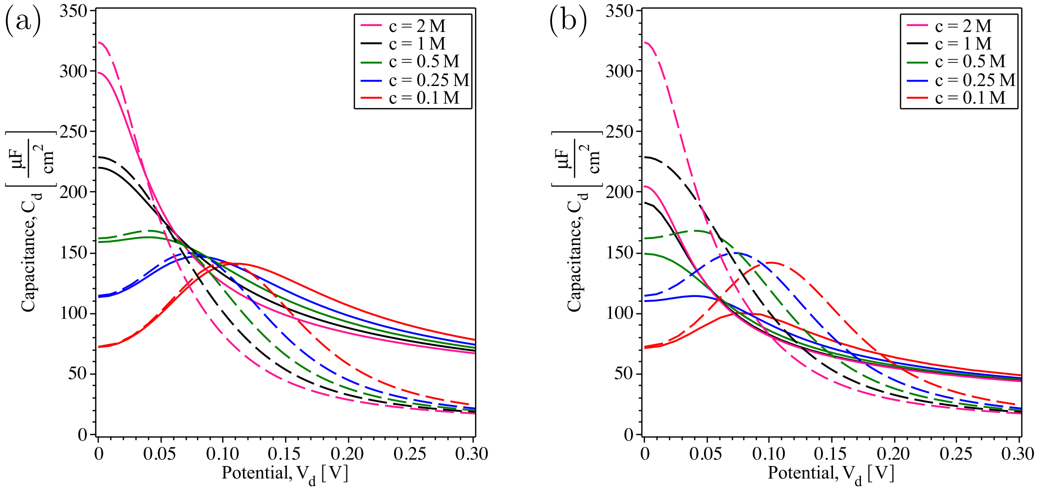

Figure 3.8: A comparison of the diffuse layer capacitance for dielectric saturation, and the diffuse layer capacitance for dielectric decrement. Dashed lines show the capacitance for the case of dielectric saturation, C_d^{DS}, and solid lines show the capacitance for dielectric decrement, C_d^{DD}. Panel (a) shows the results for a polarization of $\alpha = 3$ M^{-1} and panel (b) shows the results for polarization $\alpha = 12$ M^{-1}. Curves are shown for concentrations $c = 0.1$M to $c = 1$ M, and for ion size $a = 7.1$ Å.

dielectric saturation (Figure 3.6) a dramatic effect is observed, where a sharp lowering of the diffuse layer capacitance C_d for large V_d occurs after the peak positions, whereas the lowering is more broad in the case of steric effects (Figure 3.5) and dielectric decrement (Figure 3.7). This effect can be seen from the large potential limits of the diffuse layer capacitances, where the capacitance for dielectric saturation decays as $\sim 1/\sqrt{2ze\beta\nu|V_d|}$, where as both steric effects and dielectric decrement decay as $\sim 1/\sqrt{ze\beta|V_d| + \ln(\nu/2)}$ and $\sim 1/\sqrt{ze\beta|V_d| + \ln(2\tilde{\alpha})}$, respectively. In the cases where only dielectric saturation and dielectric decrement are considered, i.e. panels (a) in Figures 3.6 and 3.7, the capacitance arising from the Booth model in the case of dielectric saturation increases without bound for increasing potential V_d in a manner that parallels the increase in the Poisson-Boltzmann model, unlike the capacitance arising from dielectric decrement which decays following the inverse square root asymptotics given above. Note how in the case of dielectric saturation (Figure 3.6), the addition of steric effects bring the high potential end of the curve back down to more physical values of capacitance, whereas in the case of dielectric decrement (Figure 3.7), the addition of steric effects has minimal impact on the curves, but does result in a minor reduction in magnitude of the capacitance. In the case of dielectric decrement, the effect of including steric effects is minimal for small ions, which could be due to the fact that the magnitude of the ion polarizability partially accounts for the size of ions.

3.6 Inclusion of a Stern Layer

In this section, a structure consisting of an ideal metallic electrode, a Stern layer, and a diffuse layer in the electrolyte is considered. In addition to the modifications to the dielectric permittivity and finite ion size effect, a Stern layer will be considered in tandem with the already established effects. The Stern layer is considered to be a uniform, charge-free compact layer of thickness h positioned between the diffuse layer and charged electrode [66]. While the Stern layer is itself a form of steric effect, unlike the addition of steric effects in the electrolyte, the Stern layer introduces the finite size of ions at the interface (boundary) between the electrode and the electrolyte. This layer is characterized by its dielectric permittivity, ϵ_s, which is assumed to be constant, and gives rise to a constant electric field in the layer. Hence, the electric field in the Stern layer is also constant and is given by $E_s = (\phi_0 - \phi_h)/h$, where $\phi_0 \equiv \phi(0)$ is the surface potential and $\phi_h \equiv \phi(h)$ is the potential at the boundary $x = h$ between the Stern and diffuse layers (Figure 3.4).

Besides imposing continuity of the electric potential, the electrostatic jump conditions for the electric field $E(x) = -\frac{d\phi(x)}{dx}$ must be satisfied at $x = 0$ and $x = h$. Assuming a zero electric field in the region $x < 0$, the electric field at $x = 0^+$ can be written as

$$\epsilon_s E_s = 4\pi\sigma_g, \tag{3.34}$$

where σ_g is the surface charge density on the ideal metallic electrode, while the jump condition for the electric field at $x = h$ is

$$\epsilon_h\, E_h = \epsilon_s E_s, \tag{3.35}$$

with ϵ_h as the dielectric permittivity at $x = h$ and the electric field $E_h = -\frac{d\phi}{dx}\Big|_{x=h^+}$ evaluated at the inner edge of the diffuse layer.

To specify the parameters which characterize the Stern layer, it is reasonable to choose its thickness to be $h = a/2$, asserting that ions cannot approach graphene at distances shorter than their radius [111, 112]. By choosing $h = a/2$, the Stern layer is consistent with the physical meaning of the parameter a in the Bikerman-Freise model for steric effects. Generally, the dielectric permittivity of water in the Stern layer, ϵ_s, is considered to be reduced with respect to its value in the diffuse layer, although no consensus exists as to how ϵ_s can be determined. It has been speculated that a finite jump in the solvent dielectric permittivity occurs as the boundary between the Stern layer and the diffuse layer is crossed [128, 129, 130]. In the absence of specific ion adsorption at the boundary between the Stern and diffuse layers or when accumulation of the polarization charge is ignored, it is plausible to suggest that the electric field is continuous at the Stern plane $x = h$, i.e. $E_s = E_h$ [111, 112]. The jump condition in Equation (3.35) requires that $\epsilon_s = \epsilon_{\text{Booth}}(E_h)$ for dielectric saturation, allowing the overall dielectric permittivity in the electrolyte to be a continuous function for all $x > 0$, while maintaining consistency with the modified Poisson-Boltzmann equations. Similar reasoning leading to continuous dielectric permittivity at the interface with Stern layer can also be applied for dielectric decrement.

From Figure 3.4, the potential drop across the diffuse layer is $V_d \equiv \phi_\infty - \phi_0 = -\phi_0$ for $x > h$ and the potential drop across the Stern layer is $V_s = \phi_h - \phi_0$ for $0 < x < h$, allowing the total applied gate potential to be $V_a \equiv \phi_\infty + \varepsilon_F/e = \varepsilon_F/e$, which may be decomposed as

$$V_a = V_d + V_s, \tag{3.36}$$

and the differential capacitance per unit area is

$$C_{ds}^{-1} = C_d^{-1} + C_s^{-1}, \tag{3.37}$$

using the fact that $C_s V_s = \sigma_d$ (from Equation (2.36) on Page 23). Note here that C_d is either C_d^{DS} in the case of dielectric saturation (Equation 3.30) and C_d^{DD} in the case of dielectric decrement (Equation (3.31)), and that setting $C_q \to \infty$ in Equation (3.44), i.e. allowing for a metallic electrode, returns the result in Equation (3.37). Interestingly, the connection between the Stern layer and the diffuse layer is a series connection of capacitors. Finally, note that with the above definition of the Stern layer, no new free parameters are introduced into the models, and the model must continuously adjust to changes of the electric field due to the changing surface charge density on the electrode.

Results & Discussion

Figure 3.9 shows the total capacitance of the diffuse layer modelled with a Stern layer placed adjacent the metallic electrode in the electrolyte. Both the cases of the typical Poisson-Boltzmann capacitance with a Stern layer (PB) and dielectric saturation via the Booth model with Stern layer (B+S) are shown. In the case of the Poisson-Boltzmann model, decreasing the thickness of the Stern layer allows the capacitance C_{ds} to increase without bound. In the case of dielectric saturation, the Stern layer eliminates the secondary peak seen in Figure 3.6, leaving a typical "camel"-shaped capacitance, and also eliminates the increasing capacitance without bound for high potentials in panels (a) and (b) of Figure 3.6. Increasing the ion size from $a = 2$ Å in Panel (a) to $a = 7.1$ Å in Panel (b) causes a large drop in the magnitude in the capacitance, as well as a broadening of the peak. Comparing Figure 3.9 to Figure 3.6, a slight shift in the maxima location to higher potentials is observed when a Stern layer is included.

For the dielectric decrement case, the results for the diffuse layer capacitance when a Stern layer is included adjacent to the metallic electrode are shown in Figure 3.10. In both cases of polarizability, i.e. $\alpha = 3$ M^{-1} and $\alpha = 12$ M^{-1}, the peaks in the capacitance are significantly lowered from their counterparts in Figure 3.7 where no Stern layer is included. The peaks also become broadened and shift to slightly higher potentials, similar to the effect seen in the case of dielectric saturation with a Stern layer in Figure 3.9.

In both Figures 3.9 and 3.10, the Stern layer acts to decrease the magnitude of the diffuse layer capacitance, C_{ds}, and broaden the peaks, particularly in the case of large ions ($a = 7.1$ Å), where the effect of the Stern layer is stronger. The typical "camel"-shaped capacitances are observed at both high and low concentrations when the ion size is small, shown in Panel (a); when the ion size is increased, at high concentrations a bell-shaped capacitance is formed, with a maximum at $V_d = 0$. In defining the Stern layer, the parameters are chosen specifically to make them consistent with both the Bikerman-Freise and Booth models, so that no new free parameters are introduced other than the ion diameter a. By varying the value of a, results from the combined Bikerman-Freise-Booth-Stern and the dielectric decrement models can be brought to a qualitative agreement with

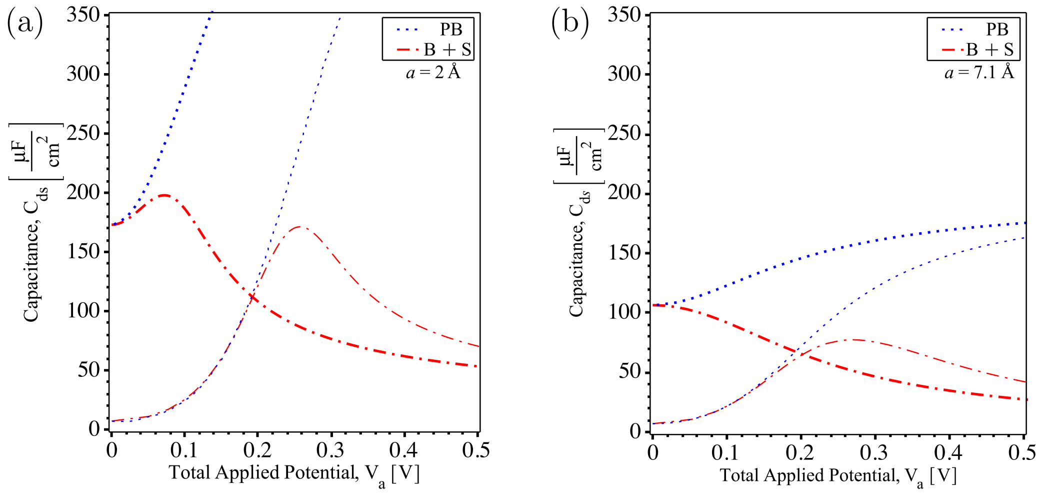

Figure 3.9: Comparisons between the Poisson-Boltzmann (PB) capacitance and the capacitance arising from the double layer consisting of a Stern layer and dielectric saturation in the electrolyte via the Booth model (B+S). The case of dielectric saturation with steric effects (B+S) is shown for two ion sizes: a small ion size of $a = 2$ Å shown in Panel (a) and a large ion size of $a = 7$ Å shown in Panel (b). The thin lines indicate a small ion concentration of $c = 10^{-3}$ M and the think lines indicate a large ion concentration of $c = 1$ M.

an array of experimental observations for differential capacitance in aqueous solutions with metallic electrode [117, 127].

3.7 Modifications for a Graphene Electrode

In this section, a structure consisting of an interface of a graphene electrode and the diffuse layer in the electrolyte. Unlike metallic electrodes, graphene exhibits strong effects due to the smallness of its quantum capacitance near the Dirac point (or point of zero charge), which is a consequence of the low-energy properties of the electronic band structure in carbon-based materials. To change from a metallic electrode to a graphene electrode, a single sheet of large area graphene is placed at $x = 0$. Then the surface potential on graphene ϕ_0 defines the Dirac point of its π electron bands as $\varepsilon_D = -e\phi_0$, as shown in Figure 3.4. Note that the charge density in graphene in Equation (2.14) on Page 18 and

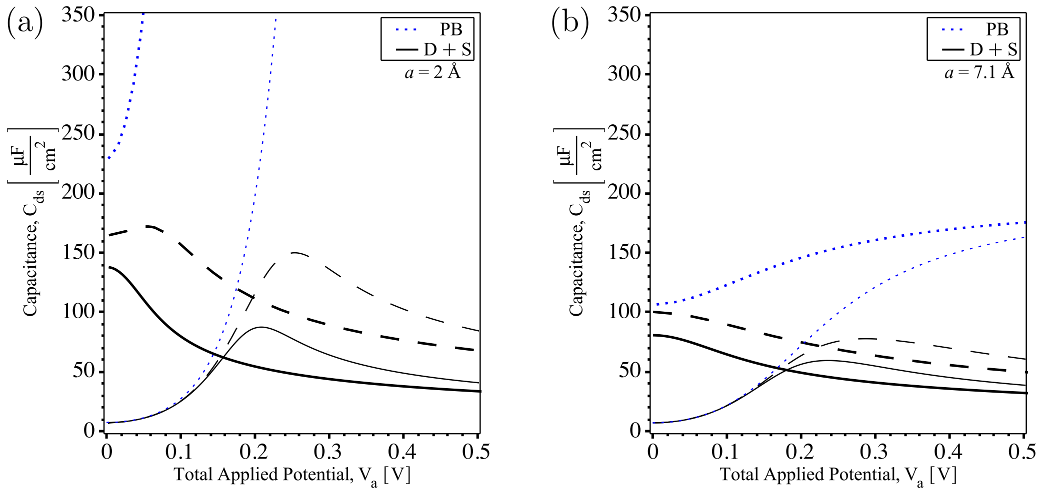

Figure 3.10: Comparisons between the Poisson-Boltzmann (PB) capacitance and the capacitance arising from the double layer consisting of a Stern layer and dielectric decrement (D+S) in the electrolyte for two ion polarizations: $\alpha = 3$ M^{-1} (black dashed lines) and $\alpha = 12$ M^{-1} (black solid lines). The case of dielectric decrement with steric effects (D+S) for two ion sizes: a small ion size of $a = 2$ Å shown in Panel (a) and a large ion size of $a = 7$ Å shown in Panel (b). The thin lines indicate a small ion concentration of $c = 10^{-3}$ M and the think lines indicate a large ion concentration of $c = 1$ M.

its quantum capacitance in Equation (2.41) on Page 25 are determined by the potential difference $V_g \equiv (\varepsilon_F - \varepsilon_D)/e = \phi_0 + \varepsilon_F/e$. When $\beta e|V_g| \gg 1$ it follows from Equation (2.14) on Page 18 that $C_q \approx e^2\mathcal{D}(e|V_g|)$, whereas for $|V_g| \lesssim 1$ V one can invoke the linearized density of states given by $\mathcal{D}(\epsilon) \approx \frac{2|\epsilon|}{\pi(\hbar v_F)^2}$, where $v_F \approx 10^6$ m/s is the Fermi speed of graphene [8].

For the doping densities of interest in sensor applications, it suffices to use the linearized approximation for the density of states. The quantum capacitance attains a minimum value of $C_g^{min} = 4e^2 \ln(2)/\left[\pi\beta(\hbar v_F)^2\right] \approx 0.8\ \mu\text{F/cm}^2$ for $V_g = 0$ at room temperature and exhibits a linear increase with the potential according to $C_q \approx \beta e|V_g|C_0/\ln(4)$ for $\beta e|V_g| \gtrsim 1$, which is a signature of the Dirac cone, or the massless Dirac fermions approximation for the π electron bands in graphene [8, 95].

From Figure 3.4 (omitting the Stern layer by setting the thickness $h \to 0$), the potential drop across the diffuse layer is $V_d \equiv \phi_\infty - \phi_0 = -\phi_0$ for $x > h$ and the potential drop across the graphene layer is $V_g = \phi_0 + \varepsilon_F/e$, allowing the total applied gate potential to be

$V_a \equiv \phi_\infty + \varepsilon_F/e = \varepsilon_F/e$, which may be decomposed as

$$V_a = V_d + V_g, \tag{3.38}$$

and the differential capacitance per unit area is given by

$$\begin{align} C_{dq}^{-1} &= \frac{dV_a}{d\sigma_d} \tag{3.39} \\ &= \frac{dV_d}{d\sigma_d} + \frac{dV_g}{d\sigma_d} \tag{3.40} \\ &= \frac{1}{C_d(V_d)} + \frac{1}{C_q(V_g)}, \tag{3.41} \end{align}$$

where the charge neutrality condition, $\sigma_d(V_d) + \sigma_g(V_g) = 0$, has been used, C_d is the capacitance of the diffuse layer, and C_q is the quantum capacitance of graphene. This series connection of the diffuse layer and the graphene electrode is the same result obtained via setting $C_s \to \infty$ in Equation (2.38) on Page 24, i.e. removing the Stern layer from the electrolyte.

Results & Discussion

In Figure 3.11, the cases for the Poisson-Boltzmann model, where ions are treated as point charges and as having finite ion sizes are considered when a graphene electrode is used. At both 10^{-3} M and 1 M, the quasi-linear dependence of the total potential C_{dq} on the total applied potential V_a comes from the characteristic V-shaped dependence of the quantum capacitance C_q of graphene on its doping potential V_g. It should be mentioned that, owing to the smallness of the quantum capacitance C_q with respect to the diffuse layer capacitance C_d, a much larger fraction of the total applied potential, $V_a = V_g + V_d$, goes to doping the graphene, i.e., $V_a \approx V_g \gg V_d$ [40, 41].

Probably the most dramatic effect of reducing the ion size is observed when the total capacitance C_{dq} is only modelled by including the ion steric effects via the Bikerman-Friese model. The broad peak at $V_a \sim 2$ V at finite ion sizes, (S curve), in panel (b) completely disappears at the smaller ion size in panel (a). Moreover, at smaller ion sizes, the capacitances accounting for steric effects practically coincide with the Poisson-Boltzmann capacitance of point ions ($a = 0$). This is consistent with the observation made by Bazant *et al.* [48] in studying the Bikerman-Friese model, where unreasonably large ion sizes had to be used to give rise to "camel-shaped" capacitance for metallic electrodes in aqueous solutions.

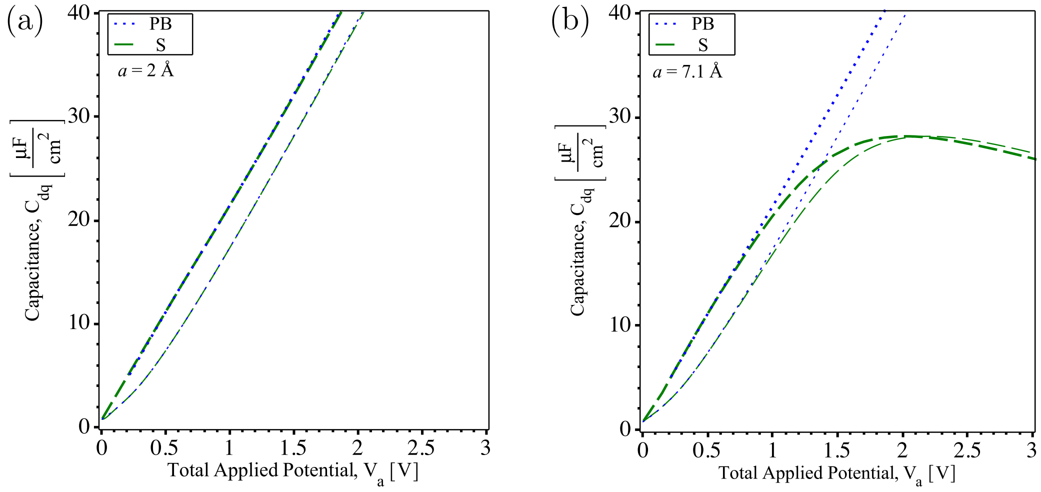

Figure 3.11: Comparisons of the total capacitance of a series connection between the capacitance arising from a graphene electrode and the diffuse layer capacitance. Two situations are included for the diffuse layer: the Poisson-Boltzmann (PB) model where ions are treated as point charges and the steric (S) model where ions have finite sizes. The thin lines show a concentration of $c = 10^{-3}$ M and the thick lines a concentration of $c = 1$ M. Panel (a) shows the results for when the finite ion size is $a = 2$ Å and panel (b) shows the results for when the finite ion size is $a = 7.1$ Å.

Figure 3.12 shows the results for the Poisson-Boltzmann model (PB) and the dielectric saturation model (B) when a graphene electrode is used. Only a relatively small change in the shape of the total capacitance C_{dq} is observed when the ion concentration changes from $c = 1$ M (thick lines) to $c = 10^{-3}$ M (thin lines). In Panels (a) and (b), a small and shallow minimum occurs in the case of dielectric saturation, which is a remnant from the secondary peak observed in the diffuse layer (see Figure 3.6, panels (a) and (b)). In panels (b) and (c), a maximum in the total capacitance C_{dq} occurs at approximately ~ 1.5 V for small ion sizes, $a = 2$ Å, and at approximately ~ 1 V for large ion sizes, $a = 7.1$ Å. With increasing ion size, this peak becomes sharper, as well as smaller in magnitude. When compared to their metallic electrode counterparts in Figure 3.6. the peaks are smaller in magnitude and shift to higher potentials, owing to the fact that the quantum capacitance of graphene C_q is much smaller than that of the diffuse layer C_d, and therefore dominates the total capacitance.

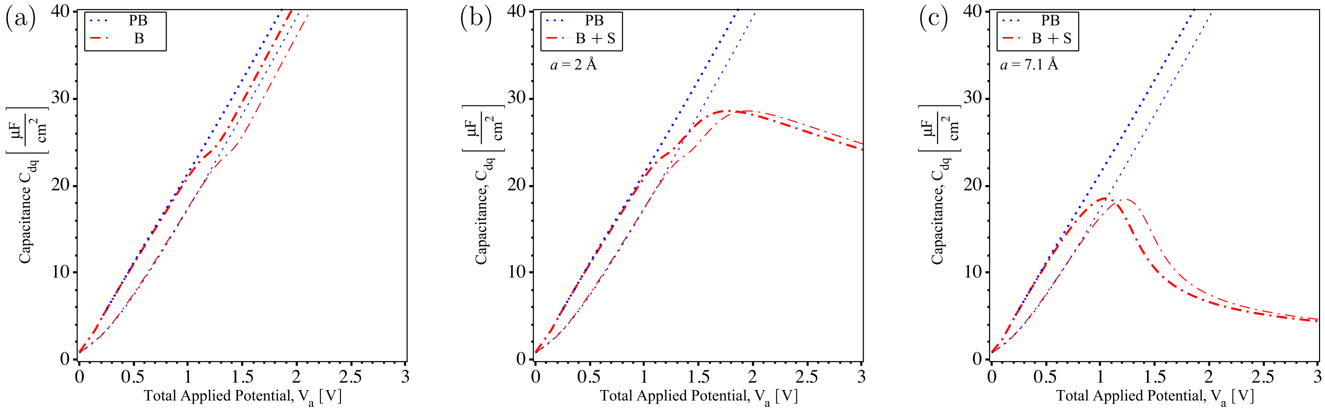

Figure 3.12: Comparisons of the total capacitance for a series connection between the capacitance arising from a graphene electrode and the diffuse layer capacitance. In the diffuse layer, the Poisson-Boltzmann (PB) capacitance and the capacitance arising from the case of dielectric saturation via the Booth model (B) are used. Panel (a) shows the case for point ions, where only the Booth model is considered in the case of dielectric saturation. Panels (b) and (c) show the case of dielectric saturation with steric effects (B+S) for two ion sizes: $a = 2$ Å and $a = 7$ Å. The thin lines indicate an ion concentration of $c = 10^{-3}$ M and the thick lines indicate a large ion concentration of $c = 1$ M.

In Figure 3.13, the total capacitance according to the Poisson-Boltzmann (PB) and the dielectric decrement (D) models are shown for a graphene electrode. When compared to their metallic electrode counterparts in Figure 3.7, the same features are evident. Increasing the ion size from point ions to small ions, and then to large ions reveals a strong interplay between the steric effects and the dielectric decrement effect at low polarizations. For large polarizations, very little difference between the capacitance curves is observed, again, suggesting that the effect of dielectric decrement prevails over the finite size of ions in this case. Similar to Figures 3.11 and 3.12, the peaks in the capacitance are lower in magnitude and shifted to higher potentials, when compared to a metallic electrode (Figure 3.7) showcasing again the smallness of the quantum capacitance of graphene, C_q.

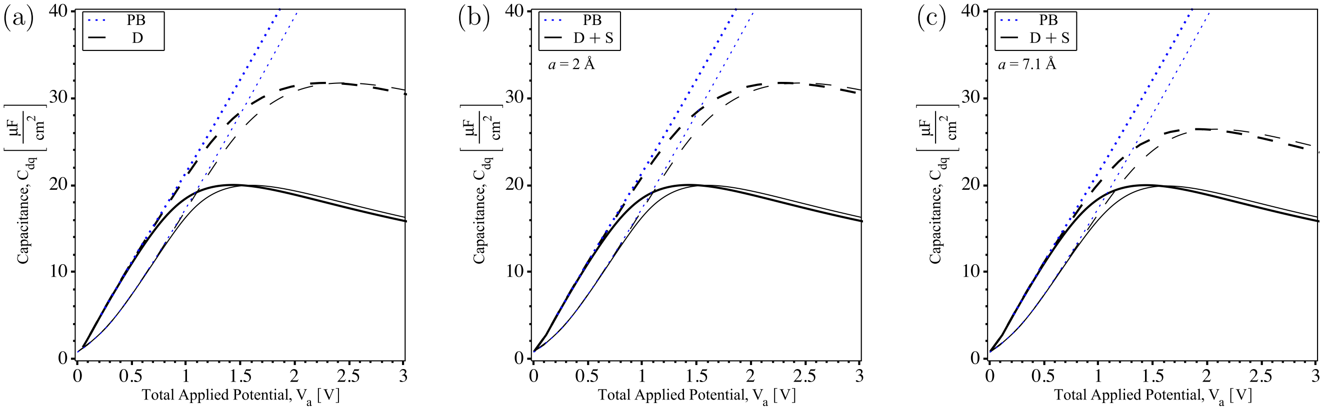

Figure 3.13: Comparisons of the total capacitance for a series connection between the capacitance arising from a graphene electrode and the diffuse layer capacitance. In the diffuse layer, the Poisson-Boltzmann (PB) capacitance and the capacitance arising from the case of dielectric decrement (D) for two ion polarizations: $\alpha = 3$ M^{-1} (black dashed lines) and $\alpha = 12$ M^{-1} (black solid lines) are used. Panel (a) shows the case for point ions, where only the Booth model is considered in the case of dielectric saturation. Panels (b) and (c) show the case of dielectric decrement with steric effects (D+S) for two ion sizes: $a = 2$ Å and $a = 7$ Å. The thin lines correspond to ionic concentrations of $c = 10^{-3}$ M and the thick lines to a concentration of $c = 1$ M.

The curves for the dielectric decrement and steric effects (D+S) case in panels (b) and (c) of Figure 3.13 exhibit a broad peak at the potentials $1 \lesssim V_a \lesssim 2.5$ V, which persists even in the limit of point ions (panel (a)). Given the uncertainty regarding the appropriate choice for ion sizes [48], it seems that only a combination of the ion steric effects with dielectric decrement is capable of giving rise to a stable, broad peak in the total capacitance C_{dq} at applied potentials $V_a \gtrsim 1$ V. While conclusive evidence for such "camel-shaped" capacitance of electrolytically gated graphene is still missing, the data reported by Du *et al.* [131] does show some asymmetrically positioned, broad peaks in the total capacitance at relatively large applied potentials.

3.8 Total Capacitance

A structure consisting of a graphene electrode, Stern layer, and diffuse layer in the electrolyte (Figure 3.4) is considered here. From Figure 3.4, the potential drops (or voltages) across graphene are $V_g = \phi_0 + \varepsilon_F/e$, $V_s = \phi_h - \phi_0$ for $0 < x < h$ across the Stern layer, and $V_d \equiv \phi_\infty - \phi_h = -\phi_h$ for $x > h$ across the diffuse layer. Thus, the total applied gate potential, $V_a \equiv \phi_\infty + \varepsilon_F/e = \varepsilon_F/e$, may be decomposed as

$$V_a = V_d + V_s + V_g. \tag{3.42}$$

The inverse of the total differential capacitance of electrolytically gated graphene is given by

$$\begin{aligned} C_{dsq}^{-1} &\equiv \frac{dV_a}{d\sigma_g} \qquad (3.43)\\ &= \frac{1}{C_d(V_d)} + \frac{1}{C_s} + \frac{1}{C_q(V_g)}, \qquad (3.44)\end{aligned}$$

corresponding to a series connection of the diffuse layer capacitance, Stern layer capacitance and the graphene quantum capacitance (Figure 3.4).

It should be stressed that the values of the graphene potential V_g and the diffuse layer potential V_d, which are used in the calculations of the quantum capacitance C_q and the diffuse layer capacitance C_d are determined self-consistently by solving the equation

$$\sigma_g(V_g) + \sigma_d(V_d) = 0, \tag{3.45}$$

which expresses the charge neutrality of the structure. The expression for the surface charge density of graphene $\sigma_g(V_g)$ is given in Equation (2.15) on Page 18, whereas the surface charge density of the diffuse layer $\sigma_d(V_d)$ can be related to the values of the dielectric permittivity and the electric field at the interface of the diffuse layer and the Stern layer by Gauss' law, $\epsilon_h E_h = -4\pi\sigma_d$ in a manner that depends on the model used for modifying the Poisson-Boltzmann equation. Here ϵ_h is the dielectric permittivity at $x = h$ and E_h is the electric field at $x = h$.

To discard the Stern layer, the Stern layer potential V_s is set to zero in Equation (3.42) and the thickness $h \to 0$ so that the Stern layer capacitance $C_s \to \infty$ in Equation (3.44).

The total capacitance then becomes a series connection of the diffuse layer capacitance and the graphene quantum capacitance as given in Equation (3.41). Similarly, replacing graphene by a metallic electrode with its surface at $x = 0$ would have the potential of graphene $V_g = 0$ giving quantum capacitance $C_q \to \infty$ in Equation (3.44), so that the total capacitance of the electric double layer is a series connection of the diffuse layer capacitance and the Stern layer capacitance as given in Equation (3.37) with the total applied gate potential given by $V_a = V_d + V_s$.

Results & Discussion

In Figure 3.14, the total capacitance is shown for a graphene electrode system, where a Stern layer is included. Result from the model for both the Poisson-Boltzmann case (PB) and the dielectric saturation with steric effects case (B+S) are included. Likewise with their metallic electrode counterparts in Figure 3.9, the Stern layer results in a lowering of the magnitude and broadening of the peak in the case of dielectric saturation. The peaks in the case without Stern layer (Figure 3.12), show that the peaks for smaller ions, $a = 2$ Å, are reduced in magnitude, and that the peaks in both cases of finite ion sizes are broadened. The Stern layer also completely eliminates the remnants of the secondary peak from the diffuse layer, as is the case when a metallic electrode is considered (Figure 3.9). Although no significant shift in the position of the primary peak in the total capacitance C_{dsq} is evident, it should be emphasized that the peak broadening due to the Stern layer also affects the region of potentials V_a below that peak, where the quantum capacitance of graphene dominates the total capacitance C_{dsq}. This finding points to the importance of using a Stern layer in modeling the capacitance of electrolytically-gated graphene [40].

Figure 3.15 shows the total capacitance for the Poisson-Boltzmann model (PB) and the dielectric decrement with steric effects model (D+S). As with the results of dielectric saturation above, the Stern layer reduces the magnitude of the peaks in the dielectric decrement curves (black lines) and slightly broadens the peaks, compared to their counterparts without a Stern layer in Figure 3.13. When comparing the capacitances to their metallic electrode counterparts in Figure 3.10, it is clear that the quantum capacitance of graphene C_q dominates the total capacitance.

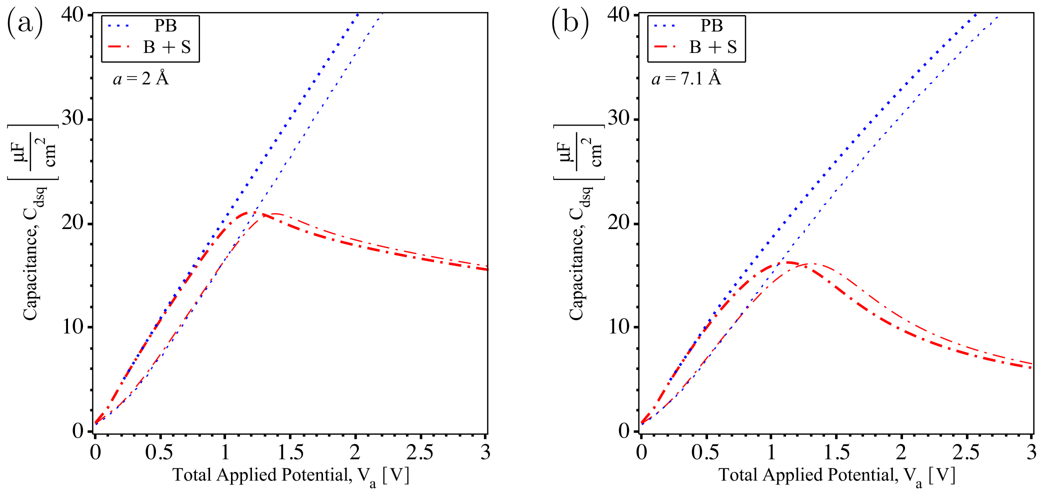

Figure 3.14: Comparisons of the total capacitance for a series connection between the capacitance arising from a graphene electrode, the capacitance of the Stern layer, and the diffuse layer capacitance. In the diffuse layer, the Poisson-Boltzmann (PB) capacitance and the capacitance arising from the case of dielectric saturation via the Booth model (B) are used. Panel (a) shows the case for point ions, where only the Booth model is considered in the case of dielectric saturation. Panel (b) shows the case of dielectric saturation with steric effects (B+S) for two ion sizes: $a = 2$ Å and $a = 7$ Å. The thin lines indicate an ion concentration of $c = 10^{-3}$ M and the thick lines an ion concentration of $c = 1$ M.

3.9 Numerical Solutions to the Modified Poisson-Boltzmann Equation

While the differential capacitance is an analytic quantity accessible through the first integral of Equation (3.9) and Equation (3.17), solutions of the Poisson-Boltzmann equation for the potential ϕ as a function of position (in this case, distance x away from the electrode) are generally not analytic due to the nonlinearity of the problem. Thus the modified Poisson-Boltzmann equation must be solved numerically.

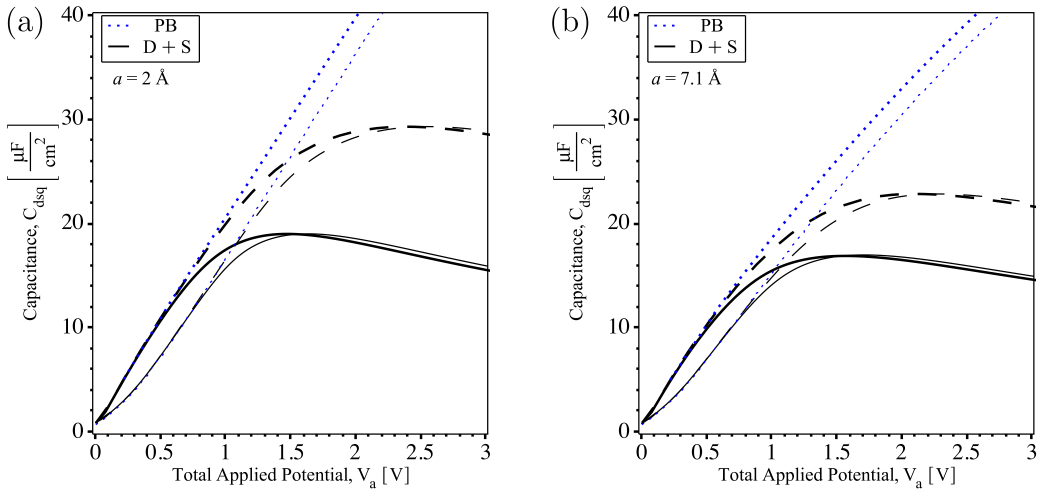

Figure 3.15: Comparisons of the total capacitance for a series connection between the capacitance arising from a graphene electrode, the capacitance of the Stern layer, and the diffuse layer capacitance. In the diffuse layer, the Poisson-Boltzmann (PB) capacitance and the capacitance arising from the case of dielectric decrement (D) for two ion polarizations: $\alpha = 3\ \mathrm{M}^{-1}$ (black dashed lines) and $\alpha = 12\ \mathrm{M}^{-1}$ (black solid lines) are used. Panel (a) shows the case for point ions, where only the Booth model is considered in the case of dielectric saturation. Panel (b) shows the case of dielectric decrement with steric effects (D+S) for two ion sizes: $a = 2$ Å and $a = 7$ Å. The thin lines indicate an ion concentration of $c = 10^{-3}$ M and the thick lines an ion concentration of $c = 1$ M.

3.9.1 Collocation Method

A well established method for solving ordinary differential equations, partial differential equations, and integral equations is the method of collocation. The method requires a finite set of candidate or test solutions, which are typically polynomials, and a set of collocation points at specific location the domain of the problem. To solve the differential equations, the method then selects the candidate solution which satisfies the problem at the collocation points while also minimizing the residual [132].

As this is a well documented method for numerical computation, many packages that implement the collocation method are available. For this work, the `solve_bvp` function from the `scipy.integrate` package in python will be used [132]. The solver requires two boundary conditions, which are chosen to be $\phi(0) = V_a$ and $\overline{\phi}(x)|_{\bar{x}\to\infty} = 0$. Here $\bar{x} = x/\lambda_D$,

$\overline{\phi}(x) = z\beta e\phi(x)$, λ_D is the Debye length, and $\overline{\rho} = \frac{\rho}{2ec_\infty}$, where $2ec_\infty$ is a measure of the total amount of charges (either positive or negative) in the bulk electrolyte.

Expressions for Second Derivative

To implement this method to find solutions in terms of position for the charge densities, Equations (3.9) and (3.17) must be expressed in the form $\phi'' = f(\phi(x), \phi'(x))$.

For the case of dielectric saturation, the dielectric permittivity is given by the Booth model in Equation (3.10), and the second derivative can be expressed by:

$$\frac{d^2\overline{\phi}^{DS}(\overline{x})}{d\overline{x}^2} = -\frac{\overline{\rho}(\overline{\phi}(\overline{x}))}{\epsilon_{Booth}\left(\frac{d\overline{\phi}(\overline{x})}{d\overline{x}}\right) + \epsilon'_{Booth}\left(\frac{d\overline{\phi}(\overline{x})}{d\overline{x}}\right)\frac{d\overline{\phi}(\overline{x})}{d\overline{x}}}, \tag{3.46}$$

where $\overline{\rho}(\overline{\phi}(\overline{x}))$ is the normalized charge density derived from Equation (3.7). In the case of dielectric decrement, the dielectric permittivity is given Equation (3.13) and the second derivative can be expressed by:

$$\frac{d^2\overline{\phi}^{DD}(x)}{d\overline{x}^2} = -\frac{\overline{\rho}_{dec}(\overline{\phi}(\overline{x}), \overline{\phi}'(\overline{x})) + \epsilon_{\text{dec},1}(\overline{\phi}(\overline{x}), \overline{\phi}'(\overline{x}))\left(\frac{d\overline{\phi}(\overline{x})}{d\overline{x}}\right)^2}{\epsilon_{\text{dec}}(\overline{\phi}(\overline{x}), \overline{\phi}'(\overline{x})) + \epsilon_{\text{dec},2}(\overline{\phi}(\overline{x}), \overline{\phi}'(\overline{x}))\left(\frac{d\overline{\phi}(\overline{x})}{d\overline{x}}\right)}, \tag{3.47}$$

where $\epsilon_{\text{dec},1}(\overline{\phi}(\overline{x}), \overline{\phi}'(\overline{x})) = \frac{\partial\epsilon_{\text{dec}}(\overline{\phi}(\overline{x}), \overline{\phi}'(\overline{x}))}{\partial\overline{\phi}(\overline{x})}$, $\epsilon_{\text{dec},2}(\overline{\phi}(\overline{x}), \overline{\phi}'(\overline{x})) = \frac{\partial\epsilon_{\text{dec}}(\overline{\phi}(\overline{x}), \overline{\phi}'(\overline{x}))}{\partial\overline{\phi}'(\overline{x})}$, and $\overline{\rho}_{dec}$ is the normalized charge density arising from Equation (3.16).

Since the overall effect of a Stern layer is to simply lower the magnitude of parameters in the system, to help elucidate the effects of steric effects, dielectric saturation, and dielectric decrement on the charge density of the system, the presence of Stern layer will be omitted.

Graphene Electrode

When a graphene electrode is considered, the total applied potential becomes $V_a = V_g + V_d$, and the charge neutrality condition becomes $\sigma_g(V_g) + \sigma_d(V_d) = 0$. Unlike the metallic electrode case, this requires an additional step in computation before the collocation can be used. Due to the surface charge on graphene σ_g, the boundary condition at $\overline{x} = 0$ applied to the electric field at the interface is $\overline{E}_0 = 4\pi\lambda_D\lambda_B\sigma_g/e$. Because σ_g is dependent on V_g, an extra step to solve for the portion of the total applied potential V_a that is diverted to graphene is required since only the total applied potential V_a is specified in the system experimentally.

3.9.2 Charge Density solutions

In Figure 3.16, the numerical solution for the positive ion charge density is plotted as a function of distance, with $x = 0$ being the electrode-electrolyte interface for electrode charge $\overline{E}_0 = 1$ and ion size $a = 0.71$ nm. Here, the positive ion charge densities are plotted rather than the overall charge densities so that comparisons can be made with previous literature results, particularly in the case of dielectric decrement. The solid lines indicate the solution for a regular metallic electrode and dashed lines show the solution for a graphene electrode. The panels consider three cases: steric effects alone (green lines), dielectric saturation and steric effects (red lines) and dielectric decrement (black lines) for $c = 10^{-3}$ M in panels (a) and (b), and $c = 1$ M in panels (c) and (d). In the case of dielectric decrement, the solution for $\alpha = 3$ M^{-1} is shown in panels (a) and (c), while the solution for $\alpha = 12$ M^{-1} is shown in panels (b) and (d).

A common pattern to the charge density profiles is evident: as one moves closer to the electrode interface, the concentration of ions builds up. At higher ion concentrations, the saturation effect drops off faster than that of the millimole case, with the latter tailing off to the bulk concentration more gradually. When additional effects, dielectric saturation and dielectric decrement, are included with the steric effect, the magnitude and thickness of the saturated layer decrease, owing to the fact that effects in the bulk electrolyte hinder the mobility of the ions. For the case of dielectric saturation, not only does the magnitude of this saturated layer decrease, but the thickness in both the low voltage cases and high voltage case is reduced, unlike the cases of dielectric decrement with steric effect and only steric effects. This may be due to the reduced mobility of the large water molecules when they align with the electric field and are less able to inhibit the movement of other ions in the electrolyte. So while a saturated layer is able to form, it could be difficult for other ions to move toward the electrode interface due to the decrease in the mobility. For the case of dielectric decrement, the increase in α corresponds to a lowering of the magnitude and the thickness of the saturated layer, owing to the fact that ions cannot as easily move towards the electrode, unlike the dielectric saturation and steric cases. In Section 3.4, the case of dielectric decrement was found to be very similar to the effect of steric effects in the electrolyte, where the dielectric decrement caused for a slightly larger overall reduction in the magnitude of the capacitance. Likewise with this result, the overall effect of dielectric decrement is quite similar in shape to that of the steric effect, particularly when the ion polarization is low.

In Figure 3.17, the numerical solution for the positive ion charge density is plotted as a function of distance, with $x = 0$ being the electrode-electrolyte interface for electrode charge $\overline{E}_0 = 5$ and ion size $a = 0.71$ nm, and for the same cases as Figure 3.16. As

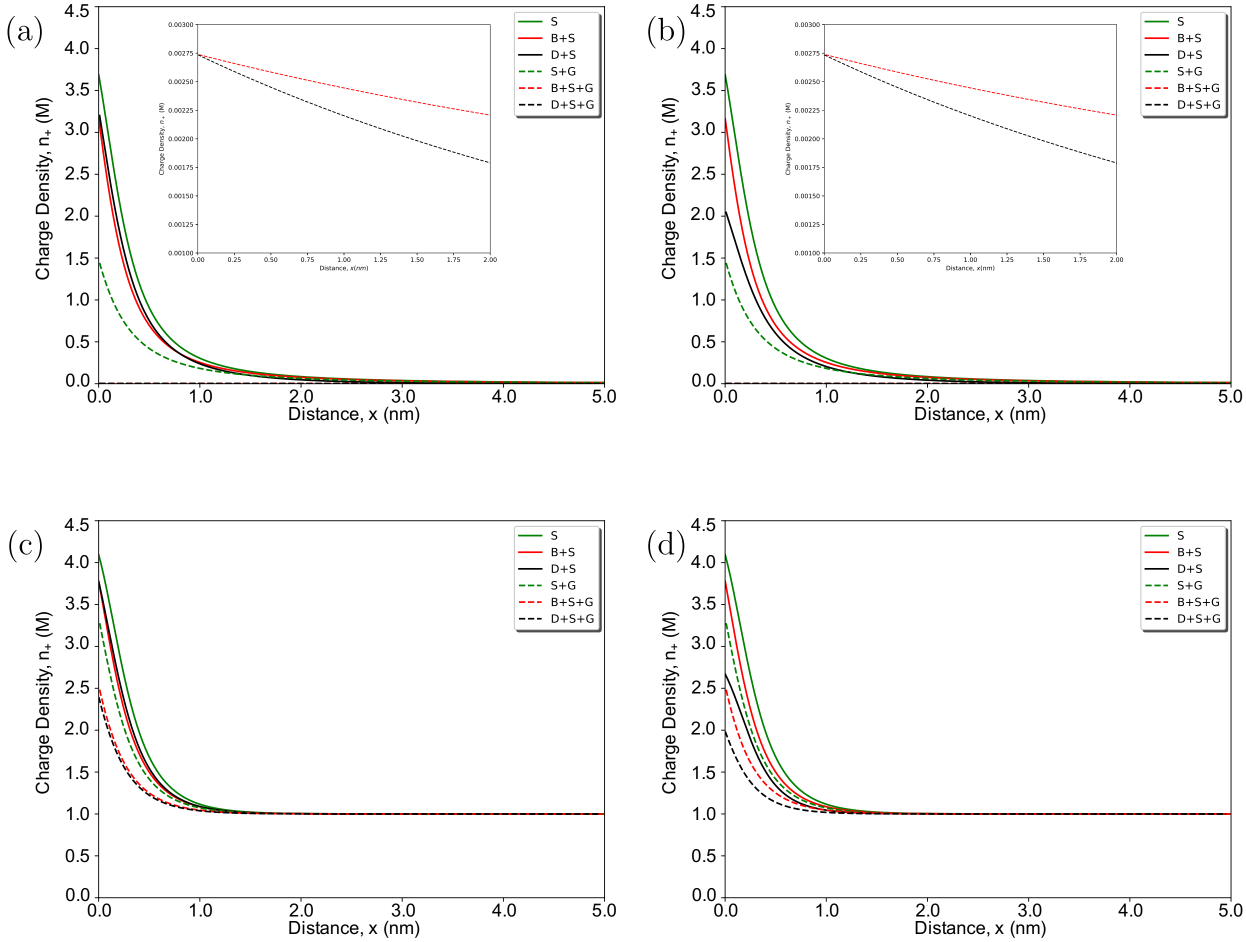

Figure 3.16: Results for the charge density of positing ions as a function of distance x from the electrode surface for $\overline{E}_0 = 1$. Panels (a) and (b) show results for $c = 10^{-3}$ M, with the insets showing a reduced axis view. Panels (c) and (d) show results for $c = 1$ M. Each panel shows models for the steric effect (S), dielectric saturation via the Booth model and steric effects (B+S), and dielectric decrement and steric effects (D+S). Solid lines indicate results for a metallic electrode and dashed lines indicate results for a graphene electrode (denoted +G in the legend).

the applied potential to the electrode is increased, the thickness of the saturated layer increases, which is comparable to the results found by Hatlo *et al*, in the case of dielectric decrement and steric effects [103]. With the increase in the electrode charge, the overall applied potential of the system is increased, which in turn gives larger potentials in both the diffuse layer V_d and graphene V_g in the case of the dashed lines. Since the potential has increased, it would be expected that this saturated layering effect would increase in thickness and magnitude [103]. As with the results in Figure 3.16, the dielectric saturation effect causes a thin saturated layer near the electrode interface, which decreases in both magnitude and thickness much more quickly than the steric effect and dielectric decrement with steric effect cases. Likewise with Figure 3.16, increasing the magnitude of the dielectric decrement, α, yields a drop in the magnitude and thickness of the saturated layer. Again, this effect is similar to the effect of steric effects on the charge density.

In both Figure 3.16 and Figure 3.17, the change from a metallic electrode to a graphene electrode, i.e. solid lines to dashed lines, has a remarkably universal effect. The use of a graphene electrode decreases the thickness of the saturated layer, and in the case of small ion concentrations, decreases the magnitude of the local concentration at the electrolyte interface. Owing to the high charge carrier density of graphene, the bulk of the applied potential, V_a, goes to charging the graphene electrode, and a small fraction of the potential goes into the diffuse layer V_d. This phenomenon is discussed in more detail in Chapter 4.

3.10 Concluding Remarks

This chapter provides an analysis of the roles of dielectric saturation and dielectric decrement in combination with finite ion size effects for the differential capacitance of electrolytically gated graphene using a mean-field theory based variational approach. Comparisons of the capacitances were made between the two models for these effects in the electrolytic solution, as well as when in a series connection with a metallic electrode and a graphene electrode. Much of the analysis is aided by the fact that expressions for the capacitance are obtained in analytic form. A thorough discussion of the diffuse layer capacitance in the cases of steric effects, dielectric saturation, dielectric saturation and steric effects, dielectric decrement, and dielectric decrement with steric effect is presented. The diffuse layer capacitances exhibited camel-shaped and bell-shaped behaviour, and criteria for the transition from one to the other was derived for both cases of dielectric saturation with steric effects and dielectric decrement with steric effects.

Emphasis was placed on the role of a charge-free Stern layer. A simple capacitor model for the Stern layer is considered with its thickness chosen in accord with the Bikerman-Freise model for ion steric effects and with the dielectric permittivity in the Stern layer

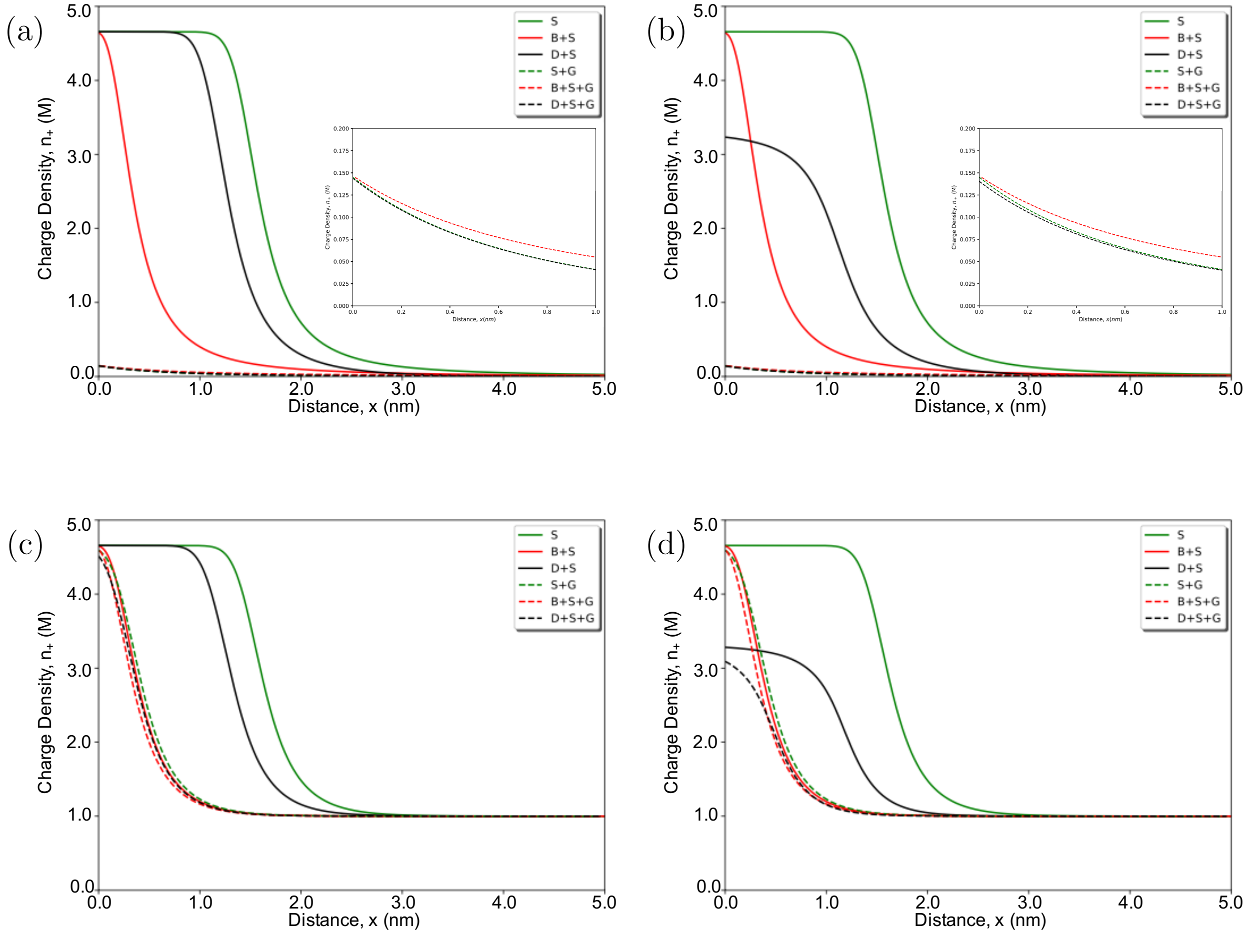

Figure 3.17: Results for the charge density of positive ions as a function of distance x from the electrode surface for $\overline{E}_0 = 5$. Panels (a) and (b) show results for $c = 10^{-3}$ M, with the insets showing a reduced axis view. Panels (c) and (d) show results for $c = 1$ M. Each panel shows models for the steric effect (S), dielectric saturation via the Booth model and steric effects (B+S), and dielectric decrement and steric effects (D+S). Solid lines indicate results for a metallic electrode and dashed lines indicate results for a graphene electrode (denoted +G in the legend).

that changes continuously across the boundary between the Stern and diffuse layers. In this way, no new free parameters are introduced in the combined Bikerman-Freise-Booth-Stern model besides the ion diameter. The inclusion of the Stern layer broadens, shifts, and reduces the overall magnitude of the primary peak with increasing ion size in a series connection of the diffuse layer capacitance and the Stern layer capacitance, C_{ds}. In the case of dielectric saturation, the Stern layer also removes the secondary peak in C_{ds} for ion sizes $a \gtrsim 1$ Å and introduces a shallow minimum beyond the primary peak, followed by a long plateau at larger potentials for the ion size $a \sim 1$ Å. By varying the value of a, results for C_{ds} from the combined Bikerman-Freise-Booth-Stern model can be brought to a qualitative agreement with experimental observations in aqueous solutions with metallic electrodes, which exhibit different behaviors of capacitance at large potentials depending of the size of ions [117, 118, 127].

Utilizing a series connection of the quantum capacitance in graphene electrode and the diffuse layer capacitance in the electrolyte the total capacitance is dominated by the quantum capacitance of graphene at applied potential $\lesssim 1$ V, as expected. At higher potential values, a peak develops in the total capacitance, which can be quite sensitive to the ion size in the presence of dielectric saturation. On the other hand, combining the finite ion size effect with dielectric decrement yields a rather stable, broad peak in the total capacitance of electrolytically gated graphene at the applied potential values $\gtrsim 1$ V, which persists even in the limit of point ions.

Including a Stern layer between graphene and the diffuse layer removes secondary peak in the capacitance C_{dq} in the case of dielectric saturation, leaving only the main peak in C_{dsq} at about 1 V, which is largely independent of the ion concentration and the value of a. The main peak in both the case of dielectric saturation and dielectric decrement is significantly broadened by the presence of the Stern layer, thereby affecting the region of low potentials where the quantum capacitance of graphene dominates. Although dielectric saturation or dielectric decrement and finite ion sizes are responsible for the appearance of a main peak at ~ 1 V in the capacitance of electrolytically gated graphene, the Stern layer plays important roles in both shaping that peak and controlling the behaviour of the capacitance at larger potentials for small ion sizes.

For the charge densities, a largely universal behaviour is exhibited, with larger applied potentials yielding a saturated layer that is larger in magnitude and thicker. The additional effects of dielectric saturation and dielectric decrement both lower the thickness and magnitude of this saturation layer, due to their impact on the mobility of ions toward the electrode surface. As expected in the case of a graphene electrode, the thickness of this layer is greatly reduced, due to the ability of graphene to take a larger portion of the applied potential than that of the diffuse layer.

The above discussion is important for future studies of modelling electrolytically gated graphene because typically quite large surface charge densities can be achieved in doped graphene, which may cause extensive ion crowding and high electric fields near graphene that may require taking into account the effects of dielectric decrement and dielectric saturation in the adjacent solution, respectively.

Chapter 4

Interface of Graphene and Room Temperature Ionic Liquid

Ionic liquids are considered to be molten salts composed of relatively large ions, which exist in a liquid state at room temperature and are more inert electrochemically than standard electrolytes [56]. As opposed to the ordinary diluted electrolytes, pure ionic liquids are characterized by high ion concentration and lack of solvent. Because of such unique properties, along with their low volatility, room temperature ionic liquids have been recently studied in the context of several applications [133, 134], including novel methods of synthesis at the nanoscale [135, 136, 137], solar cells [42], supercapacitors [43, 44, 45, 46], and efficient gating materials [47]. Due to the fact that the capacitance in ionic liquids is expected to be smaller than that of electrolytes, it is necessary to investigate the effect of the quantum capacitance of graphene on the total capacitance of the graphene–ionic liquid interface [138, 139, 140].

Modelling of ionic liquids typically follows that of electrolytic solutions, with some adjustments to the dielectric permittivity in the internal energy and the lattice-gas model for the entropy of the system. In particular, recent progress in understanding the capacitance of the electric double layer (EDL) in ionic liquids has benefitted from a landmark analysis by Kornyshev [65], which paved the way for studying ionic liquids near electrified interfaces at the level of mean-field theory by taking into account short-range correlations and finite sizes of the constituent ions. As a result, a number of publications appeared in recent years using various versions of such mean-field theories to study the differential capacitance of ionic liquids in the presence of a charged surface represented by an idealized metallic electrode [49, 57, 66, 67, 68, 69, 70, 71, 72, 141]. Many predictions of such theories were verified by computational studies of the capacitance of EDLs in ionic liquids [56, 66, 73, 142, 143].

One of the most remarkable properties of the EDL capacitance is a transition of its dependence on the potential from a camel shape to a bell shape with increasing ion packing fraction γ in ionic liquids [65], which has been corroborated in experiments [144], and is similar to the camel-to-bell shaped transition observed in electrolytic solutions. Results presented in this chapter are published in *Electrochimica Acta* [145].

4.1 Theory

Ionic liquids are known for their strong ion correlations, which could be tackled within mean-field theory by introducing non-local modifications into dielectric permittivity of ionic liquids, for example. The surface charge on the electrode can become overscreened by a monolayer of oppositely charged ions, which is then corrected by a second monolayer of ions that have opposite charge to the first monolayer of ions. To extend the previously used mean-field theory of ionic liquids and electrolytes, the next allowable potential gradient term is added to the dielectric permittivity of ionic liquids, which contains an electrostatic correlation length. The correlation term is negative to describe the overscreening effect in strongly correlated liquids, which is an electrostatic correlation [49, 67]. Due to Coulomb interactions, the dielectric permittivity can be expressed, in operator form, as $\hat{\epsilon} = \epsilon\,(1 - \ell_c^2 \nabla^2)$, where ℓ_c is an effective length scale over which ion correlation effects are important [67]. The effective length ℓ_c is attributed to the overscreening effect in the ionic liquid [146, 67]. It should be noted that the value of ℓ_c is not precisely known in ionic liquids, although, approximate bounds can be deduced: a lower bound of the ion size, a, and an upper bound of the Bjerrum length λ_B, where the electrostatic Coulomb energy becomes comparable to the thermal energy $k_B T$ [49, 67].

Following the work of Bazant *et al.* [49], a free energy model of the diffuse layer in ionic liquid results in a Landau-Ginzburg-like functional given by

$$F = \iiint \left[-w_e + \rho\phi - TS\right] d^3\vec{r}. \tag{4.1}$$

Here, w_e is the self energy of the ionic liquid, $\rho = e(z_+ c_+ - z_- c_-)$ is the charge density in the ionic liquid, $c_\pm$ is the concentration of the positive/negative ions, $z_\pm$ is the charge of the positive/negative ions, ϵ is the dielectric constant of the ionic liquid, and ϕ is the electrostatic potential. To model the electric field within the ionic liquid, the dielectric function is assumed to be the sum of a constant, ϵ, and a non-local contribution arising from the ion-ion correlations. The self-energy is given by [49]

$$w_e = \frac{\epsilon}{8\pi}\left[\|\nabla\phi\|^2 + \ell_c^2 (\nabla^2\phi)^2\right], \tag{4.2}$$

and the free energy for the ionic liquid is then

$$F = \iiint \left[-\frac{\epsilon}{8\pi} \left(\|\nabla \phi\|^2 + \ell_c^2 (\nabla^2 \phi)^2 \right) + \rho\phi - TS \right] d^3\vec{r}. \tag{4.3}$$

For simplicity, ions are considered to have equal charges, $z_+ = z_- = z$, and positive and negative ions have the same size, $a_+ = a_- = a$. Likewise with Chapter 3, a lattice-gas model for the entropic contribution is used and is given by

$$-TS = \frac{k_B T}{a^3} \iiint \left[a^3 c_- \ln(a^3 c_-) + a^3 c_+ \ln(a^3 c_+) + (1 - a^3 c_- - a^3 c_+) \ln(1 - a^3 c_- - a^3 c_+) \right] d^3\vec{r}, \tag{4.4}$$

where the first term indicates corresponds to sites occupied by negative ions, the second term represents lattice sites occupied by positive ions, and the last term represents holes in the lattice where neither positive nor negative ions are found (Figure 4.1) [49, 97].

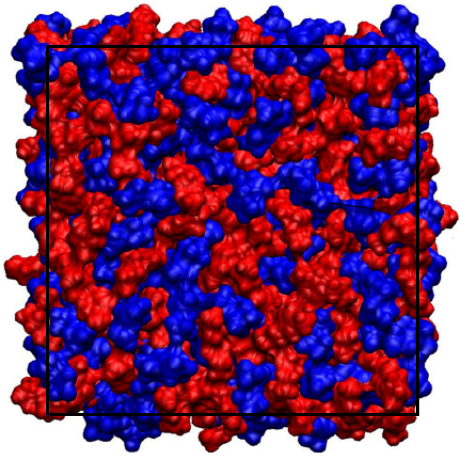

Figure 4.1: Molecular dynamics simulation of the ionic liquid 1-n-butyl-3-methylimidazolium bis(trifluoromethanesulfonyl)imide ([Bmim][TFSI]). Here, the cations are represented by the colour red and the anions by the colour blue. Note that voids in the lattice exist, which is due to the unequal packing of cations and anions into the lattice cube. Adapted from [147].

No modifications made to the free energy affect the concentration, so the minimization with respect to concentrations yields ion concentrations given by Equation (3.6) on Page 30. Note that to be consistent with the notation used in the literature on ionic liquids, the substitution $\gamma = \nu$ is made in Equation (3.6) on Page 30 [65, 148]. The minimization with respect to the potential ϕ gives a modified Poisson-Fermi equation [49],

$$(1 - \delta_c^2 \nabla^2)\nabla^2 \phi = -4\pi\rho, \tag{4.5}$$

where $\delta_c = \ell_c/\lambda_D$ is a dimensionless correlation length and $\lambda_D = \sqrt{\frac{\epsilon k_B T}{8\pi z^2 e^2 c_\infty}}$ is the Debye length in the ionic liquid. Using Equation (3.6) on Page 30 yields the charge density in the diffuse layer, $\rho(\phi;\gamma)$, with the steric effects controlled by a single parameter γ in the case of a symmetric ionic liquid.

Equation (4.5) is fourth-order and solved for $\phi(x)$ in the diffuse layer that occupies the region $x \in (0, \infty)$. Two standard boundary conditions from electrostatics are used: zero potential in the electroneutral bulk, i.e $\phi(x \to \infty) = 0$, and a prescribed potential at the interface $\phi(0) = \phi_0$, where ϕ_0 is the potential at $x = 0$. For the remaining two conditions, it will be assumed that $\phi'''(0) = 0$ and $\phi'''(x \to \infty) = 0$ so that the charge density is "flat" at the boundary (i.e. $\rho'(c_\pm) = 0$ for $x = 0$ and $x \to \infty$, coming from replacing Poisson's equation, $\epsilon\nabla^2\phi = -\rho$, into the new boundary condition). It should also be noted that these two boundary conditions which were chosen by Bazant *et al.* may be considered an approximation of boundary conditions which balance the Maxwell-stress tensor at the interface given by $\delta_c\phi'''(0) = \phi''(0)$ and $\delta_c^2\phi'''(0) - \phi'(0) = \sigma_0$, where σ_0 is the charge on the electrode [49, 67, 149]. Here, the boundary conditions used in this work can be recovered by setting $\phi''(0) = 0$ and using the fact that $\phi'(0) = \sigma_0$ which is equivalent to $\phi(0) = \phi_0$. These boundary conditions are consistent with the standard electrostatic boundary conditions and are consistent with a continuum model of finite ion size where correlation effects disappear at the interface.

Likewise with the discussion in Chapter 3, a uniform, charge-free Stern layer with thickness $\frac{a}{2}$ will be introduced between the diffuse layer and the electrode so that no new parameters are introduced [66]. Because the Stern layer is characterized by a constant dielectric permittivity, ϵ_s, it has a constant electric field. By assuming that a metallic electrode is charged by applying the potential V_a in the bulk ionic liquid, the decomposition of the potential is

$$V_a = V_d + V_s, \tag{4.6}$$

where V_d is the potential drop across the diffuse layer and V_s is the potential drop across the Stern layer, and the total capacitance for the combined diffuse and Stern layers is given by

$$\frac{1}{C_{ds}} = \frac{1}{C_d(V_d)} + \frac{1}{C_s}, \tag{4.7}$$

where C_d is the capacitance of the diffuse layer and C_s is the capacitance of the Stern layer. As expected, the capacitance is a series connection between the diffuse layer and the Stern layer, similar to the situation in Chapter 3 (Equation (3.37) on Page 47). In addition, a graphene electrode will also be considered in place of the standard metallic electrode. Following the discussion in Chapter 3, Equation (3.42) on Page 55 for the total applied potential of the system and the total capacitance (2.38) on Page 24 will be used when considering the effects of a graphene electrode in contact with an ionic liquid.

When the Stern layer is discarded and graphene is used as an electrode in an ionic liquid, the total applied potential may be written as $V_a = V_d + V_g$, where a relationship between the potential drop across graphene V_g and the potential drop in the diffuse layer V_d can be found for given V_a by using the charge neutrality condition, $\sigma_d(V_d) + \sigma_g(V_g) = 0$ [40, 41]. Here, the surface charge density in the diffuse layer is $\sigma_d(V_d)$ and the surface charge on graphene is $\sigma_g(V_g)$. The total capacitance of this structure, $C_{dq} = -d\sigma_g/dV_a$, is therefore given by a series connection of the quantum capacitance of graphene C_q and the diffuse layer capacitance C_d [25, 40],

$$C_{dq} = \left[C_d(V_d)^{-1} + C_q(V_g)^{-1}\right]^{-1}. \tag{4.8}$$

This expression can be used to discuss the relative roles of the quantum capacitance and the diffuse layer capacitance in the regime of large applied potentials.

As is the case in Chapter 3, due to the large area of the planar electrode relative to the overall size of the system, the expressions for the Poisson-Fermi equation (Equation (4.5)) may be reduced from a 3D partial differential equation to a 1D ordinary differential equation. It is also convenient to normalize the parameters of the system: $\overline{x} = x/\lambda_D$, where λ_D is the Debye screening length in the ionic liquid, $\overline{\phi} = z\beta e\phi$, and $\overline{\rho} = \rho/\left(2zec_\infty\right)$, giving the normalized Poisson-Fermi equation

$$\left(1 - \delta_c^2 \frac{d^2}{d\overline{x}^2}\right) \frac{d^2\overline{\phi}}{d\overline{x}^2} = -\overline{\rho}. \tag{4.9}$$

4.1.1 Low Voltage Solution

While the full form of the the Poisson-Fermi Equation (Equation (4.9)) coupled with the expression for the ion concentrations (Equation (3.6) on Page 30) is highly nonlinear, analytic solutions can be obtained in the low-potential limit, when the voltage is relatively small compared to the thermal voltage, $|V_d| \ll k_BT/e$. This allows for a simplification to be made in the ion concentrations, by taking the Taylor series expansion about the potential $\phi = 0$,

$$\overline{\rho} = -\frac{\sinh\left(\overline{\phi}\right)}{1-\gamma+\gamma\cosh(\overline{\phi})} \tag{4.10}$$

$$\sim \overline{\phi} \text{ as } \phi \to 0, \tag{4.11}$$

where $\gamma = 2a^3 c_\infty$ accounts for the finite size of ions. The Poisson-Fermi equation in the low potential limit then becomes:

$$\left(1 - \delta_c^2 \frac{d^2}{d\overline{x}^2}\right)\frac{d^2\overline{\phi}}{d\overline{x}^2} = \overline{\phi}, \tag{4.12}$$

which can be solved analytically [67]. Given the form of Equation (4.12), the solution is dependent on the value of δ_c, which is considered below.

"Weak" Correlation Effects

When $\delta_c < 1/2$, the ion correlations vanish well inside the diffuse layer and become subdominant to the Debye correlations. For the low potential limit, the solution is given by [67]:

$$\overline{\phi}(\overline{x}) = \frac{\overline{\phi}(0)}{1-\frac{k_1^3}{k_2^3}}\left(e^{-k_1\overline{x}} - \frac{k_1^3}{k_2^3}e^{-k_2\overline{x}}\right), \tag{4.13}$$

where $k_1 = \sqrt{\frac{1-\sqrt{1-4\delta_c^2}}{2\delta_c^2}}$ and $k_2 = \sqrt{\frac{1+\sqrt{1-4\delta_c^2}}{2\delta_c^2}}$. The diffuse layer capacitance in the weak correlation limit can then be expressed as

$$C_d^0 = -\frac{\epsilon}{4\pi}\frac{1}{\overline{\phi}(0)}\left.\frac{d\overline{\phi}}{d\overline{x}}\right|_{\overline{x}=0}, \tag{4.14}$$

$$= C_D \frac{k_1\left(1-\frac{k_1^2}{k_2^2}\right)}{1-\frac{k_1^3}{k_2^3}}, \tag{4.15}$$

where $C_D = \epsilon/4\pi\lambda_D$ is the Debye capacitance in the ionic liquid. When the effects of correlation are removed altogether, i.e. $\delta_c \to 0$, then $k_1 \to 1$ and $k_2 \to \infty$, and the solution for the potential (Equation (4.13)) becomes $\overline{\phi}(x) = \overline{\phi}(0)e^{-\overline{x}}$, which is the solution from the Debye-Hückel model when $\delta_c = 0$ [67].

“Strong” Correlation Effects

When $\delta_c > 1/2$, the ion correlation effects become more dominant than the effects of the Debye effects. The low potential limit solution is given by [67]:

$$\overline{\phi}(\overline{x}) = \overline{\phi}(0)e^{-k_3 x}\left(\cos(k_4\overline{x}) - A\sin(k_4\overline{x})\right), \tag{4.16}$$

where $k_3 = \frac{\sqrt{2\delta_c+1}}{2\delta_c}$, $k_4 = \frac{\sqrt{2\delta_c-1}}{2\delta_c}$, and $A = \frac{\sqrt{2\delta_c+1}(\delta_c-1)}{\sqrt{2\delta_c-1}(\delta_c+1)}$. In the regime of strong inter-ionic correlations and negligible steric effects in ionic liquids, the definition in Equation (4.14) then gives for the diffuse layer capacitance [49, 66, 67]

$$C_d^0 = C_D\frac{\sqrt{2\delta_c+1}}{(\delta_c+1)}. \tag{4.17}$$

4.1.2 High-Potential Analysis with Graphene Electrode

At sufficiently high potentials, $|V_d| \gg k_BT/e$, when the ion steric effects dominate and the inter-ionic correlations may be neglected [49, 56, 69], the diffuse layer capacitance exhibits a dependence on the potential given by

$$C_d^\infty \sim \sqrt{\epsilon ze/\left(8\pi a^3|V_d|\right)}, \text{ as } |V_d| \to \infty \tag{4.18}$$

which comes from replacing $\cosh(ze\beta V_d)$ by $e^{ze\beta|V_d|}/2$ and $\sinh(ze\beta V_d)$ by $e^{ze\beta|V_d|}/2$, and neglecting the terms which are not exponentially large [48, 65, 102] in Equation (3.30) on Page 40 and taking a first order asymptotic series expansion. The high potential limit of the diffuse layer capacitance is independent of both the temperature and the ion concentration in the ionic liquid [40, 49, 56, 65, 69]. When a graphene electrode is included and large chemical potentials apply, but still remaining within conditions for the Dirac cone approximation for $D(E)$, i.e., $k_BT \ll |\mu_c| \lesssim 2$ eV, Equation (2.41) on Page 25 implies that the quantum capacitance exhibits linear dependence on the charging potential, given by

$$C_q^\infty \sim \frac{2\alpha_{\text{fine}}^2}{\pi e}|V_g|, \text{ as } |V_g| \to \infty, \tag{4.19}$$

where $\alpha_{\text{fine}} = e^2/\left(\hbar v_F\right) \approx 2.2$ is the effective fine structure constant or the dimensionless coupling strength of electrons in free-standing graphene. It should be noted that the large potential $|V_g|$ behaviour of the quantum capacitance in graphene is independent of temperature, similar to that observed for the diffuse layer capacitance in ionic liquids at large $|V_d|$ values. Therefore, a transition from the linear regime to the inverse square root dependence of C_{dq} with increasing applied potential $|V_a|$ may give rise to a camel-like dependence with peaks at relatively large potentials that are independent of both the temperature and ion concentration in the ionic liquid, to the leading order.

Because this transition in the capacitance of the graphene–ionic liquid interface should be experimentally verifiable, it is worthwhile exploring its quantitative aspects on the basis of Equation (3.41) on Page 51 with C_d and C_q replaced by their large-potential limiting forms, $C_d^{\infty}(V_d)$ (Equation(4.18)) and $C_q^{\infty}(V_g)$ (Equation (4.19)), respectively. Therefore, the large-potential forms of the corresponding charge densities are $\sigma_d^{\infty} = \sqrt{\epsilon z e |V_d| / (2\pi a^3)}\,\mathrm{sign}(V_d)$ and $\sigma_g^{\infty} = -\frac{\alpha_{\text{fine}}^2 V_g^2}{\pi e}\,\mathrm{sign}(V_g)$, which come from taking the first order asymptotic expansion of the surface charge densities for the diffuse layer and for graphene, respectively. Then, by combining the charge neutrality, $\sigma_d(V_d) + \sigma_g(V_g) = 0$, with the decomposition of the applied potential, $V_a = V_d + V_g$, the capacitance in Equation (3.41) on Page 51 can be shown to reach peak values given by

$$C_{dq}^{*} = \frac{2}{3}\left(\frac{\epsilon z \alpha_{\text{fine}}^2}{2\pi^2 a^3}\right)^{1/3}, \tag{4.20}$$

for the applied potential

$$V_a^{*} = \frac{9e}{16}\left(\frac{\pi \epsilon z}{\alpha_{\text{fine}}^4 a^3}\right)^{1/3}, \tag{4.21}$$

with the potential splitting ratio at the peak given by $V_g^{*}/V_d^{*} = 8$.

4.2 Details of Computation

Unlike the case of electrolytes in Chapter 3, analytic expressions for the capacitance of the diffuse layer of the modified Poisson-Fermi equation (Equation (4.9)) are not attainable under general conditions. To obtain solutions for the differential capacitance in the ionic liquid, a numerical solver must be utilized. After computing the results, the capacitances will be further normalized by the Debye capacitance in the ionic liquid, C_D, so that comparisons can be made with previous literature on ionic liquids [49, 66, 67].

The normalization of the surface charge densities, $\overline{\sigma}_{\xi} = \sigma_{\xi}/(e n_c)$ (where $\xi = d, g$), are achieved by using the characteristic number density of ions in the diffuse layer defined by $n_c = (4\pi\lambda_D\lambda_B)^{-1}$, where $\lambda_B = \beta e^2/\epsilon$ is the Bjerrum length in the ionic liquid. The surface charge density on graphene based on the Dirac cone approximation is

$$\overline{\sigma}_g = R\left[\mathrm{dilog}\left(1 + \mathrm{e}^{\overline{V}_g}\right) - \mathrm{dilog}\left(1 + \mathrm{e}^{-\overline{V}_g}\right)\right], \tag{4.22}$$

where $R = n_g/n_c$ is a dimensionless ratio, which plays an important role in the modelling as it quantifies the relation between two subsystems: the ions in the diffuse layer in the ionic liquid and the charge carriers in graphene. Here, $n_g = \frac{2}{\pi}\frac{\alpha_{\text{fine}}^2}{(e^2\beta)^2} \approx 9.2 \times 10^{-4}$ nm^{-2} is the characteristic density of graphene at room temperature. The total normalized capacitance, for capacitors in series is Equation (2.38) on Page 24,

$$\overline{C}_{dsg} = (\overline{C}_d^{-1} + \overline{C}_s^{-1} + \overline{C}_q^{-1})^{-1}, \tag{4.23}$$

where $\overline{C}_d = C_d/C_D$ is the normalized diffuse layer capacitance, $\overline{C}_s = C_s/C_D$ is the normalized Stern layer capacitance, and $\overline{C}_q = C_q/C_D$ is the quantum capacitance of graphene. The quantum capacitance C_q is given by Equation (2.41) on Page 25, and once normalized by the Debye capacitance is:

$$\overline{C}_q = 2R \ln\left[2\cosh\left(\overline{V}_g/2\right)\right], \tag{4.24}$$

where $\bar{V}_g$ is the normalized charging potential inside. Interestingly, Equation (4.22) and Equation (4.24) feature the same ratio R. Note that the total capacitance can be modified to exclude different layers by taking that capacitance to be infinitely large (e.g. to remove the Stern layer capacitance, take $C_s \to \infty$ in Equation (4.23), which results in the capacitance without Stern layer given by Equation (3.41) on Page 51).

It should be clear that the first integral of Equation (4.5) is not tractable, and hence, analytic solutions for the surface charges and capacitances are difficult to obtain, if at all, as in the previous chapter [40, 41]. Therefore, to obtain solutions for the total capacitances the following numerical approach is used:

1. Solve the modified Poisson-Fermi equation (Equation (4.9)) over a range of surface potentials ϕ_0.

2. For each surface potential ϕ_0, find the corresponding charge density $\rho(\phi(x))$.

3. Numerically integrate the charge density $\rho(\phi(x))$, Equation (4.10) to obtain the surface charge in the diffuse layer, $\sigma_d(\phi_0) = \int \rho(\phi(x))dx$, for each surface potential ϕ_0.

4. Define the potential drop across the diffuse layer as $V_d = -\phi_0$. Then interpolate the set of diffuse layer potential drops V_d and diffuse layer surface charge density σ_d values using a cubic spline method to obtain a function that is a numerical approximation for the diffuse layer surface charge density $\sigma_d(V_d)$.

5. Impose the charge neutrality condition $\sigma_d(V_d) + \sigma_g(V_g) = 0$, where σ_g is given by Equation (4.22), and solve for the diffuse layer potential $V_d(V_a)$ and the graphene potential $V_g(V_a)$, using the total potential $V_a = V_d + V_s + V_g$, where $V_s = \sigma_d(V_d)/C_s$ is the Stern layer potential.
6. Find the quantum capacitance of graphene $C_q(V_g) = -\frac{dV_g}{d\sigma_g}$ and the diffuse layer capacitance $C_d(V_d) = -\frac{dV_d}{d\sigma_d}$, using their capacitance definitions.

4.3 Ionic Liquid Capacitances

In this section, a structure consisting of either a metallic or graphene electrode, and a diffuse layer in the ionic liquid which may contain a Stern layer is considered. The total capacitance of the system is computed using the algorithm discussed above. The two main parameters in the computations are the ion packing fraction γ and the normalized correlation length δ_c. Because the finite ion size is fixed to $a = 1$ Å, changes in ion concentration, c_∞, correspond to changes in $\gamma = 2a^3 c_\infty$, and hence, the value of γ will be varied in the computation. In addition to adopting two values typical for ionic liquids, $\gamma = 0.1$ and $\gamma = 0.5$, $\gamma = 0.0001$ is also considered in view of the current debate on whether ionic liquids could be envisioned as "dilute electrolytes" [57, 58]. The value of γ here refers to the fraction of "participation ions", whereas the fraction of the "non-participation ions" remains large in the bulk [57]. The "non-participation ions" belong to neutral ion pair aggregates and do not contribute to ion crowding, but their presence takes up a significant fraction of cells in the lattice-gas model. As a consequence, the definition of the Debye length would need to be modified to take into account the dependence of an effective dielectric permittivity on the fraction of ion pairs, which can be readily performed as the Debye capacitance $C_D \propto \sqrt{\epsilon}$ and the Debye screening length $\lambda_D \propto \sqrt{\epsilon}$. In this work, a fixed value $\epsilon = 10$ is used in all cases, and hence, the results shown for $\gamma = 0.0001$ should only be considered as qualitative.

In order to illustrate the effects of ion correlations, $\delta_c = 10$ is chosen as a representative value for ionic liquid, and is compared to the case of $\delta_c = 0$ (no ion correlations). Furthermore, the ionic liquid is assumed to be monovalent ($z = 1$) and its (relative) dielectric permittivity is given the value $\epsilon = 10$. In the cases where Stern layer is included in computations, $\epsilon_s = \epsilon = 10$ and its thickness is set to $h = a/2 = 0.5$ nm [66] (as per the discussion in Chapter 3 on the Stern layer).

At room temperature ($k_B T = 0.025$ eV), the Debye capacitance in ionic liquids studied here may be written as $C_D = C_D^* \sqrt{\gamma}$ with $C_D^* = \sqrt{e^2 \beta \epsilon / (4\pi a^3)} \approx 75.3$ μF cm^{-2}, whereas the Debye length becomes $\lambda_D = \lambda_D^*/\sqrt{\gamma}$ with $\lambda_D^* = \sqrt{\epsilon a^3/\left(4\pi\beta e^2\right)} \approx 0.12$ nm (giving $\lambda_D \approx 0.12/\sqrt{\gamma}$ nm). Likewise, the ratio R that relates the graphene and the ionic liquid subsystems takes the form $R = \frac{4\alpha_{\text{fine}}^2}{\sqrt{\pi\epsilon}}\left(\frac{a}{e^2\beta}\right)^{3/2} \approx 0.0078/\sqrt{\gamma}$.

4.3.1 Metallic Electrode

For a metallic electrode in contact with the ionic liquid, Equation (4.5) is solved numerically for the potential $\overline{\phi}(\overline{x})$ in the diffuse layer, subject to boundary conditions with several values of the potential at the interface with the electrode, $\overline{\phi}_0 = 1, 5, 10, 20$, for $\delta_c = 0$ and $\delta_c = 10$. In Figure 4.2, curves are shown for the normalized charge density in the diffuse layer $\overline{\rho}(\overline{\phi}(\overline{x}))$, for several different γ values. The results shown in Figure 4.2 (c) are consistent with those found in Figure 2 (a) in the paper by Bazant *et al.* [49]. For the cases of $\gamma = 0.1$ and $\gamma = 0.5$, in Figures 4.2 (b) and (c) the effects of both overscreening and crowding in the curves with $\delta_c = 10$ are shown, whereas the curves with $\delta_c = 0$ only exhibit the ion crowding effect due to steric effects [48, 65, 148]. It is interesting that the curves for $\gamma = 0.0001$ with $\delta_c = 10$ also show overscreening for larger $\overline{\phi}_0$ values. These overscreening effects are rather long ranged, given that the Debye length in Figure 4.2 (a) is $\lambda_D \approx 11.7$ nm, which is typical for an ordinary dilute electrolyte with ion concentration in the millimole range.

In Figure 4.3, the normalized total surface charge density in the diffuse layer is plotted, $\overline{\sigma}_d$, as a function of the normalized interface potential $\overline{\phi}_0$. Increases in γ and δ_c values give rise to a significant reduction of the charge accumulated in the diffuse layer, especially when compared to the case of the smallest ion fraction, $\gamma = 0.0001$, without ion correlation, $\delta_c = 0$, i.e. the case of a dilute electrolyte in the ordinary Poisson-Boltzmann limit. In Figure 4.3, the effects of increasing γ and δ_c are shown to be comparable. For example, the curve corresponding to $\gamma = 0.5$ with $\delta_c = 0$ gives comparable charge densities for $|\overline{\phi}_0| \approx 30$ as the curve corresponding to $\gamma = 0.1$ with $\delta_c = 10$.

In Figures 4.4 (a) and (b), the normalized diffuse layer capacitance, $\overline{C}_d$, is plotted as a function of the normalized potential drop through that layer, defined as $\overline{V}_d = -\overline{\phi}_0$, for the same set of parameters γ and δ_c as in Figure 4.3. Note that the same curves are shown in panels (a) and (b) of Figure 4.4, but with different scales on the vertical axes. In Figure 4.4 (a), the curves for both $\gamma = 0.0001$ and $\gamma = 0.1$ describe camel-shaped capacitance, while the curves for $\gamma = 0.5$ describe bell-shaped capacitance, for both $\delta_c = 0$ and $\delta_c = 10$. This shape independence of δ_c indicates that conditions for the transition from a camel- to bell-shaped diffuse layer capacitance may be independent of the ion correlation effects. This notion has been verified numerically and confirmed that the transition indeed occurs

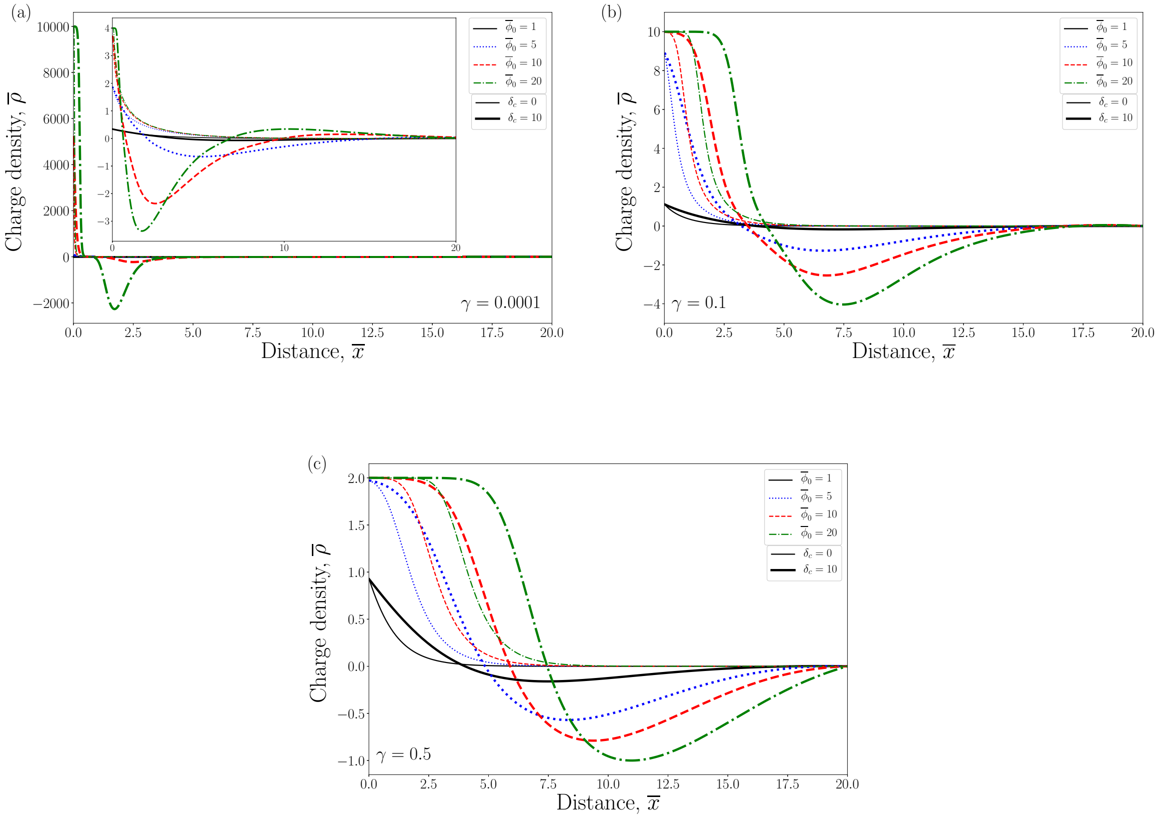

Figure 4.2: The normalized charge density, $\overline{\rho} = \frac{\rho}{2ec_\infty}$, versus the normalized distance, $\overline{x} = \frac{x}{\lambda_D}$, for varying ion packing fraction γ, for the ion correlation length (normalized to the Debye length) $\delta_c = 0$ (thin lines) and $\delta_c = 10$ (thick lines) and for several values of the normalized interface potential $\overline{\phi}_0$: $\overline{\phi}_0 = 1$ (black solid lines), $\overline{\phi}_0 = 5$ (blue dotted lines), $\overline{\phi}_0 = 10$ (red dashed lines) and $\overline{\phi}_0 = 20$ (green dot-dash lines). Panel (a) shows the results for $\gamma = 0.0001$, with the inset showing $\log(1 + |\overline{\rho}|)\,\mathrm{sign}(\overline{\rho})$ versus $\overline{x}$. Panels (b) and (c) show $\gamma = 0.1$ and $\gamma = 0.5$ respectively.

for $\gamma = 1/3$ irrespective of the value used for δ_c, thus corroborating similar observations [65, 69].

The reduced range of the $\overline{C}_d$ values in Figure 4.4 (b) emphasizes that, for the case $\gamma = 0.0001$, $\overline{C}_d(\overline{V}_d)$ exhibits a U-shaped dependence, typical of an ordinary electrolyte.

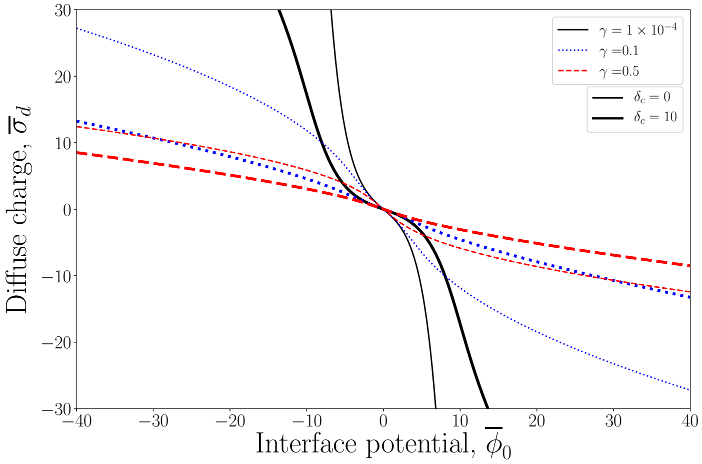

Figure 4.3: The normalized surface charge density in the diffuse layer, $\overline{\sigma}_d = \frac{\sigma_d}{en_c}$, for a metallic electrode versus the normalized potential at the interface, $\overline{\phi}_0$, for the ion packing fraction values of $\gamma = 0.0001$ (dilute electrolyte limit; black solid lines), $\gamma = 0.1$ (blue dotted lines), and $\gamma = 0.5$ (red dashed lines), and for the normalized ion correlation length $\delta_c = 0$ (thin lines) and $\delta_c = 10$ (thick lines).

Also, an overall reduction of $\overline{C}_d$ is observed in the presence of ion correlation effects with $\delta_c = 10$ compared to the case with $\delta_c = 0$. This is a major improvement over the mean-field theory of ionic liquids where only steric effects are taken into account [56, 66]. In particular, a reduction factor of $\sqrt{21}/11 \approx 0.42$ (comes from Equation (4.17)) in $\overline{C}_d$ can be seen at the potential $\overline{V}_d = 0$, which is independent of the γ values, as expected [49]. Moreover, in Figure 4.4 (b), for large $|\overline{V}_d|$ values, an inverse square root dependence of $\overline{C}_d$ on the potential emerges in a manner that becomes increasingly independent of δ_c for large γ. This seems to corroborate the observation by Goodwin *et al.* [69] of a universal dependence of the capacitance on the potential in the diffuse layer that is independent of the ion correlation effects in ionic liquids for sufficiently large $|\overline{V}_d|$ values. In Figure 4.4 (c), the same set of results for C_d are shown as in Figure 4.4 (b) as functions of arcsinh $\left(\overline{V}_d\right)$, which provides higher magnification to emphasize the behaviour close to the neutrality point.

In panel (d) of Figure 4.4, the effects of including the Stern layer are shown, where the normalized capacitance of $\overline{C}_s \approx 0.235/\sqrt{\gamma}$ is chosen as the relevant fixed parameters.

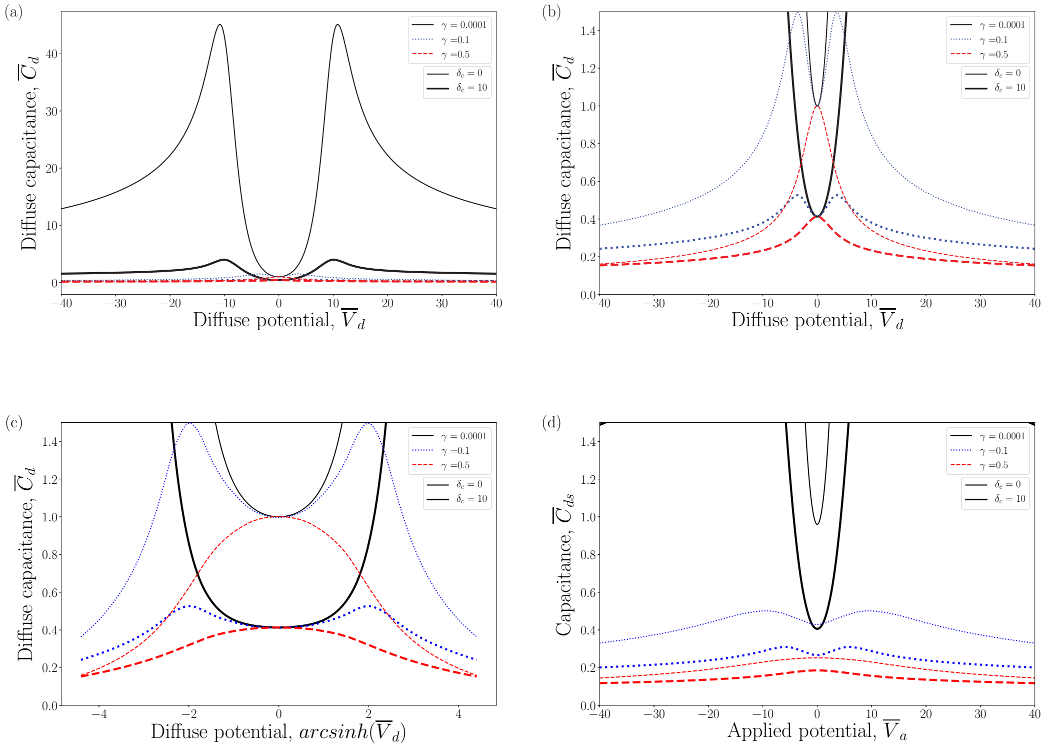

Figure 4.4: Panels (a), (b) and (c): The normalized capacitance of the diffuse layer, $\overline{C}_d = \frac{C_d}{C_D}$, for a metallic electrode versus the normalized diffuse potential, $\overline{V}_d = -\overline{\phi}_0$, for the ion packing fraction values of $\gamma = 0.0001$ (black solid lines), $\gamma = 0.1$ (blue dotted lines), and $\gamma = 0.5$ (red dashed lines), and for the normalized ion correlation length $\delta_c = 0$ (thin lines) and $\delta_c = 10$ (thick lines). Panel (a) shows the full range of $\overline{C}_d$, panel (b) shows a reduced capacitance range to showcase the structure of the capacitance near the neutrality point, while the panel (c) shows the curves from panel (b) as functions of arcsinh $\left(\overline{V}_d\right)$. Panel (d): The total capacitance of the diffuse layer and the included Stern layer, $\overline{C}_{ds} = \frac{\overline{C}_d \overline{C}_s}{\overline{C}_d + \overline{C}_s}$, for a metallic electrode, versus the normalized applied potential, $\overline{V}_a$, for the ion packing fraction values of $\gamma = 0.0001$ (black solid lines), $\gamma = 0.1$ (blue dotted lines), and $\gamma = 0.5$ (red dashed lines), and for the normalized ion correlation length $\delta_c = 0$ (thin lines) and $\delta_c = 10$ (thick lines).

The total capacitance of the ionic liquid, $\overline{C}_{ds} = \frac{\overline{C}_d \overline{C}_s}{\overline{C}_d + \overline{C}_s}$, is plotted as a function of the total applied potential, $\overline{V}_a = \overline{V}_d + \overline{V}_s$, for the same set of parameters and the same ranges as in Figure 4.4 (b). No noticeable effect of the Stern layer is observed for $\gamma = 0.0001$, as expected due to the relatively large $\overline{C}_s$ in this case. Going from Figure 4.4 (b) to Figure 4.4 (d), the Stern layer is able to decrease the magnitude of the capacitance and broaden the peaks in the curves for $\gamma = 0.1$ and $\gamma = 0.5$. It was pointed out by Fedorov and Kornyshev [66] that results for the diffuse layer capacitance based on a model, which only takes into account steric effects in an ionic liquid, can be brought to a closer agreement with the results of their computer simulations by inclusion of a Stern layer. Accordingly, the inclusion of Stern layer could also mimic the effects of ion correlation on the magnitude of the diffuse layer capacitance for $\gamma = 0.1$ and $\gamma = 0.5$. This is confirmed by the magnitude of $\overline{C}_{ds}$ near the neutrality point for $\gamma = 0.1$ with $\delta_c = 0$ in Figure 4.4 (d) being close to the magnitude of $\overline{C}_d$ near the neutrality point for $\gamma = 0.1$ with $\delta_c = 10$ in Figure 4.4 (b). In addition, the corresponding peak structure for the capacitance dependence on the potential appears to be generally broader in $\overline{C}_{ds}(\overline{V}_a)$ than in $\overline{C}_d(\overline{V}_d)$ owing to the fact that only one part of the applied potential $\overline{V}_a$ goes into charging the diffuse layer with $\overline{V}_d$, whereas the remaining part $\overline{V}_s = \overline{\sigma}_d(\overline{V}_d)/\overline{C}_s$ constitutes the potential drop across the Stern layer.

Although the choice of parameters in this computation is not aimed at reproducing experimental data on the capacitance of ionic liquids, a few comments are in order regarding the relevance of the capacitance values shown in the panels (b) and (d) of Figure 4.4. Lockett *et al* [44] and Islam *et al.* [144] observed both the camel– and bell–shaped capacitances near the measured neutrality point over a broad range from ~ 10 to ~ 20 μF cm^{-2}, whereas Jitvisate *et al* [46] measured neutrality point values at $6 - 7$ μF cm^{-2}. On the other hand, the curves for $\delta_c = 10$ in Figure 4.4 (b) give the neutrality point values for the capacitance without a Stern layer as $C_d \approx 10$ and $C_d \approx 22$ μF cm^{-2} for $\gamma = 0.1$ and $\gamma = 0.5$, respectively, whereas the corresponding values with $\delta_c = 10$ including a Stern layer are found in Figure 4.4 (d) to be $C_{ds} \approx 6.3$ and $C_{ds} \approx 9.7$ μF cm^{-2} for $\gamma = 0.1$ and $\gamma = 0.5$, respectively. All these values of the capacitance at the neutrality point are in semi-quantitative agreement with experiments [44, 46, 144].

4.3.2 Graphene Electrode

Now, consider a graphene electrode in place of the metallic electrode. In Figure 4.5, the fraction of the total applied potential $\overline{V}_a$ that is diverted to the diffuse layer $\overline{V}_d$ is shown for the same combinations of the γ and δ_c values as in the case of ideal metallic electrode studied in the preceding section. The cases without ($\overline{V}_a = \overline{V}_d + \overline{V}_g$) and with Stern layer

($\overline{V}_a = \overline{V}_d + \overline{V}_s + \overline{V}_g$) are depicted in the panels (a) and (b) of Figure 4.5, respectively. In general, $\overline{V}_d$ constitutes only a smaller fraction of $\overline{V}_a$; most of the applied potential goes to $\overline{V}_g$, which is responsible for charging the graphene electrode. This is also true in the presence of the Stern layer, which mostly acts to further reduce the potential drop $\overline{V}_d$ in the diffuse layer, as seen in Figure 4.5 (b). Specifically, in Figure 4.5, $|\overline{V}_d|$ is reduced by increasing γ and by lowering δ_c. Large differences between the curves for $\delta_c = 0$ and $\delta_c = 10$ are observed in the case of a dilute electrolyte, $\gamma = 0.0001$, for potentials $|\overline{V}_a| \gtrsim 10$. Furthermore, the curves for $\gamma = 0.1$ and $\gamma = 0.5$ are relatively narrowly distributed for all potentials, which is especially true when $\delta_c = 0$, but not so much when $\delta_c = 10$. Thus, it appears that the redistribution of the potential at the interface of graphene and ionic liquids with different γ values is increased by the presence of ion correlation effects.

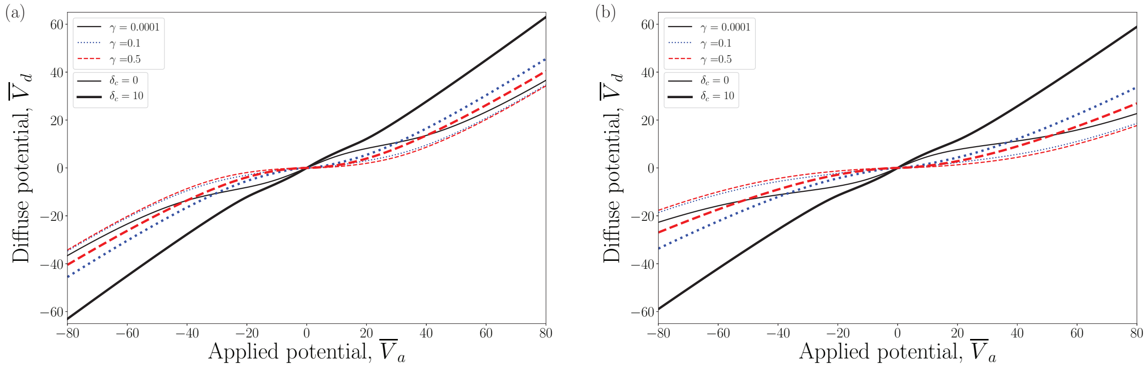

Figure 4.5: The normalized diffuse potential $\overline{V}_d$ of a graphene electrode versus the normalized applied potential $\overline{V}_a$ for the ion packing fraction values of $\gamma = 0.0001$ (black solid lines), $\gamma = 0.1$ (blue dotted lines), and $\gamma = 0.5$ (red dashed lines), and for the normalized ion correlation length $\delta_c = 0$ (thin lines) and $\delta_c = 10$ (thick lines). Panel (a) shows the results without a Stern layer and panel (b) shows the results when a Stern layer is added.

In Figure 4.6, the total capacitance, $\overline{C}_{dg} = \frac{\overline{C}_d \overline{C}_q}{\overline{C}_d + \overline{C}_q}$, of the graphene-ionic liquid interface (without Stern layer) is shown as function of the total applied potential, $\overline{V}_a = \overline{V}_d + \overline{V}_g$, along with the components of that capacitance, $\overline{C}_d\left(\overline{V}_d(\overline{V}_a)\right)$ and $\overline{C}_q\left(\overline{V}_g(\overline{V}_a)\right)$. The cases for $\gamma = 0.0001$ are shown in Figure 4.6 (a), where, near the neutrality point, $\overline{C}_d$ is comparable with $\overline{C}_q$ when $\delta_c = 0$, but is smaller than $\overline{C}_q$ when $\delta_c = 10$, owing to the reduction factor ~ 0.42 due to ion correlation, discussed in Figure 4.4. As a result, the curves for $\overline{C}_{dg}$ in Figure 4.6 (a) with $\delta_c = 0$ and $\delta_c = 10$ are relatively close to each other for the potential values $|\overline{V}_a| \lesssim 10$. At the same time, these same two curves exhibit large differences at the potential values $|\overline{V}_a| \gtrsim 10$ in Figure 4.6 (a), echoing the conclusion from Figure 4.5 regarding the role of the ion correlation effects in a dilute electrolyte for large potential values.

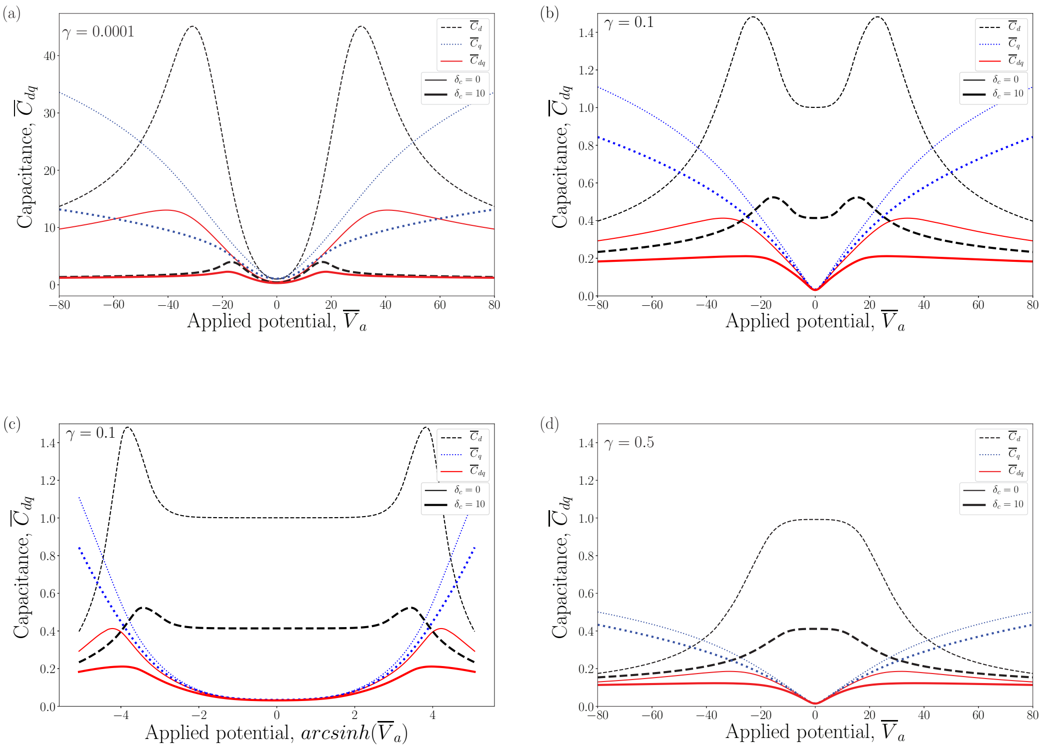

Figure 4.6: The normalized capacitance in the diffuse layer, $\overline{C}_d$ (black lines), the normalized quantum capacitance of the graphene electrode, $\overline{C}_q$ (blue lines), and the normalized total capacitance, $\overline{C}_{dg} = \frac{\overline{C}_d \overline{C}_q}{\overline{C}_d + \overline{C}_q}$ (red lines), for a graphene electrode versus the applied voltage $\overline{V}_a$, and for the normalized ion correlation length $\delta_c = 0$ (thin lines) and $\delta_c = 10$ (thick lines). Panel (a) shows the results for $\gamma = 0.0001$ on an extended capacitance range, panels (b) and (c) show the results for $\gamma = 0.1$ as functions of $\overline{V}_a$ and $\operatorname{arcsinh}\left(\overline{V}_a\right)$, respectively, while panel (d) shows the results for $\gamma = 0.5$ as as functions of $\overline{V}_a$.

In the panels (b) and (d) of Figure 4.6 the cases with $\gamma = 0.1$ and $\gamma = 0.5$, where the diffuse layer capacitance exhibits camel-shaped and bell-shaped dependencies on the potential, respectively, regardless of the δ_c values are shown. As a consequence of the smallness of the quantum capacitance of graphene $\overline{C}_q$ near the neutrality point, the total capacitance $\overline{C}_{dg}$ exhibits camel-like dependence on $\overline{V}_a$ for both $\gamma = 0.1$ and $\gamma = 0.5$. This is considered to be one of the most important manifestations of the quantum capacitance of graphene at the interface with ionic liquids. While the shape of $\overline{C}_{dg}(\overline{V}_a)$ closely follows the shape of $\overline{C}_q\left(\overline{V}_g(\overline{V}_a)\right)$ for $|\overline{V}_a| \lesssim 10$, in Figures 4.6 (b) and (d) it is shown that the ion correlation effects begin to cause some qualitative and quantitative differences in the shapes of the $\overline{C}_{dg}(\overline{V}_a)$ curves. As a result of the significant lowering of the $\overline{C}_d$ values for $\delta_c = 10$ in comparison with those for $\delta_c = 0$, the peaks in the $\overline{C}_{dg}(\overline{V}_a)$ curves with $\delta_c = 10$ are much broader than the peaks in the corresponding $\overline{C}_{dg}(\overline{V}_a)$ curves with $\delta_c = 0$. In fact, the $\overline{C}_{dg}(\overline{V}_a)$ curves with $\delta_c = 10$ appear to be almost flat for the potential values $|\overline{V}_a| \gtrsim 20$ in Figures 4.6 (b) and (d). Note that the widths of the local minima in the camel-shaped C_d curves in Figure 4.6 (b) and the local maxima in the bell-shaped C_d curves in Figure 4.6 (d) are larger than the widths in their counterparts in Figures 4.4 (b) and (d), respectively. Referring to Figure 4.5 (a), this can be explained by the fact that only a fraction of the applied potential $\overline{V}_a$ goes to the diffuse layer potential $\overline{V}_d$. In order to further elucidate the behaviour of the capacitances in Figure 4.6 (b) close to the neutrality point, the curves are shown as functions of $\operatorname{arcsinh}\left(\overline{V}_a\right)$ in Figure 4.6 (c).

The peaks in Figures 4.6 (b) and (d) occur when the potential and the capacitance take the following values: $|\overline{V}_a| \approx 33.9$ and $\overline{C}_{dg} \approx 0.41$ for $\gamma = 0.1$ and $|\overline{V}_a| \approx 31.6$ and $\overline{C}_{dg} \approx 0.19$ for $\gamma = 0.5$. These values may be reasonably well reproduced by using the expressions quoted in the preceding section for the quantum capacitance $C_q^\infty(V_g)$ and the diffuse layer capacitance $C_d^\infty(V_d)$ which are valid in the regime of large potentials, where those capacitances exhibit universal temperature-independence. The values of the potential drop in the diffuse layer, which correspond to the peaks in the $\overline{C}_{dg}(\overline{V}_a)$ curves with $\delta_c = 0$ in Figures 4.6 (b) and (d), are found from Figure 4.5 (a) to be: $|\overline{V}_d| \approx 7.0$ and $|\overline{V}_d| \approx 5.1$, respectively. Those values satisfy the condition $|\overline{V}_d| \gg 1$ only marginally, so an improved asymptotic form for the diffuse layer capacitance is used, i.e.,

$$C_d^\infty = \sqrt{\epsilon z e/\left[8\pi v\left(|V_d| - V_\gamma\right)\right]},\ \text{as} |V_d| \to \infty \tag{4.25}$$

which is valid for $|\overline{V}_d| > V_\gamma$, where $V_\gamma = \frac{k_B T}{e} \ln\left(\frac{2}{\gamma}\right)$ [40]. With this definition of V_γ, the model for C_d^∞ is no longer temperature- and concentration-independent, but it helps bring the estimates for the peaks in $\overline{C}_{dg}(\overline{V}_a)$ closer to those observed in Figures 4.6 (b) and (d) for $\delta_c = 0$. Referring to Equations (4.21) and (4.20) for $\overline{V}_a^*$ and $\overline{C}_{dg}^*$, their (normalized) values, $|\overline{V}_a^*| \approx 31.5$ and $\overline{C}_{dg}^* \approx 0.42$ for $\gamma = 0.1$ and $|\overline{V}_a^*| \approx 29.9$ and $\overline{C}_{dg}^* \approx 0.19$ for

$\gamma = 0.5$, indeed closely reproduce the peaks in $\overline{C}_{dg}(\overline{V}_a)$ observed in Figures 4.6 (c) and (d) for $\delta_c = 0$.

In Figure 4.7, the results for the inclusion of a Stern layer between the graphene electrode and the diffuse layer in the ionic liquid are shown, with a comparison of the resulting total capacitance $\overline{C}_{dsg}$ and the capacitance $\overline{C}_{dg}$ without the Stern layer, discussed in Figure 4.6. Note that, in Figure 4.7, $\overline{C}_{dsg}$ is shown as a function of the applied potential $\overline{V}_a = \overline{V}_d + \overline{V}_s + \overline{V}_g$, whereas $\overline{C}_{dg}$ is shown as a function of the applied potential $\overline{V}_a = \overline{V}_d + \overline{V}_g$. With the range of values adopted for the capacitances on the vertical axis in Figure 4.7, the case of $\gamma = 0.0001$ can only be observed for $\delta_c = 10$, showing negligible effects of the Stern layer, as expected for a dilute electrolyte. Furthermore, the cases of $\gamma = 0.1$ and $\gamma = 0.5$ show that both $\overline{C}_{dsg}(\overline{V}_a)$ and $\overline{C}_{dg}(\overline{V}_a)$ are dominated near the neutrality point by a local minimum in the quantum capacitance of graphene for both $\delta_c = 0$ and $\delta_c = 10$. However, the interval of the potential values $\overline{V}_a$ near the neutrality point where this minimum dominates is somewhat narrower in $\overline{C}_{dsg}(\overline{V}_a)$ than in $\overline{C}_{dg}(\overline{V}_a)$.

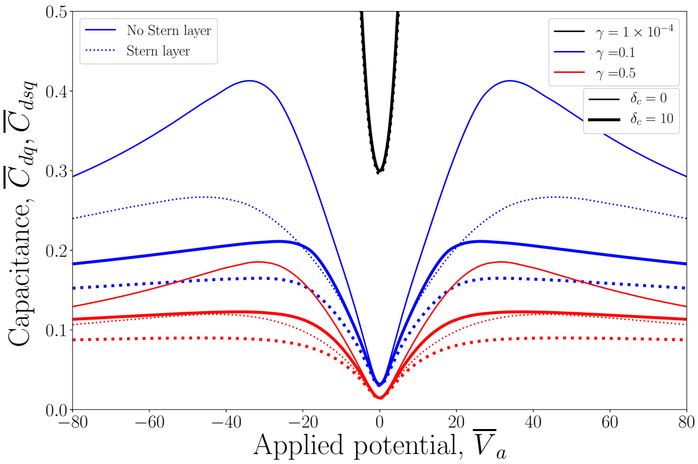

Figure 4.7: The normalized total capacitance without a Stern layer, $\overline{C}_{dg}$ (solid lines), and the normalized total capacitance with the inclusion of a Stern layer, $\overline{C}_{dsg}$ (dotted lines), for a graphene electrode versus the normalized applied potential, $\overline{V}_a$, for the ion packing fraction values of $\gamma = 0.0001$ (black lines), $\gamma = 0.1$ (blue lines), and $\gamma = 0.5$ (red lines), and for the normalized ion correlation length $\delta_c = 0$ (thin lines) and $\delta_c = 10$ (thick lines). Results are shown for a Stern layer thickness $h = 0.5$ nm and permittivity $\epsilon_s = 10$, and for a diffuse layer consisting of a permittivity of $\epsilon = 10$ and the lattice size of $a = 1$ nm.

For larger applied potentials, e.g. $|\overline{V}_a| \gtrsim 10$, all curves with $\gamma = 0.1$ and $\gamma = 0.5$ exhibit more or less broad peaks, giving rise to camel-shaped dependence of both $\overline{C}_{dsg}$ and $\overline{C}_{dg}$ on $\overline{V}_a$. As expected from Figures 4.6 (c) and (d), the inclusion of ion correlation effects with $\delta_c = 10$ reduces the magnitude of $\overline{C}_{dg}(\overline{V}_a)$ and broadens/flattens its peaks, when compared to the case with $\delta_c = 0$. As expected from Figure 4.4 (c), the inclusion of a Stern layer also reduces the magnitude of $\overline{C}_{ds}(\overline{V}_a)$ for $\gamma = 0.1$ and $\gamma = 0.5$ and also broadens/flattens its peaks, when compared to $\overline{C}_d(\overline{V}_d)$ in Figure 4.4 (b). When both the ion correlation and the Stern layer effects are included, the $\overline{C}_{dsg}(\overline{V}_a)$ curves for $\gamma = 0.1$ and $\gamma = 0.5$ with $\delta_c = 10$ in Figure 4.7 appear to almost level off at constant values for sufficiently large potentials, say, $|\overline{V}_a| \gtrsim 30$. These values are on the order of (using physical units) $C_{dsg} = 4.7$ μF cm^{-2}, occurring in a broad range of the applied potentials near $|V_a| = 1$ V for both $\gamma = 0.1$ and $\gamma = 0.5$, while the minima in the $\overline{C}_{dsg}(\overline{V}_a)$ curves that occur at the neutrality point are $C_{dsg} \approx 0.8$ μF cm^{-2} for both $\gamma = 0.1$ and $\gamma = 0.5$, coinciding with the minimum in the quantum capacitance of graphene.

4.4 Asymmetric Ionic Liquids

In the case of an asymmetric ionic liquid, the volumes occupied by positive and negative ions are not equal ($a_+ \neq a_-$), and hence, the entropic term of the free energy (Equation (4.4)) is modified to take into account the unequal packing of ions [68, 72, 150, 151]. Following the work of Gupta *et al.*, only the entropic term in Equation (4.5) requires a modification due to the unequal packing of ions. The asymmetric concentration relations are derived in the same way as outlined in Chapter 3 via minimizing the free energy functional with respect to concentration. Han *et al.* derived a generalized form for the entropic term under the assumption that positive ions are larger than negative ions, i.e. $a_+ \geq a_-$, and obtained expressions for ion concentrations, which are quoted below using the form given by Gupta *et al.* [72]:

$$c_+ = c_\infty \frac{e^{-ze\beta\phi}}{g(\phi)}, \tag{4.26}$$

$$c_- = c_\infty \frac{e^{ze\beta\phi} f(\phi)}{g(\phi)}, \tag{4.27}$$

where

$$f(\phi) = \left(1 + \frac{z a_-^3 c_\infty \left(e^{ze\beta\phi} - 1\right)}{1 - z a_+^3 c_\infty}\right)^{\frac{a_+^3}{a_-^3} - 1}, \tag{4.28}$$

$$g(\phi) = f(\phi) + z a_+^3 c_\infty \left[e^{-ze\beta\phi} - f(\phi)\right] + z a_-^3 c_\infty f(\phi)(e^{ze\beta\phi} - 1). \tag{4.29}$$

When ion sizes are equal, $a_+ = a_- = a$, the symmetric case for ion concentrations, Equation (3.6), is recovered. It should also be noted that due to the unequal volumes of the ions, packing fractions of ionic species will be unequal due to the competition of ions, and therefore, two values of γ are required: γ_+ for positive ions and γ_- for negative ions. Here, the ion concentrations are replaced by Equations (4.26) and (4.27) in Equation (4.5), and the computation carried out as outlined in the previous sections. In the calculation, the values $\gamma_+ = 0.5$ for cations and $\gamma_- = 0.1$ for anions are assigned, while keeping all other parameters the same as in the preceding discussion. The results for the asymmetric ionic liquid are normalized by using the definitions for the Debye length, λ_D, and the Debye capacitance, C_D, with fixed ion fraction of $\gamma = \gamma_+ = 0.5$.

In Figure 4.8, the normalized charge density, $\overline{\rho}\left(\overline{\phi}(\overline{x})\right)$, is shown for both positive and negative values of the potential $\overline{\phi}_0$ at the interface of the diffuse layer in an ionic liquid and a metallic electrode. Owing to ion crowding effects close to the interface, for large positive $\overline{\phi}_0$ values in Figure 4.8 (a), the charge density saturates at the value $\overline{\rho} = -1/\gamma_- = -10$, whereas for large negative $\overline{\phi}_0$ values in Figure 4.8 (b), the density saturates at $\overline{\rho} = 1/\gamma_+ = 2$. In both panels, strong overscreening occurs at large $|\overline{\phi}_0|$ values. The curve for $\overline{\phi}_0 = 20$ in Figure 4.8 (a) exhibits a second layer that is occupied by cations, where the charge density is bounded above by $\overline{\rho} = 1/\gamma_+ = 2$. This shows that, for sufficiently large electrode potentials, there may be strong interplay of ion crowding and overscreening effects, which extends farther out into the ionic liquid, beyond the first ion layer, so that overcrowding may affect higher-order ion layers.

Similar to Figures 4.6 (b) and (d), Figure 4.9 shows the total capacitance, $\overline{C}_{dg} = \frac{\overline{C}_d \overline{C}_q}{\overline{C}_d + \overline{C}_q}$, of the interface of an asymmetric ionic liquid and a graphene electrode (without Stern layer) as function of the total applied potential, $\overline{V}_a = \overline{V}_d + \overline{V}_g$, along with the components of that capacitance, $\overline{C}_d\left(\overline{V}_d(\overline{V}_a)\right)$ and $\overline{C}_q\left(\overline{V}_g(\overline{V}_a)\right)$. Note that $\overline{C}_d$ exhibits asymmetric structure, which is similar in shape to the capacitances observed in recent experiments with pure ionic liquids and metal electrode [46]. Also the amplitude of $\overline{C}_d$ in Figure 4.9 is much higher than those reported by Jitvisate *et al.* [46], but it could possibly be brought down by increasing the ion correlation parameter δ_c or by inclusion of a Stern layer, as discussed in Figure 4.4 (d). Figure 4.9 focuses on the effects of a graphene electrode, which is again seen

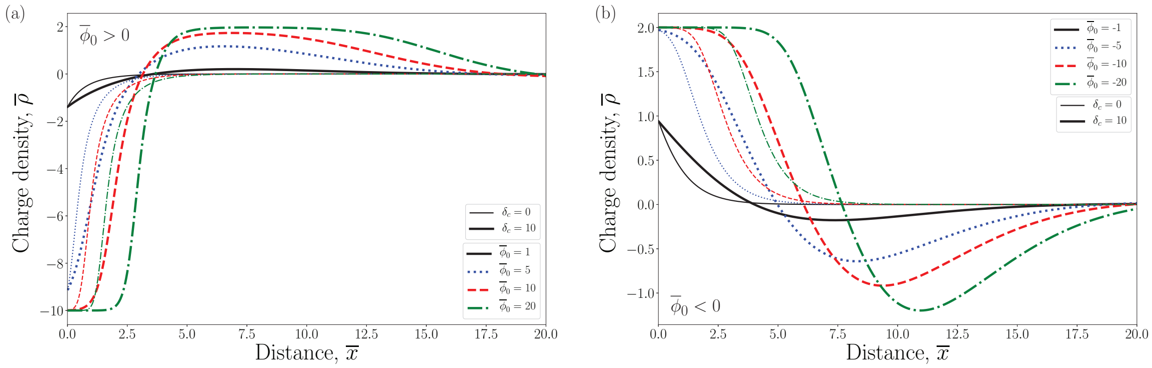

Figure 4.8: Panel (a): The normalized charge density $\overline{\rho}$ versus the normalized distance $\overline{x}$, for an asymmetric ionic liquid with ion packing fraction values of $\gamma_+ = 0.5$ and $\gamma_- = 0.1$, and for the normalized ion correlation length $\delta_c = 0$ (thin lines) and $\delta_c = 10$ (thick lines), and for several values of the normalized initial potential $\overline{\phi}_0$: $\overline{\phi}_0 = 1$ (black solid lines), $\overline{\phi}_0 = 5$ (blue dotted lines), $\overline{\phi}_0 = 10$ (red dashed lines) and $\overline{\phi}_0 = 20$ (green dot-dash lines). Panel (b): same as (a), but for $\overline{\phi}_0$: $\overline{\phi}_0 = -1$ (black solid lines), $\overline{\phi}_0 = -5$ (blue dotted lines), $\overline{\phi}_0 = -10$ (red dashed lines) and $\overline{\phi}_0 = -20$ (green dot-dash lines).

to dominate the capacitance over the range of applied potentials $|\overline{V}_a| \lesssim 10$, giving rise to a rather symmetric, V-shaped minimum in $\overline{C}_{dg}$ at the neutrality point. Outside this range of the applied potential, two somewhat broad peaks give rise to an overall asymmetric camel-shaped capacitance $\overline{C}_{dg}$, with a higher peak at negative $\overline{V}_a$ (and hence negative $\overline{V}_d$, corresponding to a positive $\overline{\phi}_0 = -\overline{V}_d$), reflecting the fact that the smaller sized anions are crowded to a larger extent near the positively charged graphene.

Near the neutrality point in Figure 4.9, $C_{dq} \approx 0.8$ μF cm^{-2}, as was the case in Figures 4.6 (b) and (d), and in Figure 4.7 in the presence of a Stern layer. This value corresponds to the minimum in the quantum capacitance of graphene at room temperature, which is expected since $C_q \ll C_d$ and hence $C_{dq} \approx C_q$ near the neutrality point. Experimental data from Oll *et al.* [152] also exhibits a V-shaped minimum in the capacitance of a graphene–ionic liquid interface, which takes the value ≈ 1.7 μF cm^{-2} at the Dirac point, consistent with the measurements on single-layer graphene by Uesugi *et al.* [138]. The almost doubled value of the experimental capacitance at the neutrality point compared to the theoretical value of ≈ 0.8 μF cm^{-2} may be explained by the effect of fluctuations in the potential values across a nominally neutral graphene surface [92], which result from a

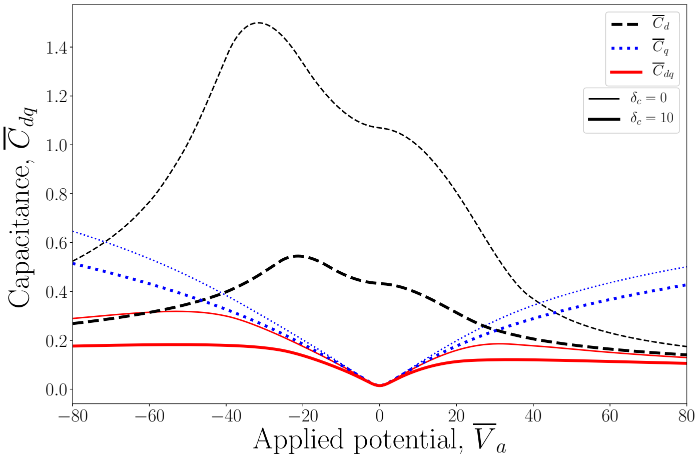

Figure 4.9: The normalized diffuse capacitance, $\overline{C}_d$ (blue dotted lines), the normalized quantum capacitance of the graphene electrode $\overline{C}_q$ (black dashed lines), and the total capacitance, $\overline{C}_{dg}$ (red solid lines), for a graphene electrode versus the normalized applied potential, $\overline{V}_a$, for an asymmetric ionic liquid with ion packing fraction values of $\gamma_+ = 0.5$ and $\gamma_- = 0.1$. Results for $\delta_c = 0$ are shown as thin lines while results for $\delta_c = 10$ are shown as thick lines.

random distribution of charged impurities in the insulating substrate underneath graphene [153]. Those fluctuations are quite capable of doubling the effective minimum value in the quantum capacitance of a graphene sheet lying on an oxide layer [92], and hence the experimental value can be larger in magnitude than the predicted theoretical value.

4.5 Concluding Remarks

The modified Poisson-Fermi equation (Equation (4.5)) was used to study the effects of ion correlations and finite ion sizes on the differential capacitance of the interface of a pure ionic liquid and a charged planar electrode [49]. Emphasis was put on the effects of the quantum capacitance of graphene in comparison to the standard metallic electrode. Effects of a Stern layer between the ionic liquid and the electrode as well as the effects of different ion sizes in the ionic liquid were explored. Two typical ion packing fractions in the ionic liquid were utilized, $\gamma = 0.1$ and $\gamma = 0.5$, which give rise to a camel-shaped and a bell-shaped diffuse layer capacitance, C_d, respectively.

In the presence of a metallic electrode, the inclusion of both the ion correlation effects and the Stern layer in the ionic liquid reduces the magnitude of its diffuse layer capacitance C_d, while the Stern layer further broadens any peak structures in the C_d dependence on the potential drop V_d in that layer. In the case of a dilute electrolyte, the Stern layer has little influence on the diffuse layer capacitance C_d, while the ion correlation effects persist, giving rise to long-ranged overscreening effects, accompanied by a reduction of the diffuse layer capacitance C_d.

In the case of a graphene electrode, the largest fraction of the total applied potential V_a goes to shifting the chemical potential in graphene, which controls its charge density via the potential of graphene V_g, whereas the potential drop in the diffuse layer remains bounded by $|V_d| \lesssim 1$ V. The quantum capacitance of graphene, C_q, is so small near the potential of zero charge that it dominates the total capacitance at the interface with the ionic liquid $C_{dq} = \frac{C_d C_q}{C_d + C_q}$ over a range of applied potential values, $|V_a| \lesssim 0.2 - 0.3$ V, giving rise to a camel-shaped function of the total capacitance $C_{dq}(V_a)$ for both $\gamma = 0.1$ and $\gamma = 0.5$. This is true regardless of the effects due to ion correlation or the Stern layer in symmetric ionic liquid as long as the ion packing fraction is not too small. When these two effects are included, the peaks in the total capacitance of the interface become very broad, with $C_{dq}(V_a)$ showing a tendency to level off for very large applied potentials, $|V_a| \gtrsim 1$ V.

At the interface of graphene with an asymmetric ionic liquid, having different packing fractions for cations and anions, an asymmetric camel-shaped total capacitance $C_{dq}(V_a)$, with a local minimum at the potential of zero charge governed by the minimum in the quantum capacitance of graphene is observed.

In the regime of a dilute electrolyte with very small ion packing fraction, the role of quantum capacitance in the total capacitance is not as prominent as for large packing fractions. However, it would be interesting to explore issues related to the long ranged screening in ionic liquids by means of surface force measurements when graphene is used as a charged electrode [57, 58].

Finally, it would be worthwhile to explore generalizing the modified Poisson-Fermi equation for asymmetric ionic liquids to include the effects of different ion correlation lengths for cations and anions [49, 68]. Additionally, the model developed by Goodwin *et al.* [69] showed strong promise for describing the experimental measurements of the capacitance in ionic liquids [46], so it would be interesting to generalize it by inclusion of a graphene electrode in a manner similar to the discussion provided here.

Chapter 5

Sensitivity to pH and Ion Concentration

Sensors are continually being developed for more applications and utility in electronic devices. They are widely used in automobiles, airplanes, telephones, radios, industrial plants, and, more recently, in biological sensors which can be implanted in the human body [154]. When integrating sensors, the miniaturization of these devices, cost, performance, and toxicity are important manufacturing factors. Due to its thinness, flexibility, and unique band structure, which gives rise to clear minima in its conductivity and capacitance, graphene has risen to be a key material in nanoscale biological and chemical sensors [1, 5, 6]. Because graphene is chemically inert, the addition of an oxide layer or non-covalent functional coating between graphene and the electrolytic environment helps to increase the adsorption, and consequently, the sensing capabilities of graphene-based devices [5, 21, 82]. This functionalization enables chemical bonding of ion species from the electrolyte on the oxide surface which changes the charge balance of the system, and ultimately, affects the conductivity and capacitance of graphene, resulting in a shift of the minimum from its neutral position. This shift in the minimum is then plotted as either the ion concentration/pH against the potential where the minimum occurs [19, 21, 27, 30, 31, 33, 76, 82]. The sensitivity of the devices is then determined via the slope of the line which connects the minima, and is reported as volts per molar concentration or volts per pH, depending on the configuration of the experiment. Of particular interest in the development and experimental testing of graphene-based biochemical sensors is methods for increasing their sensitivity to changes in environmental ion concentration and/or pH [19, 21, 27, 30, 31, 33, 76, 82]. Importantly, when a functionalized layer is included, these graphene-based devices can give rise to high sensitivities, allowing the sensor to be able to distinguish between minute changes in their environment. While many experimental studies on the sensitivity of graphene-based FETs have been reported, the modelling of such systems has lagged behind. It is imperative to theoretically understand the role of graphene in sensors so that advancements can be made in nano-scale sensing devices.

As discussed in the Introduction, the sensing function of graphene can be achieved by either measuring the electrical conductivity of graphene in an electrolytically gated FET configuration, or measuring the capacitance of a graphene interface with electrolyte. In the former case, a minimum conductivity is achieved at the point where graphene is nominally neutral, characterized by the Fermi energy level being pinned to the Dirac point in graphene. This causes a depletion of conducting charges in graphene and results in a pronounced minimum in its conductivity as a function of the applied potential. In the case of the capacitance measurements, it is the smallness of the quantum capacitance of graphene at the neutrality point that causes a pronounced minimum in the total capacitance of the interface as a function of the applied gate potential through the electrolyte. The minimum in the conductance or the minimum in the capacitance is sensitive to the charge balance in the structures near graphene. Thus, measurement of the applied potential near these minima (the so-called potential of zero charge) as a function of the ion concentration or the pH in the solution gives sensitivity curves, of great value for sensing applications of graphene. Therefore, in the regime at the potential of zero charge characterized by the vanishing surface charge density on graphene, or neutrality point, $\sigma_g = 0$, is of particular interest for modelling.

The inclusion of ion adsorption at the interface between the sensor and the bulk electrolytes in the modelling of this layered structure allows for a direct link with the experimental data reported. Here, direct comparisons between the reported conductivity/capacitance minima and the minima obtained from modelling are made with remarkable agreement, in both the case of sensitivity to ion concentration and pH. This experimental validation of the mathematical model provides direct insight into the physical systems at play in graphene-based sensors; in particular, the inclusion of a finite ion size in the diffuse layer and a functionalized oxide layer between graphene and the electrolyte yield potential minima which directly match those obtained from experiments.

5.1 Theory

In Chapters 3 and 4, only an electric double layer forms at the interface of the electrode and the electrolyte/ionic liquid. In this regime, the adsorption of ions onto the surface of the electrode was not considered (see Figure 1.5 on Page 8). This scenario gives a description of the electrostatic interactions between the electrolyte and bulk solution, but without any chemical interactions. Chemical reactions on the surface of the interface may give rise to a net charge. The adsorption of ionic species onto the electrode results in either ions being “removed” from the bulk solution as they are no longer mobile or ions being “added” to the bulk solution when they become desorbed from the surface. This adsorption/desorption of species, particularly H^+ is responsible for the observed changes in either pH or ion concentration in the bulk solution [28]. The inclusion of this adsorbed layer into the previously established models will be the focus this chapter.

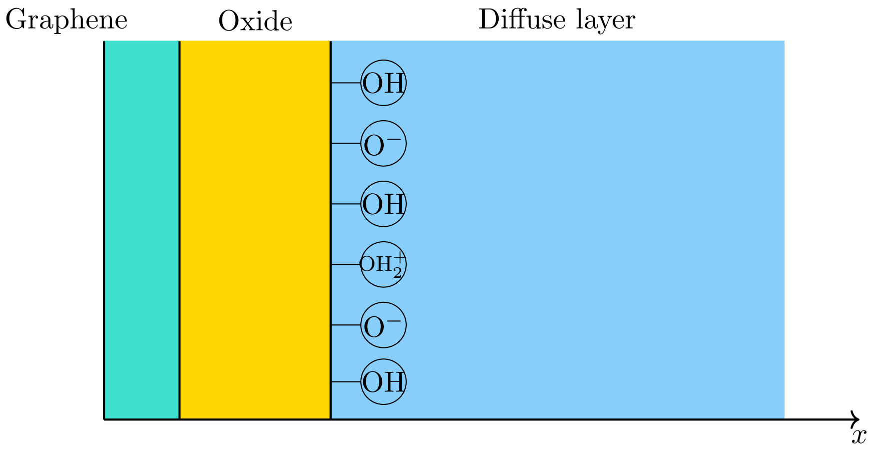

Figure 5.1: Schematic representation of the layered system, consisting of a graphene electrode, oxide layer, which promotes binding, and a diffuse layer. An adsorbed layer, consisting of protons and hydroxyl groups, forms at the oxide–diffuse layer interface.

Similar to the discussion in Chapters 3 and 4, a layered composed of a graphene sheet, an oxide layer, and the diffuse layer in the electrolyte is considered (Figure 5.1). In view of the current debate in the literature as to whether or not bare graphene is sensitive, graphene is functionalized by placing an oxide layer between graphene and the diffuse layer. The oxide surface is characterized by a high density of defect sites where ions from the electrolyte can absorb and desorb at certain rates. The inclusion of the oxide layer is mathematically similar to the inclusion of the Stern layer described in Chapter 3, with an important difference being the existence of an atomically thin layer of adsorbed ions at the oxide–electrolye interface, giving rise to an average equilibrium surface charge density σ_a.

The electrostatic forces described in Chapters 3 and 4 act over long ranges unlike chemical interactions which are short reange. Because hydrated salt ions are large in size, they do not adsorb onto the surface and so the protons and hydroxyl groups are the only binding groups considered. The bound groups form an adsorbed layer that exists within the diffuse layer and account for the net charge arising from chemical reactions at the oxide surface. The adsorbed ions are removed from the bulk diffuse layer, and hence, the adsorbed layer can be considered a subsystem of the diffuse layer as a whole. The adsorbed layer occurs at the inner Helmholtz plane (IHP) in the electric double layer (EDL), and hence, occurs within the Stern layer (Figure 1.5 on Page 8). In principle, a charge-free Stern layer between the adsorbed layer and the diffuse layer can be included (i.e. between the IHP and OHP in Figure 1.5 on Page 8) but, for the sake of simplicity, such refinement is disregarded in the present model. For the same reason, the dielectric permittivity of solvent (water) ϵ_w is assumed constant throughout the diffuse layer.

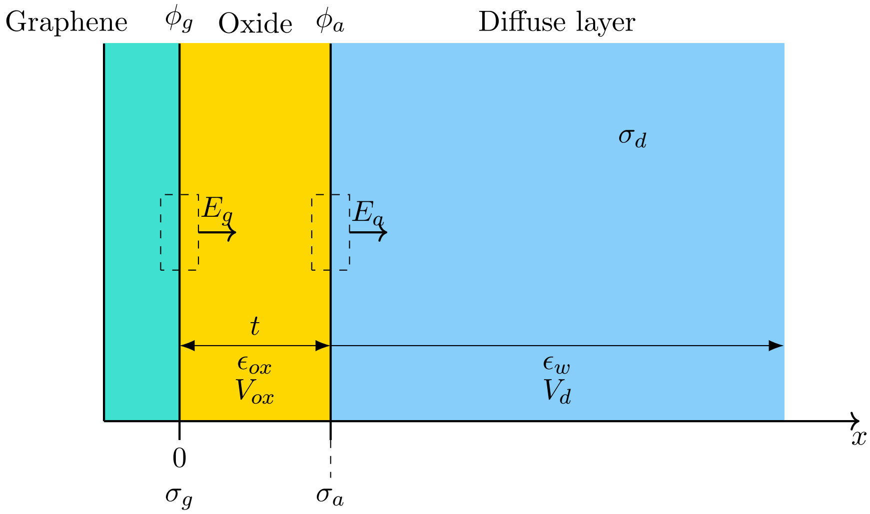

Figure 5.2: Schematic representation of the layered system with a graphene sheet with charge density σ_g and potential ϕ_g, a functionalized oxide layer with thickness t and dielectric permittivity of ϵ_{ox}, and the diffuse layer with dielectric permittivity ϵ_w and charge density σ_d, which includes an adsorbed layer with charge density σ_a. The Gaussian pillboxes are also shown at each layer with dashed lines.

A planar structure, consisting of a graphene electrode and oxide layer with large areas is considered, so that the electrostatics of the problem depend only on the x coordinate, with the outermost graphene surface located at $x = 0$. The system has the following boundary conditions, which come from analyzing the Gaussian pillboxes in Figure 5.2:

$$\epsilon_w E_a - \epsilon_{ox} E_g = 4\pi\sigma_a \tag{5.1}$$

$$\epsilon_{ox} E_g = 4\pi\sigma_g \tag{5.2}$$

$$-\epsilon_w E_a = 4\pi\sigma_d. \tag{5.3}$$

Here, ϵ_{ox} is the dielectric constant of the oxide (occupying the region $0 < x < t$), while σ_g and σ_d are the surface charge densities on graphene and in the diffuse layer, respectively. The (constant) electric field in the oxide is E_g, whereas E_a is the electric field in the diffuse layer evaluated at $x = t^+$, i.e., at the diffuse layer–oxide interface. Adding Equation (5.1) and Equation (5.2) gives $\epsilon_w E_a = 4\pi(\sigma_a + \sigma_g)$, and further combination with Equation (5.3) gives the charge neutrality condition for the system:

$$\sigma_a + \sigma_g + \sigma_d = 0. \tag{5.4}$$

As mentioned above, this condition is a key step in modelling the sensitivity of graphene near the neutrality point, where setting the surface charge density of graphene $\sigma_g = 0$ corresponds to a regime that yields a minimum in the conductivity or a minimum in the capacitance of electrolytically gated graphene. The potential drop inside the graphene sheet, which is responsible for charging the graphene, is $V_g = \varepsilon_F/e + \phi_g$, where ε_F is the Fermi energy. The potential across the oxide layer is $V_{ox} = \phi_a - \phi_g$ and $V_d = \phi_\infty - \phi_a = -\phi_a$ (as $\phi_\infty = 0$) across the diffuse layer. Then, the total potential drop across the system is $V_a = \varepsilon_F/e = V_g + V_{ox} + V_d$. Here, e is the elementary charge. Then, the surface charge density on graphene, σ_g, is given by (see Equation (2.15) on Page 18)

$$\sigma_g = eN_g \bigg(\mathrm{dilog}(1 + e^{-ze\beta V_g}) - \mathrm{dilog}(1 + e^{ze\beta V_g}) \bigg), \tag{5.5}$$

with $N_g = \frac{2}{\pi(\hbar v_F \beta)^2} \approx 9.2 \times 10^{-4}\mathrm{nm}^{-2}$. At the neutrality point, the potential $V_g = 0$ and hence the surface charge density $\sigma_g = 0$. On the other hand, the surface charge density of the diffuse layer is usually modeled in the literature [48] by using the simple Poisson-Boltzmann model, i.e.,

$$\sigma_d = 4\sigma_{gc} \sinh\left(\frac{ze\beta V_d}{2}\right), \tag{5.6}$$

where $\sigma_{gc} = e/(4\pi\lambda_D\lambda_B) \approx 0.36\sqrt{c}$ e/nm^2, with c being the numerical value of the bulk ion concentration, c_∞, expressed in the units of M=mole/litre, whereas $\lambda_D = \sqrt{\frac{\epsilon_w}{8\pi\beta z^2 e^2 c_\infty}}$ is the Debye length and $\lambda_B = \beta e^2/\epsilon_w$ is the Bjerrum length.

5.1.1 Inclusion of Steric Effects

One of the modifications made to the Poisson Boltzmann formulation in Chapters 3 and 4 was the addition of finite ion size effects in the diffuse layer. Likewise with the case of adsorption, the finite size of ions in the diffuse layer will also be considered. The surface charge density in the diffuse layer follows from [48]

$$\sigma_d = \text{sign}\left(V_d\right) 2zec_\infty \lambda_D \sqrt{\frac{2}{\nu} \ln\left(1 + 2\nu \sinh^2\left(\frac{ze\beta V_d}{2}\right)\right)}. \tag{5.7}$$

A recent study by Parizi *et al.* [155] demonstrated that the inclusion of finite ion size in the adsorbed layer provides better comparisons with experimental results. Their model only assumes that protons adsorb and desorb from the interface of the electrode, creating a layer of positive charge next to the electrode surface, which results in an accumulation of oppositely charged groups, e.g. salt ions or hydroxyl groups, next to the adsorbed layer. While their model dis able to reproduce the shape of experimental results, their simulations produce capacitance curves which are higher than those observed in experiments. In addition, the model by Parizi *et al.* [155] only includes one type of binding on the surface (protons), unlike the site model where both protons and hydroxyl groups are allowed to adsorb onto the surface. By allowing different types of groups to adsorb onto the surface, the charge density is likely to be more uniform in nature, as energetically it would be favoured for oppositely charged groups to bind next to each other rather than two groups of the same charge (as the like charges would have a repulsion between them). The inclusion of steric effects in the diffuse layer (Equation (5.7)) allows for the salt ions in the bulk electrolyte to have size, which accounts for any size effects of the opposite charge in the diffuse layer, and therefore, the effects of finite ion size in the adsorbed layer will be ignored.

5.1.2 Adsorbed Layer

To derive an expression for the charge density of the adsorbed ions, a site binding model will be used [34, 35]. This model utilizes the surface reactions to describe the adsorption/desorption of species. For now, only the case where H^+ is adsorbed/desorbed from the interface will be considered. The reactions at the surface are then (see Figure 1.7 on Page 11):

$$\mathrm{AOH_2^+} \rightleftharpoons \mathrm{AOH} + \mathrm{H^+} \tag{5.8}$$

$$\mathrm{AOH} \rightleftharpoons \mathrm{AO^-} + \mathrm{H^+}. \tag{5.9}$$

From here, the equilibrium dissociation constants, which gives the extent to which a compound will dissolve in a solvent, are defined:

$$K_{\mathrm{b}} = \frac{[\mathrm{AOH}][\mathrm{H}^+]_{\mathrm{surface}}}{[\mathrm{AOH}_2^+]} \tag{5.10}$$

$$K_{\mathrm{a}} = \frac{[\mathrm{AO}^-][\mathrm{H}^+]_{\mathrm{surface}}}{[\mathrm{AOH}]}. \tag{5.11}$$

Here, the square brackets denote the concentration of the species, A represents the atoms in the oxide, AOH, AO^-, and AOH^+ represent the surface complexes which are formed by adsorption, and $[\mathrm{H}^+]_{\mathrm{surface}}$ represents the surface concentration of protons, given in the units of M = moles/litre. A relation between the surface concentration of H^+ and the bulk concentration is given via the Boltzmann distribution [34, 35]:

$$[\mathrm{H}^+]_{\mathrm{surface}} = [\mathrm{H}^+]_{\mathrm{bulk}} e^{-\frac{e\phi_a}{k_B T}}. \tag{5.12}$$

Here, ϕ_a is the value of the electrostatic potential at the oxide surface where adsorption takes place relative to the potential in the bulk of the electrolyte, taken to be $\phi_\infty = 0$. Finally, the total number of binding sites on the oxide surface is fixed

$$N_s = [\mathrm{AOH}] + [\mathrm{AOH}_2^+] + [\mathrm{AO}^-]. \tag{5.13}$$

Then the surface charge on the adsorbed layer is given by:

$$\begin{align} \sigma_a &= e([\mathrm{AOH}_2^+] - [\mathrm{AO}^-]) \tag{5.14} \\ &= eN_s \frac{[\mathrm{AOH}_2^+] - [\mathrm{AO}^-]}{[\mathrm{AOH}] + [\mathrm{AOH}_2^+] + [\mathrm{AO}^-]}. \tag{5.15} \end{align}$$

Using Equations (5.10), (5.11), and (5.12) gives a final form of [34, 35]:

$$\sigma_a = eN_s \frac{2\delta \sinh\left(\beta e(\phi_N - \phi_a)\right)}{1 + 2\delta \cosh\left(\beta e(\phi_N - \phi_a)\right)}, \tag{5.16}$$

where $\delta = \sqrt{\frac{K_{\mathrm{a}}}{K_{\mathrm{b}}}}$ and ϕ_N is the Nernst potential, given by

$$\begin{align} \phi_N &= \frac{k_B T}{e} \ln\left(\frac{[\mathrm{H}^+]_{\mathrm{bulk}}}{\sqrt{K_{\mathrm{b}} K_{\mathrm{a}}}}\right) \tag{5.17} \\ &= \frac{1}{\beta e} \ln\left(\frac{10^{-pH}}{(10^{-pK_{\mathrm{b}}} 10^{-pK_{\mathrm{a}}})^{1/2}}\right) \tag{5.18} \\ &= \frac{1}{\beta e} \ln 10 \left[\frac{pK_{\mathrm{b}} + pK_{\mathrm{a}}}{2} - pH\right], \tag{5.19} \end{align}$$

with $pK_\mathrm{b} = -\log_{10} K_\mathrm{b}$ and $pK_\mathrm{a} = -\log_{10} K_\mathrm{a}$. Note the pH in the bulk of the electrolyte enters in the definition of the Nernst potential. Recall that pH is defined as $pH = -\log_{10}\left(\frac{\gamma_{\mathrm{H}^+}[\mathrm{H}]^+_\mathrm{bulk}}{c^0}\right)$, where γ_{H^+} is a dimensionless activity coefficient that takes into account deviations from ideal behaviour of the concentration, $[\mathrm{H}]^+_\mathrm{bulk}$ is the concentration of protons in the bulk solution, and c^0 is the standard concentration of 1 M. If the non-ideal terms are neglected, i.e. $\gamma_{\mathrm{H}^+} \to 1$, then the pH can be approximated as $pH \approx -\log_{10}\frac{[\mathrm{H}]^+_\mathrm{bulk}}{c^0} = -\log_{10}[\mathrm{H}]^+_\mathrm{bulk}$.

Total Capacitance

The total capacitance of the system is derived as was done in Chapter 3 on Page 51 and Chapter 4 on Page 74, to give:

$$\begin{aligned}
C^{-1} &= -\frac{dV_a}{d\sigma_g} && (5.20)\\
&= -\frac{dV_g}{d\sigma_g} - \frac{dV_{ox}}{d\sigma_g} - \frac{dV_d}{d\sigma_g} && (5.21)\\
&= C_g^{-1} + C_{ox}^{-1} - \frac{dV_d}{d\sigma_d}\frac{d\sigma_d}{d\sigma_g} && (5.22)\\
&= C_g^{-1} + C_{ox}^{-1} - C_d^{-1}\left(-1 - \frac{d\sigma_a}{dV_d}\frac{dV_d}{d\sigma_g}\right) && (5.23)\\
&= C_g^{-1} + C_{ox}^{-1} + C_d^{-1} + C_d^{-1}C_a\left(-C^{-1} + C_g^{-1} + C_{ox}^{-1}\right). && (5.24)
\end{aligned}$$

Rearranging, gives:

$$\begin{aligned}
C^{-1}(1 + C_d^{-1}C_a) &= (C_g^{-1} + C_{ox}^{-1})(1 + C_d^{-1}C_a) + C_d^{-1}, && (5.25)\\
\implies C^{-1} &= C_g^{-1} + C_{ox}^{-1} + (C_d + C_a)^{-1}. && (5.26)
\end{aligned}$$

Here, C_g is the quantum capacitance of graphene, $C_{ox} = \frac{\epsilon_{ox}}{4\pi t}$ is the capacitance of the functional oxide layer, C_d is the capacitance of the diffuse layer, and C_a is the capacitance of the adsorbed layer. To discard the oxide layer, let $t = 0$ so that $C_{ox} \to \infty$, and $C_{ox}^{-1} \to 0$, and, similarly, to consider a metallic electrode, let $C_g \to \infty$ so that $C_g^{-1} \to 0$.

Equation (5.26) indicates a parallel capacitor connection between the adsorbed layer and the diffuse layer, and then a series connection of the graphene layer, oxide layer, and parallel connection. If the adsorbed layer were to be discarded, $C_a^{-1} \to 0$, the series connection of layers from the previous chapters is recovered. Because the adsorbed layer can be considered a subsystem of the whole diffuse layer, where the total charge in the electrolyte is the combined surface charge density on the adsorbed layer σ_a and the surface charge density in the diffuse layer σ_d a parallel connection between the adsorbed layer and the diffuse layer is not unexpected (Figure 5.2). Equation (5.26) also indicates that if the oxide capacitance is not too small and if the ion concentration is not too low in the diffuse layer, the total capacitance C will be dominated by the quantum capacitance of graphene near the neutrality point. This confirms that using the dependence of the minimum in C on the applied potential V_a for sensing measurements corresponds to the regime where charge density on graphene vanishes $\sigma_g = 0$ in Equation (5.5) and, accordingly, $V_g = 0$.

5.2 Inclusion of Trapped Charges in the Oxide Layer

When considering the case of a functionalized graphene, a thin layer of oxide will be placed between graphene and the diffuse layer (see Figure 5.2). The oxide layer helps to increase the adsorption capabilities of graphene and normally comes in the form of an oxide that will provide a non-covalent functionalization of graphene [21, 82]. It is necessary for this bonding between the oxide and graphene to provide this non-covalent functionalization so that the unique electronic band structure of graphene remains unmodified [156]. Typical oxides used in experiments are tantalum pentoxide (Ta_2O_5), aluminum oxide (Al_2O_3), and silicon dioxide (SiO_2), due to their use in ISFETs and well understood surface chemistry [21, 82, 156, 157, 158]. More recently, hafnium dioxide (HfO_2), has also been of interest as a functional layer, and has shown some promising results [159]. The relevant experimental parameters of these oxides can be found in Table 5.1. The main focus of the discussion here will be on tantalum pentoxide (Ta_2O_5) and aluminum oxide (Al_2O_3), as these oxides appear to be most popular in sensor design.

Oxide	pK_a	pK_b	ϵ_{ox}	N_s (nm^{-2})	δ
Ta_2O_5	4	2	22	10	10^{-1}
Al_2O_3	10	6	14	8	10^{-2}
HfO_2	7	7	25	4	1
SiO_2	6	-2	3.9	5	10^{-4}

Table 5.1: Experimental values for typical oxides used as functional layers [160].

An important design feature of oxides is the existence of charged impurities or charged traps within the bulk of the oxide or at its interface with graphene [8, 161]. These impurities (or atomic defects) can trap and de-trap charge carriers from graphene, and may cause degradation of the conductivity due to fluctuations in the available density for electrical conduction and due to Coulomb scattering [162, 163]. Because these impurities also contribute a net charge to the system, an additional surface charge density is included, $\sigma_t = N_t t$, to account for these oxide traps, where N_t is the effective volume density of trapped impurities and t is the oxide thickness.

To include the addition of oxide layer trapped charges between graphene and the diffuse layer, there is an additional boundary condition arising from the Gaussian pillbox on the graphene–oxide interface (see Figure 5.2), giving

$$-\epsilon_{ox}\left(\frac{\phi_a - \phi_g}{t}\right) = 4\pi\sigma_g + 4\pi\sigma_t\left(1 - \frac{d}{t}\right) \tag{5.27}$$

$$C_{ox}V_{ox} = -\sigma_g - \sigma_t\left(1 - \frac{d}{t}\right), \tag{5.28}$$

where $C_{ox} = \frac{\epsilon_{ox}}{4\pi t}$, is the capacitance of the oxide layer of thickness t, σ_t is the volume density of charged impurities in the oxide layer, and $0 \leq d \leq t$ is the average distance in the oxide where the impurities are located. The charge neutrality condition when charged impurities are included is generalized to

$$\sigma_g + \sigma_t + \sigma_a + \sigma_d = 0, \tag{5.29}$$

which comes from replacing the right hand side of Equation (5.27) into Equation (5.2). To discard the traps in the oxide layer, set $\sigma_t = 0$ in Equation (5.29) and Equation (5.4) is recovered.

At the neutrality point or the point of zero charge, the Fermi level is equal to the Dirac point energy level, i.e. $\varepsilon_F = \varepsilon_D$ (see Figure 3.4 on Page 37), so that $V_g = 0$ at this point. Under this condition, the surface charge density vanishes, $\sigma_g = 0$ as a consequence (comes from Equation (5.5)). Therefore, Equation (5.28) becomes

$$C_{ox}V_{ox} = -\sigma_t\left(1 - \frac{d}{t}\right), \tag{5.30}$$

and the total applied potential V_a is the sum of the diffuse layer potential V_d and the oxide potential V_{ox}. Interestingly, the choice to use graphene as an electrode does not play a key role in the sensitivity of the device, but does allow for clear minima to form in the conductivity or capacitance, which provide precise measurements of the sensitivity [8].

Because both the surface charge density of the adsorbed layer σ_a and the surface charge density of the diffuse layer σ_d are functions of the diffuse layer potential V_d, the following substitution is made:

$$
\begin{aligned}
V_d &= V_a - V_{ox} && (5.31)\\
&= V_a + \frac{\sigma_t\left(1-\frac{1}{2}\right)}{C_{ox}} && (5.32)\\
&= V_a + \frac{2\pi e}{\epsilon_{ox}} N_t t^2 && (5.33)\\
\implies \overline{V}_d &= \overline{V}_a + \ell_{ox} N_t t^2, && (5.34)
\end{aligned}
$$

upon substitution of Equation (5.28), and where $\overline{V}_d = ze\beta V_d$ and $\overline{V}_a = ze\beta V_a$ are the normalized potentials of the diffuse layer and total applied potential respectively, and $\ell_{ox} = \frac{2\pi e^2}{\epsilon_{ox} k_B T} \approx \frac{361.91}{\epsilon_{ox}}$ nm. Here, $d = t/2$ is fixed, which describes the case of a uniform distribution of charged impurities throughout the oxide layer.

5.3 Sensitivity Relations from the Charge Neutrality Condition

The sensitivity of graphene-based sensors is accessed by plotting the potential at which either the capacitance or conductivity is a minimum against the ion concentration or the pH when the measurement was taken. At the potential minimum, the Fermi energy ε_F in graphene coincides with the Dirac point energy ε_D and hence, the potential drop across graphene is $V_g = 0$ and the surface charge density on graphene is $\sigma_g = 0$ (Equation (5.5). Therefore, the only contribution to the potential at the minimum in the conductivity or capacitance is from the oxide (V_{ox}) and the diffuse layer (V_d) and so the total applied potential becomes $V_a = V_{ox} + V_d$. At the same time, the overall charge neutrality condition, Equation (5.29) must be satisfied, and hence, the potential at the minimum is numerically accessible by inverting the system of equations.

To obtain solutions for the potential at the neutrality point, the system of equations given by Equations (5.7), (5.16), (5.30), and (5.34) is solved subject to the neutrality constraint given by Equation (5.29). Comparisons will be made between the potential minima obtained from the proposed model above and experimental data from two groups: a group of Heller [76] at the University of Twente where the minima in the graphene conductivity are plotted against ion concentration and a group led by Szkopek [82] at McGill University where the minima are plotted against pH.

Constant pH Regime

In the case of the Heller group [76], the graphene sheet is in direct contact with the electrolyte solutions composed of lithium chloride (LiCl) and potassium chloride (KCl) and phosphate buffer (PB) is added to keep the pH of the system constant over the electrolyte concentration range. They utilize graphene-based FETs, which have an underlying oxide layer of silicon dioxide. The experimental data presented by Heller *et al.* is averaged over 13 graphene devices [76], and their measurements in both electrolytic solutions, LiCl and KCl, show that they have identical sensitivities (slopes), with only a small vertical offset between salts. Because the experiment does not make use of a functional layer, the density of oxide traps $N_t = 0$, the charge density $\sigma_t = 0$, and the potential drop across the oxide is $V_{ox} = 0$. The neutrality condition is then simply $\sigma_a(V_d) + \sigma_d(V_d) = 0$. Both surface charge densities are only functions of the diffuse layer potential, which allows the calculation to reduce down to numerically inverting the charge neutrality condition for V_d.

The experiment considers two different pH levels: pH $= 3$ and pH$= 7$, with the experimental parameters reported by the group given in Table 5.2. Heller *et al.* assumes that binding proceeds as in the site binding model with binding sites being deprotonated from neutral to a -1 charge (H$^+$ being given to the electrolyte), remaining neutral, or being protonated from neutral to a $+1$ charge (H$^+$ removed from the electrolyte) [76].

Parameter	Value
N_s	0.5 nm^{-2}
pK_a	4.5
pK_b	4.5
pH	3 (black lines) and 7 (blue lines)
ϕ_N	$\ln(10)(4.5 - pH)$

Table 5.2: Experimental values from Heller *et al.*, where the graphene sheet is in direct contact with the electrolytic solution [76]. Here, it is assumed that the binding occurs directly on the surface of graphene, and the underlying oxide layer has no effects.

In Figure 5.3, the neutrality point, or potential of zero charge, V_pzc is plotted verses concentration of LiCl. The solid line correspond to the solution obtained by considering the mobile ions in the electrolyte as point charges, i.e. with diffuse layer surface charge σ_d given by the Poisson-Boltzmann expression in Equation (5.6). While the overall shape of the solution is in good agreement with the shape of the experimental points, the magnitude of the potential is not in agreement. The dashed line shows the solution obtained by adding the effects of finite size in the diffuse layer, i.e. replacing Equation (5.6) with Equation (5.7). The addition of steric effects appears to decrease the slope of the neutrality point potential in both cases, but does not bring the model results into better agreement with experimental data.

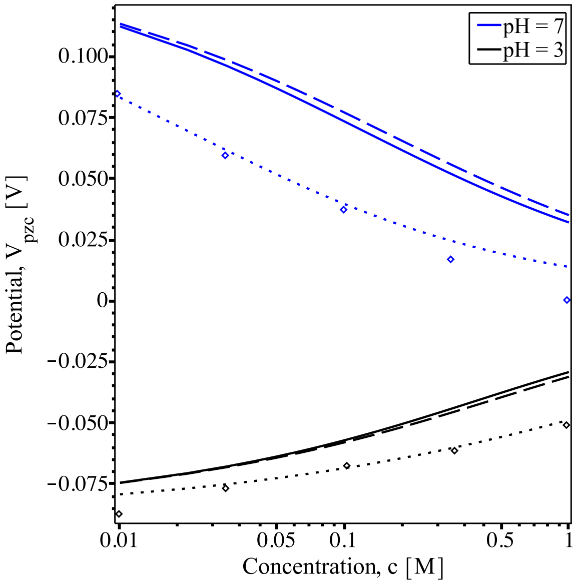

Figure 5.3: Results for the Heller *et al.* experiment of the potential at the neutrality point, or point of zero charge (V_{pzc}), plotted verses LiCl concentration. Experimental data are shown as points and are taken from Figure 2 d) in [76], the model with no steric effects in the diffuse layer is shown as the solid lines, and the model with steric effects is shown as the dashed line. In an effort to bring the minima from the model in closer agreement with the experimentally observed potential values, variations in the number of binding sites, N_s, are made: $N_s = 0.2\ \text{nm}^{-2}$ for pH= 7 (blue dotted lines) and $N_s = 0.9\ \text{nm}^{-2}$ for pH= 3 (black dotted lines).

Interestingly, adjusting the number of binding sites N_s allows the solution for the neutrality point potential V_{pzc} to agree very well with the observed experimental values. For the case of pH= 3 (black lines), increasing the number of binding sites N_s to 0.9 nm^{-2}, brings the model into good agreement with the observed potential minima, which is plotted as the black dotted line in Figure 5.3. For the case of pH= 7 (blue lines), decreasing the number of binding sites N_s to 0.2 nm^{-2}, brings the model down to better agreement with the measured experimental values. Due to the chemical inertness of graphene, it is expected that the adsorption of ions on the surface would only occur at defects in the hexagonal lattice. Therefore, charged impurities in the silicon dioxide substrate could promote adsorption due to the thinness of graphene [5], which provide some functionalization through charged impurities. This could be attracted electrostatically to protons or hydroxyl groups to bind to the graphene–electrolyte interface, and hence, the number of binding sites of a bare graphene may deviate from the quoted value of $N_s = 0.5\ \text{nm}^{-2}$. This could be tested experimentally by varying the density of traps in the underlying oxide from a low (or zero) density to a high density to observe the change in the potential minima. Alternatively, since bare graphene is known to be chemically inert, adding a functional layer to graphene would remove any effects of the oxide substrate, and likely lead to more accurate modelling of the sensitivity to ion concentration, as is the case in the constant concentration regime below. It would also be worthwhile to apply a coating, e.g. parylene, to the graphene surface in either the bare graphene case or functionalized graphene case to prevent degradation of the surface over multiple experiments, as in the case of the work of Szkopek *et al.* [21, 82], discussed in more detail below.

Sensitivity to Ion Concentration

Using a least-squares method to calculate the line of best fit for the solutions found in Figure 5.3 gives sensitivities of approximately 23 mV/M for pH= 3 and 34 mV/M for pH= 7 for the dotted lines (with adjusted number of binding sites). Similar slopes are obtained when the number of binding sites is $N_s = 0.5\ \text{nm}^{-2}$. These slopes show that the sensitivity to ion concentration is a median value to those quoted by other experimental groups, who measured the sensitivity of a graphene-based sensor to be approximately 6 mV/M [38] in one set and approximately 55 mV/M [30] in another. These groups also utilized a graphene-based FET, in which the graphene sheet was in direct contact with the electrolyte. However, they simply diluted their solutions without using a buffer to maintain a constant pH [30, 38].

The sensitivity in these cases is highly dependent on the quality of the graphene used, as defects in the lattice structure give rise to binding sites N_s for protons and hydroxyl groups. If the sheet of graphene has more defects, it would be expected to have a higher sensitivity to adsorption than that of a pristine sheet of graphene that is chemically inert [5]. Hence, discrepancies in the uniformity of the graphene sheets used by each group could give rise to different sensitivities.

Constant concentration regime

In the case Szkopek *et al.* [82], two different oxide layers, 5 nm of tantalum pentoxide (Ta_2O_5) and 3 nm of aluminum dioxide (Al_2O_3), are deposited on top of graphene to help promote adsorption of ions to the surface. In addition, the layer of graphene is wrapped with a layer of parylene, which is a polymer that helps to prevent the degradation of the graphene surface during multiple experiments and provides a non-covalent functionalization so that the unique band structure of graphene remains intact [164, 165]. The experimental measurements were done with an electrolytic buffer, sodium phosphate (Na_3PO_4), at a concentration of 20 mM. The relevant experimental values can be found in Table 5.3 [82]. Note that the experimental section of their work does not quote a density of charged impurities in each oxide. Consequently, typical values in the $10^{12} - 10^{13}$ cm^{-2} range are considered [161], and the best fit values for the density of impurities are provided in Table 5.3.

Oxide: Al_2O_3	Value
c	0.02 M
ϕ_N	$\ln(10)(8 - pH)$
N_t	-0.032 nm^{-3}
t	3 nm
σ_t	-0.096 $\mathrm{e/nm}^2$
δ	10^{-2}
Oxide: Ta_2O_5	Value
c	0.02 M
ϕ_N	$\ln(10)(3 - pH)$
N_t	-0.01 nm^{-3}
t	5 nm
σ_t	-0.05 $\mathrm{e/nm}^2$
δ	10^{-1}

Table 5.3: Experimental values from the Szkopek *et al.* group, where there is an oxide layer placed between graphene and the electrolytic solution [82].

In Figure 5.4, the neutrality point potential V_{pzc} is plotted verses pH. The solid lines indicate the solutions obtained when considering the mobile ions in the electrolyte as point charges, i.e., with σ_d given by the Possion-Boltzmann expression in Equation (5.6). Likewise with Figure 5.3, the overall trend of the solutions for both oxides is in good agreement with the shape of the experimental points. When the mobile ions are considered to have finite size, i.e., when Equation (5.6) is replaced with Equation (5.7) for σ_d, the dashed lines in Figure 5.4 are obtained. The addition of steric effects into the model brings the solutions into excellent agreement with the observed experimental values. In the standard Poisson-Boltzmann model for the surface charge density σ_d (Equation (5.6)), all ions are treated as point charges, and therefore, have equal ability to move in the bulk electrolyte and adsorb on the oxide surface. However, the diffuse layer contains hydrated salt ions, which are much larger than point charges and the protons and hydroxyl groups responsible for binding. The large size of the hydrate ions inhibits the movement of the smaller protons and hydroxyl groups, and hence a smaller proportion of these groups can engage in binding at the oxide–electrolyte interface. This dependence on the inclusion of finite ion size effects in the diffuse layer could be experimentally confirmed by taking potential minima measurements with electrolytic solutions of varying ion sizes to identify the effects of ion size on the minima. The inclusion of finite ion size in the diffuse layer, the dotted lines in Figure 5.4, suggest that steric effects diffuse layer exist, and are an important phenomena in the modelling of experimental data.

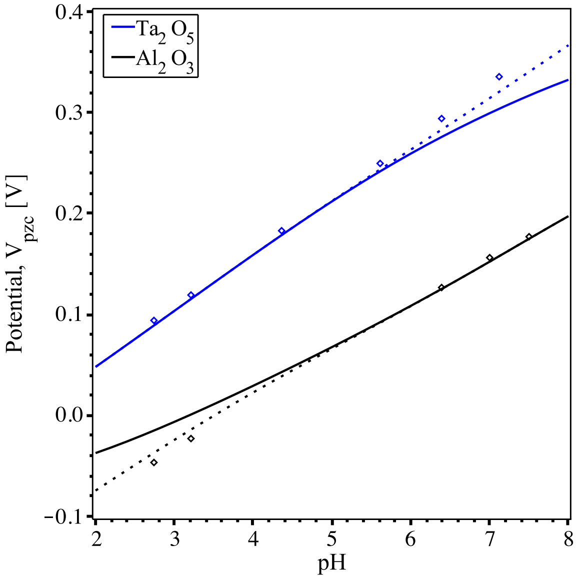

Figure 5.4: Results reported by Szkopek *et al.* on the dependence of the neutrality point potential V_{pzc} on pH. Experimental data are shown as points and are taken from Figure 3 c) in [82]; the model with no steric effects in the diffuse layer is shown as the solid lines, and the model with steric effects is shown as the dotted lines.

The site binding model and steric effects in the diffuse layer provide a direct link between the modelling of graphene-based sensors and the experimental data for these sensors. The agreement between the data and the model is impressive, and provide insight into the important physical systems in graphene sensors: the inclusion of an oxide layer that promotes binding at the oxide–electrolyte interface, the inclusion of an adsorbed layer, which allows for protons and hydroxyl groups to bind, and the inclusion of steric effects in the diffuse layer. This experimental validation of the site binding model is encouraging for advancing the understanding and theoretical modelling of graphene-based sensors.

Sensitivity to pH

Similar to the sensitivity to ion concentration, a least-squares method to calculate the line of best fit for the solutions in Figure 5.4 gives sensitivities of approximately 44 mV/pH for Al_2O_3 and 53 mV/pH for Ta_2O_5. These slopes compare favourably with those reported by other groups, who find the sensitivity for functionalized graphene FETs to be in the range of $30 - 60$ mV/pH [32, 33]. To identify experimental parameters which affect the sensitivity of the device, Figure 5.5 shows variations of the neutrality point V_{pzc} with pH for different parameter values. The oxide used in all cases is 5 nm of Ta_2O_5, and unless specified, the experimental values are consistent with those in Tables 5.1 and 5.3.

In panel a) of Figure 5.5, the ratio of the dissociation constants $\delta = \sqrt{\frac{K_{\text{a}}}{K_{\text{b}}}}$ is varied for constant number of binding sites ($N_s = 10\ \text{nm}^{-2}$) oxide thickness (5nm), and concentration ($c = 0.1$ M). The range of δ is chosen so that it is consistent with the typical values for oxides. When $\delta \geq 1$, the minima become independent of pH values. The sensitivities for increasing δ are: 4 mV/pH, 18 mV/pH, 42 mV/pH, and 56 mV/pH (in the case of $\delta = 1$ and $\delta = 2$), showing that increasing δ corresponds to a direct increase in the sensitivity. A larger dissociation constant for the reaction $AOH \leftrightharpoons AO^- + H^+$, which breaks up the hydroxyl group and allows for more free protons to be given to the system, yields a more sensitive response.

Panel b) of Figure 5.5 shows the results when the number of binding sites N_s is varied at constant oxide thickness, concentration, and δ set to 1. The sensitivities at increasing N_s are: 25 mV/pH, 30 mV/pH, 37 mV/pH, and 42 mV/pH, indicating that an increase in the number of binding sites also yields a direct increase in the sensitivity. An increase in the number of binding sites allows for more interactions to take place at the oxide–electrolyte interface.

In panel c) of Figure 5.5, the results of varying the concentration with constant oxide thickness, the ratio of dissociation constants δ, and binding sites N_s is shown. For increasing

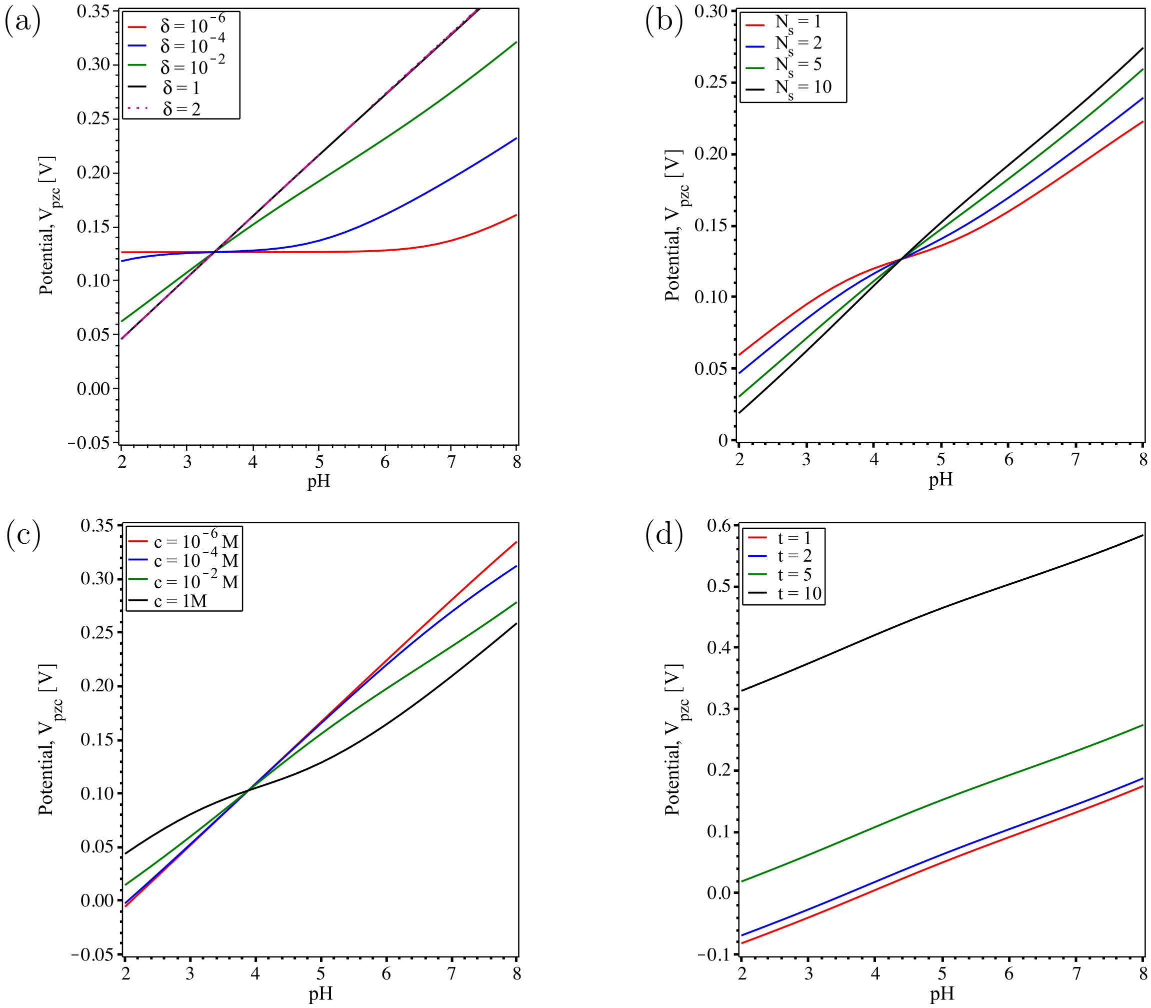

Figure 5.5: Plots of the potential at the neutrality point, or point of zero charge (V_{pzc}), plotted with respect to increasing pH. Panel a) shows results for several values of increasing $\delta = \sqrt{\frac{K_{\text{a}}}{K_{\text{b}}}}$, panel b) shows results for increased number of binding sites N_s, panel c) shows results for increasing concentrations from micromole to molar, and panel d) shows results for different thicknesses of oxides. For all panels, unless otherwise stated, parameters are consistent with those for the oxide tantalum pentoxide found in Tables 5.1 and 5.3.

concentrations, the sensitivities are: 57 mV/pH, 54 mV/pH, 44 mV/pH, and 33 mV/pH, which show that for increasing concentrations, the sensitivity decreases. Due to the site binding model only taking into account the adsorption of protons and hydroxyl groups, it may be that with increasing electrolyte concentration, that there is some competition between the different ions (protons, hydroxide, and salt ions) during the adsorption process, and so for large concentrations, the protons and hydroxyl groups are inhibited from binding on the surface.

Panel d) of Figure 5.5 plots the results for increasing oxide thickness at constant concentration c, δ, and number of binding sites N_s. For this configuration, the sensitivity is constant at approximately 44 mV/pH, and increasing the oxide thickness only shifts V_{pzc} upward.

Given Figure 5.5, it is the ratio of dissociation constants, δ, the number of binding sites N_s, and the concentrations that can alter sensitivity. The case of the latter is an easily controllable external parameter; however, δ and N_s are material dependent and are not easily adjusted. To adjust these two parameters, fabrication processes would need to be altered to obtain the desired number of binding sites N_s and ratio of dissociation constants δ.

5.4 Concluding Remarks

Site binding theory is used to study the effect of ion adsorption on the neutrality point potential in a graphene-based sensor. Two configurations of sensors are considered: one where graphene is in direct contact with the electrolyte and one where a thin layer of oxide is placed between graphene and the electrolyte. The sensitivity of the neutrality point to changes in ion concentration and pH were considered, and comparisons were made between the model solution and experimental data. In addition, the inclusion of finite ion size in the diffuse layer of the electrolyte was also considered.

Because the adsorbed layer is a subsystem of the overall diffuse layer, its capacitance comes in a parallel connection with the diffuse layer capacitance. This combined adsorbed layer and diffuse layer capacitance then comes as a series connection with the oxide layer and graphene electrode, which is consistent with previous modelling with and without an adsorbed layer.

In the case of sensitivity to ion concentration, the site binding model does yield results which are in fair agreement with experimental data. The inclusion of finite ion size in the diffuse layer does not affect the neutrality point potential drastically, but slightly reduces the slope of the lines. By allowing for adjustments in the number of binding sites, N_s, the neutrality point potentials are brought into excellent agreement with the experimental data when steric effects are included.

For the regime of constant concentration where sensitivity to pH is measured, the site binding model performs well compared to the experimental data. When steric effects are included in the diffuse layer so that a finite amount of charge is able to approach the electrode, the model yields results which are almost identical to the experimental data, with no adjustments needed to experimentally documented values. The sensitivities of both oxides considered were relatively high, but within the normally observed range of $30 - 60$ mV/pH [21, 30, 38, 82].

To be able to control the sensitivity of the graphene-based FET, adjustments to the concentration, pH, ratio of dissociation constants δ and the number of available binding sites N_s play an important role in the site binding model. Changes in these parameters result in a direct to changes in the predicted sensitivity. Although this model of site-binding only considers the adsorption of protons and hydroxl groups to the surface, it would be interesting to allow for the adsorption of salt ions. It could then be investigated to determine if the competition between these different ionic species affects their ability to adsorb onto the surface and the corresponding change in the neutrality point of the system.

Chapter 6

Conclusions and Future Work

6.1 Summary

This research focused on various aspects of modelling a graphene-based biochemical sensor in the configuration of a field effect transistor. These sensors have a sheet of graphene in contact with either an electrolytic solution or ionic liquid. The quantum capacitance of graphene is much smaller than the capacitance of the diffuse layer, and hence, dominates in the system near the point of zero charge. The smallness of the quantum capacitance gives rise to more sensitive devices when the field effect transistor is operated in capacitor mode, which makes modelling of the differential capacitance of such sensors a primary interest.

In Chapter 3, the interactions of a metallic and graphene electrode with a liquid electrolyte are considered. A free energy functional is used to derive self consistent equations for the concentration of ions and a modified Poisson-Boltzmann equation. This modified Poisson-Boltzmann equation includes the effects of finite ion size in the diffuse layer coupled with two different effects in the dielectric permittivity of the electrolyte: dielectric saturation and dielectric decrement. In the case of dielectric saturation, the Booth model is used to modify the dielectric permittivity of the diffuse layer to be dependent on the magnitude of the electric field. In the case of dielectric decrement, a linearized model that is dependent on the concentration of mobile ions is used to account for the so-called excess ion polarizability effect in the diffuse layer. Because the modified Poisson-Boltzmann equation is not dependent on the position variable (distance x into the electrolyte from the electrode surface), the Beltrami identity is used to obtain analytic functions for the first integral of this equation, which can then be used to obtain analytic functions for the capacitance of the diffuse layer. For both regimes of modifications to the dielectric permittivity, a charge-free Stern layer is considered between the electrode and the diffuse layer, as well as the effects of both a metallic and graphene electrode. The capacitances in the diffuse layer exhibit both camel- and bell-shaped dependence on the potential drop across that layer for certain combinations of experimental parameters. The Stern layer acts to broaden the peaks in the capacitance and to reduce the magnitude of the capacitance to bring them into closer agreement with experimentally observed capacitances. Near the point of zero charge, as expected, the total capacitance is dominated by the quantum capacitance of graphene in both regimes of dielectric modification and finite ion size effects.

The interactions and capacitance of graphene in contact with an ionic liquid were discussed in Chapter 4. Due to ionic liquids being devoid of solvent molecules, the Coulomb correlations between charged mobile ions become non-negligible and therefore a modification to the dielectric permittivity is required. This results in a fourth-order modified Poisson-Fermi equation, which does not have a general analytic solution. A numerical computation is used to obtain results for both a metallic electrode and a graphene electrode, as well as the cases when a Stern layer is added between the electrode and the diffuse layer and when asymmetric ion sizes are considered. Likewise with the solutions for electrolytes, both camel- and bell-shaped capacitances are observed in the diffuse layer, and the inclusion of a Stern layer lowers the magnitude and broadens the peaks of the capacitance. In the presence of a graphene electrode, the quantum capacitance again dominates near the point of zero charge and only camel-shaped capacitances are observed.

In Chapter 5, the sensitivity of graphene-based sensors is explored. A site binding model is used to allow for ion adsorption onto the surface of the graphene sensor. Both the case of bare graphene and a functionalized graphene, where a thin layer of oxide is placed on top of the graphene sheet, are considered. Solutions of the charge neutrality condition are obtained for both sensitivity to ion concentration (constant pH) and sensitivity to pH (constant ion concentration) and compared to experimental data. In both cases, the site binding model reproduces the experimental data quite well, particularly in the case when the sensitivity to pH is considered. Although graphene does not have a direct impact on the neutrality point and sensitivity, it is vital to the accuracy of devices as clear minima are observed in the conductivity and capacitance.

6.2 Future Work

In Chapter 3, the effects of dielectric saturation and dielectric decrement were considered as separate manifestations in the electrolyte. Future work should consider both effects in tandem in the electrolyte, and to analyze the interplay of these two effects. The conditions where one effect dominates or where both effects become comparable should be analyzed to obtain a fully modified model of the diffuse layer.

A more careful analysis of the boundary conditions for Poisson-Fermi equation in Chapter 4 was performed recently by Pedro *et al.* [149], and a set of new conditions was derived enforcing the continuity of the Maxwell stress at a charged interface, which upholds the contact theorem for dilute primitive-model electrolytes. The solutions obtained for ionic liquids will change under these new boundary conditions, and implementation of the new conditions should be performed to analyze the similarities and differences of the boundary conditions.

In the case of adsorption, the model presented here assumes that only protons and hydroxyl groups were able to bind to the surface. Further work should allow for multiple layers of adsorption and the adsorption of the salt ions to make further refinements to the model, particularly in the case of constant pH where the sensitivity is with respect to the ion concentration. At large ion concentrations, the competition between the different sized ion groups to adsorb onto the surface may play a significant role in the neutrality point potential. Furthermore, a recent paper by Parizi *et al.* [155] allowed for the inclusion of steric effects in the adsorbed layer. A careful analysis of this result and their methodology for including finite ion size in this regime is also necessary.

In addition, combining the work in Chapter 3 with Chapter 5 so that the adsorption model includes the effects of dielectric saturation and dielectric decrement in the diffuse layer would be a next step for modelling. This would yield a fully modified model for graphene-based biochemical sensors, which would be interesting to analyze for the interplay of the effects in the diffuse layer with the effects of adsorption.

The work in this thesis assumes that the applied potential comes from a direct current, i.e. the electric field does not depend on time. It would be interesting to consider that the electric field is time-dependent, e.g. in the case of alternating current. With every switch of direction in the electric field, ions would be redistributed in the diffuse layer as oppositely charged ions move either to or from the electrode surface.

References

[1] L. H. Hess, M. Seifert, and J. A. Garrido. Graphene transistors for bioelectronics. *Proc. IEEE*, 101:1780–1792, 2013.

[2] L. Bousse and P. Bergveld. The role of buried oh sites in the response mechanism of inorganic-gate ph-sensitive isfets. *Sens. and Act.*, 6:65–78, 1984.

[3] E. Cabruja, A. Merlos, C. Cané, M. Lozano, J. Bausells, and J. Esteve. Influence of the degradation on the surface states and electrical characteristics of eos structures. *Surface Sci.*, 251:364–368, 1991.

[4] S. Ren, P. Rong, and Q. Yu. Preparations, properties and applications of graphene in functional devices: a concise review. *Cer. Intl.*, 44:11940–11955, 2008.

[5] D. J. Cole, P. K. Ang, and K. P. Loh. Ion adsorption at the graphene/electrolyte interface. *J. Phys. Chem. Lett.*, 2:1799–1803, 2011.

[6] P. Avouris and F. Xia. Graphene applications in electronics and photonics. *MRS Bulletin*, 37:1225–1234, 2012.

[7] K. P. Loh, Q. Bao, P. K. Ang, and J. Yang. The chemistry of graphene. *J. Mater. Chem.*, 20:2277–2289, 2010.

[8] A. H. Castro Neto, F. Guinea, N. M. R. Peres, K. S. Novoselov, and A. K. Geim. The electronic properties of graphene. *Rev. Mod. Phys.*, 81:109–162, 2009.

[9] F. L. Liu, Y. Yu, C. Yan, K. Li, and Z. Zheng. Wearable energy-dense and power-dense supercapacitor yarns enabled by scalable graphene-metallic textile composite electrodes. *Nat. Comm.*, 6:7260, 2015.

[10] A. R. Wright, X. G. Xu, J. C. Cao, and C. Zhang. Strong nonlinear optical response of graphene in the terahertz regime. *Appl. Phys. Lett.*, 95:072101, 2009.

[11] F. Rana. Graphene terahertz plasmon oscillators. *IEEE Trans. Nanotech.*, 7:91–99, 2008.

[12] L. Liu, X. Doug, and P. Chen. Biological and chemical sensors based on graphene materials. *Chem. Soc. Rev.*, 41:2283–2307, 2012.

[13] D. Jarwala, V. K. Sangwan, L. J. Lauhon, T. J. Marks, and M. C. Hersam. Carbon nanomaterials for electronics, optoelectronics, photovoltaics, and sensing. *Chem. Soc. Rev.*, 42:2824–2860, 2013.

[14] K. Balasubramanian and K. Kern. Label-free electrical biodetection using carbon nanostructures. *Adv. Mater.*, 26:1154–1175, 2014.

[15] P. Kang, M.C. Wang, and S. Nam. Bioelectronics with two-dimensional materials. *Microelectronic Engineering*, 161:18–35, 2016.

[16] S. Chen, Z. B. Zhang, L. Ma, P. Ahlberg, Z. Gao, Z. Qiu, D. Wu, W. Ren, H. M. Cheng, and S. L. Zhang. A graphene field-effect capacitor sensor in electrolyte. *Applied Phys. Lett.*, 101:154106, 2012.

[17] F. Chen, J. Xia, and N. Tao. Ionic screening of charged-impurity scattering in graphene. *Nano Lett.*, 9:1621–1625, 2009.

[18] H. Ji, X. Zhao, Z. Qiao, J. Jung, Y. Zhu, Y. Lu, L. L. Zhang, A. H. MacDonald, and R. S. Ruoff. Capacitance of carbon-based electrical double- layer capacitors. *Nature Communications*, 5:3317, 2014.

[19] F. Chen, Q. Qing, J. Xia, and N. Tao. Graphene field-effect transistors: Electrochemical gating, interfacial capacitance, and biosensing applications. *Chem. Asian J.*, 5:2144–2153, 2010.

[20] M. H. Lee, B. J. Kim, K. H. Lee, I. S. Shen, W. Huh, J. H. Cho, and M. S. Kang. Apparent pH sensitivity of solution-gated graphene transistors. *Nanoscale*, 7:7540–7544, 2015.

[21] I. Fakih, S. Sabri, F. Mahvash, M. Nannini, M. Siaj, and T. Szkopek. Large area graphene ion sensitive field effect transistors with tantalum pentoxide sensing layers for pH measurement at the Nernstian limit. *App. Phys. Lett.*, 105:083101, 2014.

[22] Y. Yang, A M. Asiri, Z. Tang, D. Du, and Y. Lin. Graphene based materials for biomedical applications. *Mater. Today*, 16:365–373, 2013.

[23] B. G. Streetman and S. Banerjee. *Solid State Electronic Devices.* Prentice Hall, United States of America, 5th edition, 2000.

[24] S. T. Thornton and A. Rex. *Modern Physics for Scientists and Engineers.* Brooks/Cole Cengage Learning, United States of America, 3rd edition, 2006.

[25] P. Sharma and Z. L. Miskovic. Capacitance of graphene in aqueous electrolytes: The effects of dielectric saturation of water and finite size of ions. *Phys. Rev. B*, 90:125415, 2014.

[26] A. A. Balandin. Low-frequency $1/f$ noise in graphene devices. *Nature Nanotechnolody*, 8:549–555, 2013.

[27] Y. Ohno, K. Maehashi, Y. Yamashiro, and K. Matsumoto. Electrolyte-gated graphene field-effect transistors of detecting pH and protein adsorption. *Nano Lett.*, 9:3318–3322, 2009.

[28] A. J. Bard and L. R. Faulkner. *Electrochemical Methods: Fundamentals and Applications.* John Wiley & Sons, United States of America, 2nd edition, 2001.

[29] S. Chen, Z. B. Zhang, L. Ma, P. Ahlberg, Z. Gao, Z. Qiu, D. Wu, W. Ren, H. M. Cheng, and S. L. Zhang. A graphene field-effect capacitor sensor in electrolyte. *Applied Phys. Lett.*, 101:154106, 2012.

[30] F. Chen, Q. Qing, J. Xia, J. Li, and N. Tao. Electrochemical gate-controlled charge transport in graphene in ionic liquid and aqueous solution. *J.A.C.S. Commun.*, 131:9908–9909, 2009.

[31] P. K. Ang, W. Chen, A. T. S. Wee, and K. P. Loh. Solution-gated epitaxial graphene as pH sensor. *J. Am. Chem. Soc.*, 130:14392–14393, 2008.

[32] W. Fu, C. Nef, O. Knopfmacher, A. Tarasov, M. Weiss, M. Calame, and C. Schönenberger. Graphene transistors are insensitive to pH changes in solution. *Nano Lett.*, 11:3597–3600, 2011.

[33] W. Fu, C. Nef, M. Wipf, R. Stoop, O. Knopfmacher, M. Weiss, M. Calame, and C. Schönenberger. High mobility graphene ion-sensitive field-effect transistors by noncovalent functionalizations. *Nanoscale*, 5:12104–12110, 2013.

[34] L. Bousse, N. F. de Rooij, and P. Bergveld. The influence of counter-ion adsorption on the ψ_0/ph characteristics of insulator surfaces. *Surface Sci.*, 135:479–496, 1983.

[35] P. Bergveld and A. Sibbald. *Comprehensive Analytical Chemistry Volume XXIII: Analytical and Biomedical Applications of Ion-Selective Field-Effect Transistors.* Elsevier Science Publishers B.V., Netherlands, 1988.

[36] R. E. G. van Hal, J. C. T. Eijkel, and P. Berveld. A novel description of isfet sensitivity with the buffer capacity and double-layer capacitance as key parameters. *Sensors and Actuators B*, 24-25:201–205, 1995.

[37] J. Xia, F. Chen, J.Li, and N. Tao. Measurement of the quantum capacitance of graphene. *Nature Nano.*, 4:505–509, 2009.

[38] R. X. He, P. Lin, Z. K. Liu, H. W. Zhu, X. Z. Zhao, H. L. W. Chan, and F. Yan. Solution-gated graphene field effect transistors integrated in microfluidic systems and used for flow velocity detection. *Nano Lett.*, 12:1404–1409, 2012.

[39] Z. L. Miskovic, P. Sharma, and F. O. Goodman. Ionic screening of charged impurities in electrolytically gated graphene. *Phys. Rev. B*, 86:115437, 2012.

[40] L. Daniels, M. Scott, and Z. L. Mišković. The role of stern layer in the interplay of dielectric saturation and ion steric effects for the capacitance of graphene in aqueous electrolytes. *J. Chem. Phys.*, 146:094101, 2017.

[41] L. Daniels, M. Scott, and Z. L. Mišković. The effects of dielectric decrement and finite ion size on differential capacitance of electrolytically gated graphene. *Chem. Phys. Lett.*, 701:43–51, 2018.

[42] Y. Bai, Y. Cao, J. Zhang, M. Wang, R. Li, P. Wang, S. M. Zakeeruddin, and M. Gratzel. High-performance dye-sensitized solar cells based on solvent-free electrolytes produced from eutectic melts. *Nature Mater.*, 7:626–630, 2008.

[43] A. Lewandowski and M. Galinski. Carbon - ionic liquid double-layer capacitors. *J. Phys. Chem. Solids*, 65:281–286, 2004.

[44] V. Lockett, R. Sedev, J. Ralston, M. Horne, and T. Rodopoulos. Differential capacitance of the electrical double layer in imidazolium-based ionic liquids: Influence of potential, cation size, and temperature. *J. Phys. Chem. C*, 112:7486–7495, 2008.

[45] P. Simon and Y. Gogotsi. Materials for electrochemical capacitors. *Nat. Mater.*, 7:845–854, 2008.

[46] M. Jitvisate and J. R. T. Seddon. Direct measurement of the differential capacitance of solvent-free and dilute ionic liquids. *J. Chem. Phys. Lett.*, 9:126–131, 2018.

[47] J. Ye, M. F. Craciun, M. Koshino, S. Russo, S. Inoue, H. Yuan, H. Shimotani, H. Shimotani, A. F. Morpurgo, and Y. Iwasa. Accessing the transport properties of graphene and its multilayers at high carrier density. *Proceed. Nat. Acad. Sci. USA*, 108:13002–13006, 2011.

[48] M. Z. Bazant, M. S. Kilic, B. D. Storey, and A. Ajdari. Towards an understanding of induced-charge electrokinetics at large applied voltages in concentrated solutions. *Adv. Colloid Interface Sci.*, 152:48–88, 2009.

[49] M. Z. Bazant, B. D. Storey, and A. A Kornyshev. Double layer in ionic liquids: Overscreening versus crowding. *Phys. Rev. Lett.*, 106:046102, 2011.

[50] H. Helmholtz. Ueber einige gesetze der vertheilung elektrischer ströme in körperlichen leitern mit anwendung auf die thierisch-elektrischen versuche. *Annlen der Phyik*, 165:211–233, 1853.

[51] M. G. Gouy. Sur la consitution de la charge Électrique à la surface d'un Électrolyte. *J. Phys. Radium*, 9:457–468, 1910.

[52] D. L. Chapman. A contribution to the theory of electrocapillarity. *Philos. Mag.*, 6:475–481, 1913.

[53] O. Z. Stern. Zur theorie der elektrolytischen doppelschicht. *Electrochem.*, 30:508–516, 1924.

[54] D. Silvester. Recent advances in the use of ionic liquids for electrochemical sensing. *Analyst*, 136:4871–4882, 2011.

[55] M. J. A. Shiddiky and A. A. J. Torriero. Application of ionic liquids in electrochemical sensing systems. *Biosens. and Bioelec.*, 26:1775–1787, 2011.

[56] M. V. Fedorov and A. A. Kornyshev. Ionic liquids at electrified interfaces. *Chem Rev.*, 114:2978–3036, 2014.

[57] Z. A. H. Goodwin and A. A. Kornyshev. Underscreening, overscreening and double-layer capacitance. *Electrochem. Comm.*, 82:129–133, 2017.

[58] M. A. Gebbie, A. M. Smith, H. A. Dobbs, A. A. Lee, G. G. Warr, X. Banquy, M. Valtiner, M. W. Rutland, J. N. Israelachvili, S. Perkin, and R. Atkin. Long range electrostatic forces in ionic liquids. *Chem. Commun.*, 53:1214–1224, 2017.

[59] P. Walden. Molecular weights and electrical conductivity of several fused salts. *Bull. Imp. Acad. Sci.*, 1800:405–422, 1914.

[60] H. L. Chum, V. R. Koch, L. L. Miller, and R. A. Osteryoung. Electrochemical scrutiny of organometallic iron complexes and hexamethylbenzene in a room temperature molten salt. *JACS*, 97:3264–3265, 1975.

[61] J. S. Wilkes, J. A. Levisky, R. A. Wilson, and C. L. Hussey. Dialkylimidazolium chloroaluminate melts: a new class of room-temperature ionic liquids for electrochemistry, spectroscopy and synthesis. *Inorg. Chem.*, 21:1263–1264, 1982.

[62] T. Brousse, D Bélanger, and J. W. Long. To be or not to be pseudocapacitive? *J. Electrochem. Soc.*, 162:A5185–A5189, 2015.

[63] T. Brezesinski, J. Wang, S. H. Toblert, and B. Dunn. Ordered mesoporous α-moo$_3$ with iso-oriented nanocrystalline walls for thin-film pseudocapacitors. *Nat. Mater.*, 9:146–151, 2010.

[64] S. Kondrat and A. A. Kornyshev. Pressing a spring: what does it take to maximize the energy storage in nanoporous supercapacitors? *Nano. Hori.*, 1:45–52, 2016.

[65] A. A. Kornyshev. Double-layer in ionic liquids: paradigm change? *J. Phys. Chem. B*, 111:5545–5557, 2007.

[66] M. V. Fedorov and A. A. Kornyshev. Towards understanding the structure and capacitance of electrical double layer in ionic liquids. *Electrochim. Acta*, 53:6835 – 6840, 2008.

[67] B. D. Storey and M. Z. Bazant. Effects of electrostatic correlations on electrokinetic phenomena. *PRE*, 86:056303, 2012.

[68] Y. Han, S. Huang, and T. Yan. A mean-field theory on the differential capacitance of asymmetric ionic liquid electrolytes. *J. Phys.: Condens. Matt.*, 26:284103, 2014.

[69] Z. A. H. Goodwin, G. Feng, and A. A. Kornyshev. Mean-field theory of electrical double layer in ionic liquids with account of short-range correlations. *Electrochimica Acta*, 225:190 – 197, 2017.

[70] R. Downing, B. K. Berntson, G. V. Bossa, and S. May. Differential capacitance of ionic liquids according to lattice-gas mean-field model with nearest-neighbor interactions. *J. Chem. Phys.*, 149:204703, 2018.

[71] R. Downing, G. V. Bossa, and S. May. The role of ion–ion correlations for the differential capacitance of ionic liquids. *J. Phys. Chem. C*, 122:28537–28544, 2018.

[72] A. Gupta and H. A. Stone. Electrical double layers: effects of asymmetry in electrolyte valence on steric effects, dielectric decrement, and ion-ion correlations. *Langmuir*, 34:11971–11985, 2018.

[73] S. Lamperski, J. Sosnowska, L. B. Bhuiyan, and D. Henderson. Size asymmetric hard spheres as a convenient model for the capacitance of the electrical double layer of an ionic liquid. *J. Chem. Phys.*, 140:014704, 2014.

[74] P. Bergveld. Development of an ion-sensitive solid-state device for neurophysiological measurements. *IEE Trans. Biomed. Eng.*, 17:70–71, 1970.

[75] L. Zuccaro, J. Krieg, K. Kern, and K. Balasubramanian. Tuning the isoelectric point of graphene by electrochemical functionalization. *Scientific Reports*, 5:11794, 2015.

[76] I. Heller, S. Chatoor, J. Männik, M. A. G. Zevenbergen, C. Dekker, and S. G. Lamay. Influence of electrolyte composition on liquid gated carbon nanotube and graphene transistors. *J. Am. Chem. Soc.*, 132:17149–17156, 2010.

[77] P. Bergveld and A. Sibbald. *Comprehensive Analytical Chemistry Volume XXIII: Analytical and Biomedical Applications of Ion-Selective Field-Effect Transistors*. Elsevier Science Publishers B.V., Netherlands, 1988.

[78] P. W. Atkins. *Physical Chemistry*. Oxford University Press, 1990.

[79] J. Duval, J. Mieke Kleijn, J. Lyklema, and H. P. van Leeuwen. Double layers at amphifunctionally electrified interfaces in the presence of electrolytes containing specifically adsorbing ions. *J. Electroanal. Chem.*, 532:337–352, 2002.

[80] L. Bousse, N. F. de Rooij, and P. Bergveld. Operation of chemically sensitive field-effect sensors as a function of the insulator-electrolyte interface. *IEEE*, 30:1263–1270, 1983.

[81] G. Trefalt, S. H. Behrens, and M. Borkovec. Charge regulations in the electrical double layer: Ion adsorption and surface interactions. *Langmuir*, 32:380–400, 2016.

[82] I. Fakih, F. Mahvash, M. Siaj, and T. Szkopek. Sensitive precise pH measurement with large-area graphene field-effect transistors at the quantum-capacitance limit. *PRA*, 8:044022, 2017.

[83] R. J. H. Clark and D. Brown. *The Chemistry of Vanadium, Niobium and Tantalum.* Elsevier, United States of America, 1^{st} edition, 1973.

[84] A. F. Holleman, E. Wiberg, and N. Wiberg. *Inorganic Chemistry.* Academic Press, United States of America, 2001.

[85] T. Ihn. *Semiconductor Nanostructures: Quantum States and Electronic Transport.* Oxford University Press, United Kingdom, 2010.

[86] P. R. Wallace. The band theory of graphite. *Phys. Rev.*, 71:622–634, 1947.

[87] K. S. Novoselov, D. Jiang, F. Schedin, T. J. Booth, V. V. Khotkevich, S. V. Morozov, and A. K. Geim. Two-dimensional atomic crystals. *PNAS*, 102:10451–10453, 2005.

[88] K. S. Novoselov, A. K. Geim, S. V. Morozov, D. Jiang, M. I. Katsnelson, I. V. Grigorieva, S. V. Dubonos, and A. A. Firsov. Two-dimensional gas of massless dirac fermions in graphene. *Nature*, 438:197–200, 2005.

[89] A. K. Geim and K. S. Novoselov. The rise of graphene. *Nat. Mater.*, 6:183–191, 2007.

[90] P. Sutter. How silicon leaves the scene. *Nat. Mater.*, 8:171–172, 2009.

[91] Y. Sun, L. Yang, K. Xia, H. Liu, D. Han, Y. Zhang, and J. Zhang. “Snowing” graphene using microwave ovens. *Adv. Mater.*, 30:1803189, 2018.

[92] Z. Xu (Editor). *Graphene: Properties, Synthesis, and Applications.* Nova Science Publishers, Inc., United States of America, 2011.

[93] K. Leo. Organic semiconductor world. `https://web.archive.org/web/20150418183833/http://www.orgworld.de/`, 2015.

[94] S. Reich, J. Maultzsch, C. Thomsen, and P. Ordejón. Tight-binding description of graphene. *Phys. Rev. B*, 66:035412, 2002.

[95] S. Das Sarma, S. Adam, E. H. Hwang, and E. Rossi. Electronic transport in two-dimensional graphene. *Rev. Mod. Phys.*, 83:407–470, 2011.

[96] J. J. Bikerman. Structure and capacity of the electrical double layer. *Philos. Mag.*, 33:384–397, 1942.

[97] I. Borukhov, D. Andelman, and H. Orland. Steric effects in electrolytes: A modified poisson-boltzmann equation. *Phys. Rev. Lett.*, 79:435–438, 1997.

[98] D. C. Grahame. Effects of dielectric saturation upon the diffuse double layer and the free energy of hydration of ions. *J. Chem. Phys.*, 18:903–909, 1950.

[99] F. Chen, Q. Qing, J. Xia, and N. Tao. Graphene field-effect transistors: Electrochemical gating, interfacial capacitance, and biosensing applications. *Chem. Asian J.*, 5:2144–2153, 2010.

[100] V. Freise. Zur theorie der diffusen doppelschicht. *Z. Elektrochem.*, 56:822–*27, 1952.

[101] D. Ben-Yaakov, D. Andelman, D. Harries, and R. Podgornik. Beyond standard poisson-boltzmann theory: Ion-specific interactions in aqueous solutions. *J. Phys: Condens. Matter*, 21:424106, 2009.

[102] D. Ben-Yaakov, D. Andelman, and R. Podgornik. Dielectric decrement as a source of ion-specific effects. *J. Chem. Phys.*, 134:074705, 2011.

[103] M. M. Hatlo, R. van Roij, and L. Lue. The electric double layer at high surface potentials: The influence of excess ion polarizability. *EPL*, 97:28010, 2012.

[104] L. Sandberg and R. Edholm. Nonlinear response effects in continuum models of the hydration of ions. *J. Chem. Phys.*, 116:2936–2944, 2002.

[105] E. Gongadze, U. van Rienen, V. Kralj-Iglic, and A. Iglic. Spatial variation of permittivity of an electrolyte solution in contact with a charged metal surface: A mini review. *Comp. Methods in Biomech. and Biomed. Eng.*, 16:463–480, 2013.

[106] G. B. Arken and H. J. Weber. *Mathematical Methods for Physicists.* Harcourt/Academic Press, United States of America, 5th edition, 2001.

[107] H. Chen and I. Nakamura. Effects of the dielectric response of single-component liquids and liquid mixtures on electrochemical properties between charged plates. *J. Phys. Chem. C*, 119:24714–24723, 2015.

[108] N. Gavish and K. Promislow. Dependence of the dielectric constant of electrolyte solutions on ionic concentration: A microfield approach. *Phys. Rev. E*, 94:012611, 2016.

[109] M. Aguilella-Arzo, A. Andrio, V. M. Aguilella, and A. Alcaraz. Dielectric saturation of water in a membrane protein channel. *Phys. Chem. Chem. Phys.*, 11:358–365, 2009.

[110] V. N. Paunov, R. I. Dimova, P. A. Kralchevshy, G. Broze, and A. Mehreteab. The hydration repulsion between charged surfaces as an interplay of volume exclusion and dielectric saturation effects. *J. Colloid Interface Sci.*, 182:239–248, 1996.

[111] H. Wang, J. Varghese, and L. Pilon. Simulation of electric double layer capacitors with mesoporous electrodes: Effects of morphology and electrolyte permittivity. *Electrochimica Acta*, 56:6189–6197, 2011.

[112] H. Wang and L. Pilon. Accurate simulations of electric double layer capacitance of ultramicroelectrodes. *J. Phys. Chem. C*, 115:16711–16719, 2011.

[113] F. Booth. The dielectric constant of water and the saturation effect. *J. Chem. Phys.*, 19:391–394, 1951.

[114] I. C. Yeh and M. L. Berkowitz. Dielectric constant of water at high electric fields: Molecular dynamics studys. *J. Chem. Phys.*, 110:7935–7942, 1999.

[115] R. L. Fulton. The nonlinear dielectric behavior of water: Comparisons of various approaches to the nonlinear dielectric increment. *J. Chem. Phys.*, 130:204503, 2009.

[116] X. Duan and I. Nakamura. A new lattice Monte Carlo simulation for dielectric saturation in ion-containing liquids. *Soft Matter*, 11:3566–3571, 2015.

[117] J. R. MacDonald. Theory of the differential capacitance of the double layer in unadsorbed electrolytes. *J. Chem. Phys.*, 22:1857–1866, 1954.

[118] J. R. MacDonald and C. A. Barlow Jr. Theory of double-layer differential capacitance in electrolytes. *J. Phys. Chem. C*, 36:3062–3080, 1962.

[119] S. Gavryushov and P. Linse. Polarization deficiency and excess free energy of ion hydration in electric fields. *J. Phys. Chem. B*, 107:7135–7142, 2003.

[120] B. Figliuzzi, W. H. R. Chan, C. R. Buie, and J. L. Moran. Nonlinear electrophoresis in the presence of dielectric decrement. *Phys. Rev. E*, 94:023115, 2016.

[121] Y. Nakayama and D. Andelman. Differential capacitance of the electric double layer: The interplay between ion finite size and dielectric decrement. *J. Chem. Phys.*, 142:044706, 2015.

[122] G. Minton and L. Lue. The influence of excluded volume and excess ion polarisability on the capacitance of the electric double layer. *Mol. Phys.*, 114:2477–2491, 2016.

[123] J.J. López-García, J. Horno, and C. Grosse. Differential capacitance of the diffuse double layer at electrode-electrolyte interfaces considering ions as dielectric spheres: Part 1. binary electrolyte solutions. *J. Coll. and Inter. Sci.*, 496:531–539, 2017.

[124] J. B. Hasted, D. M. Ritson, and C. H. Collie. Dielectric properties of aqueous ionic solutions. parts i and ii. *J. Chem. Phys.*, 16:1–21, 1948.

[125] F. Chen, J. Xia, and N. Tao. Ionic screening of charged-impurity scattering in graphene. *Nano Lett.*, 9:1621–1625, 2009.

[126] M. S. Kilic, M. Z. Bazant, and A. Ajdari. Steric effects in the dynamics of electrolytes at large applied voltages. i. double-layer charging. *Phys. Rev. E*, 75:021502, 2007.

[127] G. Valette. Double layer on silver single-crystal electrodes in contact with electrolytes having anions which present a slight specific adsorption. *J. Electroanal. Chem.*, 122:285–297, 1981.

[128] A. Velikonja, E. Gongadze, V. Kralj-Iglic, and A. Iglic. Charge dependent capacitance of stern layer and capacitance of electrode/electrolyte interface. *Int. J. Electrochem. Sci.*, 9:5885–5894, 2014.

[129] M. A. Brown, A. Goel, and A. Abbas. Effect of electrolyte concentration on the stern layer thickness at a charged interface. *Angew. Chem. Int. Ed.*, 55:3790–3794, 2016.

[130] M. A. Brown, A. Abbas, A. Kleibert, R. G. Green, A. Goel, S. May, and T. M. Squires. Determination of surface potential and electrical double-layer structure at the aqueous electrolyte-nanoparticle interface. *Phys. Rev. X*, 6:011007, 2016.

[131] X. Du, H. Guo, Y. Jin, Q. Jin, and J. Zhao. Electrochemistry investigation on the graphene/electrolyte interface. *Electroanalysis*, 27:2760–2765, 2015.

[132] J. Kierzenka and L. F. Shampine. A bvp solver based on residual control and the maltab pse. *ACM Trans. Math. Softw.*, 27:229–316, 2001.

[133] D. Silvester and R. Compton. Electrochemistry in room temperature ionic liquids: A review and some possible applications. *Z. Phys. Chem.*, 220:1247–1274, 2006.

[134] M. Armand, F. Endres, D. R. MacFarlane, H. Ohno, and B. Scrosati. Ionic-liquid materials for the electrochemical challenges of the future. *Nature Mater.*, 8:621–629, 2009.

[135] T. Welton. Room-temperature ionic liquids. solvents for synthesis and catalysis. *Chem. Rev.*, 99:2071–2084, 1999.

[136] M. Antonietti, D. Kuang, B. Smarsly, and Y. Zhou. Ionic liquids for the convenient synthesis of functional nanoparticles and other inorganic nanostructures. *Angewandte Chemie International Edition*, 43:4988–4992, 2004.

[137] R. Hayes, G. G. Warr, and R. Atkin. Structure and nanostructure in ionic liquids. *Chem. Rev.*, 115:6357–6426, 2015.

[138] E. Uesugi, H. Goto, R. Eguchi, A. Fujiwara, and Y. Kubozono. Electric double-layer capacitance between an ionic liquid and few-layer graphene. *Sci. Rep.*, 3:01595, 2013.

[139] E. Paek, A. J. Pak, and G. S. Hwang. A computational study of the interfacial structure and capacitance of graphene in [bmim][pf$_6$] ionic liquid. *J. Electrochem. Soc.*, 160:A1–A10, 2013.

[140] A A. Kornyshev, N. B. Luque, and W. Schmickler. Differential capacitance of ionic liquid interface with graphite: the story of two double layers. *J. Solid State Electrochem.*, 18:1345–1349, 2014.

[141] R. Blossey, A. C. Maggs, and R. Podgornik. Structural interactions in ionic liquids linked to higher-order poisson-boltzmann equations. *PRE*, 95:060602, 2017.

[142] M. V. Fedorov and A. A. Kornyshev. Ionic liquid near a charged wall: Structure and capacitance of electrical double layer. *J. Phys. Chem. B*, 112:11868–11872, 2008.

[143] M. Merlet, B. Rotenberg, P. A. Madden, and M. Salanne. Computer simulations of ionic liquids at electrochemical interfaces. *Phys. Chem. Chem. Phys.*, 15:15781–15792, 2013.

[144] M. M. Islam, M. T. Alam, and T. Ohsaka. Electrical double-layer structure in ionic liquids: A corroboration of the theoretical model by experimental results. *J. Phys. Chem. C*, 112:16568–16574, 2008.

[145] A. Shalabi, L. Daniels, M. Scott, and Z. Miskovic. Differential capacitance of ionic liquid interface with graphene: the effects of correlation and finite size of ions. *Electrochimica Acta*, 319:423–434, 2019.

[146] C. D. Santangelo. Computing counterion densities at intermediate coupling. *Phys. Rev. E*, 73:041512, 2006.

[147] G. Feng, M. Chen, S. Bi, Z. A. H. Goodwin, E. Postinikov, N. Brilliantov, M. Urbakh, and A. A. Kornyshev. Free and bound states of ions in ionic liquids, conductivity, and underscreening paradox. *Phys. Rev. X*, 9:021024, 2019.

[148] M. S. Kilic, M. Z. Bazant, and A. Ajdari. Steric effects in the dynamics of electrolytes at large applied voltages. i. double-layer charging. *Phys. Rev. E*, 75:021502, 2007.

[149] J. P. de Souza and M. Z. Bazant. Continuum theory of electrostatic correlations at charged surfaces. *arXiv:1902.05493*, 2019.

[150] A. C. Maggs and R. Podgornik. General theory of asymmetrical steric interactions in electrostatic double layers. *Soft Matt.*, 12:1219–1229, 2016.

[151] L. Yin, Y. Huang, H. Chen, and T. Yan. A mean-field theory on the differential capacitance of asymmetric ionic liquid electrolytes. ii. accounts of ionic interactions. *Phys. Chem. Chem. Phys.*, 20:17606–17614, 2018.

[152] O. Oll, T. Romann, C. Siimenson, and E. Lust. Influence of chemical composition of electrode material on the differential capacitance characteristics of the ionic liquid – electrode interface. *Electrochemi. Comm.*, 82:39–42, 2017.

[153] R. Anicic and Z. L. Miskovic. Potential fluctuations in graphene due to correlated charged impurities in substrate. *Appl. Phys. Lett.*, 17:171606, 2013.

[154] O. Moldovan, B. Iñiguez, M. J. Deen, and L. F. Marsal. Graphene electronic sensors - review of recent developments and future challenges. *IET Circ. Dev. Sys.*, 9:446–453, 2015.

[155] K. B. Parizi, X. Xu, A. Pal, X. Hu, and H.S. P. Wong. Isfet pH sensitivity: counter-ions play a key role. *Sci. Rep.*, 7:41305, 2017.

[156] V. Georgakilas, M. Otyepka, A. B. Bourlinos, V. Chandra, N. Kim, K. C. Kemp, P. Hobza, R. Zboril, and K. S. Kim. Functionalization of graphene: covalent and non-covalent approaches, derivatives, and applications. *Chem. Rev.*, 112:6156–6214, 2012.

[157] Z. Jiang and D. Stein. Electrofluidic gating of a chemically reactive surface. *Langmuir*, 26:8161–8173, 2010.

[158] S. Kim, J. Nah, I. Jo, D. Shahrjerdi, L. Colombo, Z. Yao, E. Tutuc, and S. K. Banerjee. Realisation of a high mobility dual-gated graphene field-effect transistor with Al_2O_3 dielectric. *App. Phys. Lett.*, 94:062107, 2009.

[159] S. K. Ameri, P. K. Singh, and S. R. Sonkusale. Three dimensional graphene transistor for ultra-sensitive pH sensing directly in biological media. *Analy. Chim. Acta*, 934:212–217, 2016.

[160] Editor: J. Rumble. *CRC Handbook of Chemistry and Physics.* CRC Press, United States of America, 99th edition, 2018.

[161] R. Anicic and Z. L. Miskovic. Effects of the structure of charged impurities and dielectric environment on conductivity of graphene. *Phys. Rev. B*, 88:205412, 2013.

[162] A. A. Baladin. Low-frequency $1/f$ noise in graphene devices. *Nat. Nanotech.*, 8:549–555, 2013.

[163] S. Adan, E. H. Hwang, V. M. Galitski, and S. D. Sarma. A self-consistent theory for graphene transport. *Proceed. Nat. Acad. Sci.*, 104:18392–18397, 2007.

[164] S. S. Sabri, P.L. Levesque, C. M. Aguirre, J. Guillemette an R. Martel, and T. Szkopek. Graphene field effect transistors with parylene gate dielectric. *Appl. Phys. Lett.*, 95:242104, 2009.

[165] P. L. Levesque, S. S. Sabri, C. M. Aguirre, J. Guillemette, M. Saij, P. Desjardins, T. Szkopek, and R. Martel. Probing charge transfer at surfaces using graphene transistors. *Nano Lett.*, 11:132–137, 2011.

[166] L. Onsager. Electric moments of molecules in liquids. *J. Am. Chem. Soc.*, 58:1486–1493, 1936.

APPENDICES

Appendix A

Stationary Points of Free Energy Functional

In this appendix, a derivation of the Poisson-Boltzmann equation using calculus of variations is presented.

The free energy of the system is given by $F = U - TS$, where U is the internal energy of the system, T is the temperature (in Kelvin), and S in the entropy of the system [51, 52, 96]. By treating mobile ions in a $Z : Z$ symmetric electrolyte as point charges, the internal energy of the system is given by the functional

$$U = \iiint\limits_{\Omega} \left[-\frac{\epsilon}{8\pi} (\nabla\phi)^2 + Ze(c_+ - c_-)\phi \right] d^3\vec{r} + \iint\limits_{\partial\Omega} \sigma_0 \phi_0 d^2\,\vec{r}, \tag{A.1}$$

where Ω is the volume occupied by the electrolyte, ϵ is the dielectric permittivity of the solvent (assumed constant), ϕ is the electrostatic potential, Ze the charge on the ionic species, c_+ and c_- are the local concentrations of positive and negative ions respectively, σ_0 is the surface density of free charges on the boundary $\partial\Omega$, and ϕ_0 is the surface value of the potential ϕ. Using an entropy of an ideal gas of point-like ions [97], the entropic contribution is given by the functional

$$-TS = \frac{1}{\beta} \iiint\limits_{\Omega} \left[c_+ \ln\left(\frac{c_+}{c_\infty}\right) + c_- \ln\left(\frac{c_-}{c_\infty}\right) - c_+ - c_- \right] d^3\vec{r}, \tag{A.2}$$

where c_∞ is the bulk concentration of each ionic species and $\beta = \frac{1}{k_B T}$ with k_B being the Boltzmann constant and T the temperature.

Minimization with respect to potential, ϕ

Set $\phi = u + \lambda v$, where u and v are permissible functions in Ω. To find a function u such that the functional F has a stationary value, set the derivative with respect to λ to zero:

$$\frac{d}{d\lambda}\left\{\iiint\limits_{\Omega}\left[-\frac{\epsilon}{4\pi}\|\nabla u + \lambda\nabla v\|^2 + Ze(c_+ - c_-)\,(u+\lambda v)\right]d^3\vec{r}\right.$$
$$\left.+\iint\limits_{\partial\Omega}\sigma_0\,(u_0 + \lambda v_0)\,d^2\vec{r}\right\}\Bigg|_{\lambda=0} = 0. \tag{A.3}$$

Applying the derivative gives

$$\iiint\limits_{\Omega}\left[-\frac{\epsilon}{4\pi}\nabla u\cdot\nabla v + Ze(c_+ - c_-)v\right]d^3\vec{r} + \iint\limits_{\partial\Omega}\sigma_0 v_0\,d^2\vec{r} = 0. \tag{A.4}$$

Next, integrate the first term in the integral by parts to convert ∇v to v:

$$\iiint\limits_{\Omega}\nabla u\cdot\nabla v = -\iiint\limits_{\Omega}v\nabla^2 u\,d^3\vec{r} + \iint\limits_{\partial\Omega}v_0\hat{n}\cdot\nabla u_0 d^2\,\vec{r} = 0, \tag{A.5}$$

where $\hat{n}$ is the outward unit normal vector to the boundary $\partial\Omega$. The final form of the variation, when set to zero to find the stationary points, is then:

$$\iiint\limits_{\Omega}v\left[\frac{\epsilon}{4\pi}\nabla^2 u + Ze(c_+ - c_-)\right]d^3\vec{r} + \iint\limits_{\partial\Omega}v_0\left(-\frac{\epsilon}{4\pi}\hat{n}\cdot\nabla u_0\sigma_0\right)d^2\vec{r} = 0. \tag{A.6}$$

Because Equation (A.6) is true for all variations v and v_0, it then follows that the resulting Euler-Lagrange equation for u yields the well-known Poisson equation

$$\frac{\epsilon}{4\pi}\nabla^2\phi = -Ze(c_+ - c_-), \tag{A.7}$$

and the stationary condition for u_0 gives the Neumann boundary condition

$$\epsilon\hat{n}\cdot\nabla\phi\Big|_{z=0} = 4\pi\sigma_0. \tag{A.8}$$

Minimization with respect to concentrations, $c_\pm$

Set $c_+ = u_+ + \lambda v_+$, where u_+ and v_+ are permissible functions in Ω. To determine a stationary value of the functional F, set the derivative with respect to λ to zero:

$$\frac{d}{d\lambda}\left\{\iiint_\Omega \left[Ze\phi\left(u_+ + \lambda v_+\right)\right] d^3\vec{r} \right.$$
$$\left. + \frac{1}{\beta}\iiint_\Omega \left[\left(u_+ + \lambda v_+\right)\ln\left(\frac{u_+ + \lambda v_+}{c_\infty}\right) - \left(u_+ + \lambda v_+\right)\right]\, d^3\vec{r}\right\}\Bigg|_{\lambda=0} = 0. \quad \text{(A.9)}$$

Applying the derivative gives:

$$\iiint_\Omega \left[Ze\phi v_+\right] d^3\vec{r} + \frac{1}{\beta}\iiint_\Omega v_+ \ln\left(\frac{u_+}{c_\infty}\right)\, d^3\vec{r} = 0. \quad \text{(A.10)}$$

The final form of the variation, when set to zero to find the stationary points, is

$$\iiint_\Omega \left[Ze\phi + \frac{1}{\beta}\ln\left(\frac{u_+}{c_\infty}\right)\right] v_+\, d^3\vec{r} = 0. \quad \text{(A.11)}$$

Similarly, by setting $c_- = u_- + \lambda v_-$, where u_- and v_- are permissible functions in Ω, the variation with respect to concentrations c_- gives

$$\iiint_\Omega \left[-Ze\phi + \frac{1}{\beta}\ln\left(\frac{u_-}{c_\infty}\right)\right] v_-\, d^3\vec{r} = 0. \quad \text{(A.12)}$$

Because Equations (A.11) and (A.12) are valid for all variations v_+ and v_-, it then follows that

$$\pm\, Ze\phi + \frac{1}{\beta}\ln\left(\frac{u_\pm}{c_\infty}\right) = 0. \quad \text{(A.13)}$$

Rearranging Equation (A.13), and reverting back to the original symbol for concentrations $c_\pm$ gives

$$c_\pm = c_\infty e^{\mp Ze\beta\phi}, \quad \text{(A.14)}$$

which is the well-known Boltzmann distribution of ions. Substituting Equation (A.14) into Equation (A.7) gives the Poisson-Boltzmann equation.

Appendix B

Lattice Entropy

B.1 Entropic Contribution of Cations and Anions

The entropy of a solution containing cations and anions is calculated using a lattice model. Here, the system is divided into cells of equal size, with lattice spacing of the size of ion diameter a.

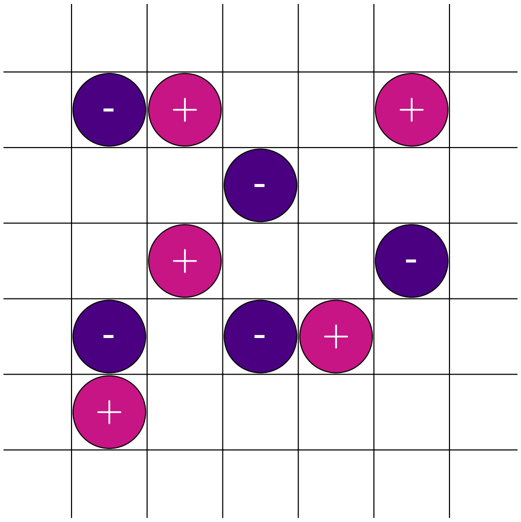

Figure B.1: Schematic representation of the lattice model with both cations and anions.

The total number of spatial arrangements of the cations and anions in a cell with N

lattice sites is

$$\Omega = \frac{N(N-1)(N-2)\ldots(N-(C-1))}{c_+!c_-!} \tag{B.1}$$

$$= \frac{N!}{c_+!c_-!(N-C)!}, \tag{B.2}$$

where $C = c_+ + c_-$, c_+ is the number of cations, and c_- is the number anions.

The total entropy of the system is then given by the Boltzmann formula:

$$S = k_B \ln \Omega. \tag{B.3}$$

By using Stirling's approximation for large C; i.e, $\ln C_i \simeq C_i \ln C_i - C_i$, $i = \{+,-\}$, the total entropy for the given system is:

$$\ln \Omega = N \ln N - N - C_+ \ln C_+ + C_+ - C_- \ln C_- + C_- - (N-C)\ln(N-C) + (N-C) \tag{B.4}$$

$$= N \ln N - C_+ \ln C_+ - C_- \ln C_- + (N-C) \ln\left(\frac{1}{N}\left(1 - \frac{C}{N}\right)\right) \tag{B.5}$$

$$= -C_+ \ln\left(\frac{C_+}{N}\right) - C_- \ln\left(\frac{C_-}{N}\right) - (N-C) \ln\left(\frac{1}{N}\left(1 - \frac{C}{N}\right)\right). \tag{B.6}$$

Here, the first term gives the entropic contribution of the cations, the second term gives the entropic contribution of the anions, and the last term represents the empty lattice spaces. In the case where the solution also contains water molecules, the last term is the entropic contribution of the water. For this case, note that in Figure B.1, the empty lattice spaces would represent the water molecules.

Appendix C

Derivation of the Booth Model

C.1 Spherical Cavity in Dielectric

Suppose a spherical cavity of radius a exists in an otherwise homogeneous material of dielectric constant ϵ, and a point dipole is located at the centre of the cavity is a point dipole $\vec{m}$, see figure C.1. Let the potential in the absence of the cavity be given by $\phi_0 = -Er\cos\theta$, where θ indicates the direction of the polar axis, which is oriented along the externally applied constant electric field $\vec{E}$. By introducing the cavity into the system, the potential inside the cavity is ϕ_i and outside the cavity is $\phi_0 + \phi_p$, where ϕ_p is the perturbation to the potential by introducing the cavity. Note that ϕ_p must decrease at large distances away from the cavity, at least as fast as $\frac{1}{r}$.

Now both the potential inside and outside the cavity must satisfy Laplace's equation:

$$\nabla^2(\phi_0 + \phi_p) = 0 \tag{C.1}$$

$$\nabla^2\phi_i = 0, \tag{C.2}$$

with boundary conditions

$$\phi_0 + \phi_p = \phi_i \qquad (r = a) \tag{C.3}$$

$$\epsilon\frac{\partial}{\partial r}(\phi_0 + \phi_p) = \frac{\partial \phi_i}{\partial r} \qquad (r = a). \tag{C.4}$$

Given the form of ϕ_0 and the boundary conditions, try a solution of the form:

$$\phi_i = -Br\cos\theta \tag{C.5}$$

$$\phi_p = -\frac{A}{r^2}\cos\theta, \tag{C.6}$$

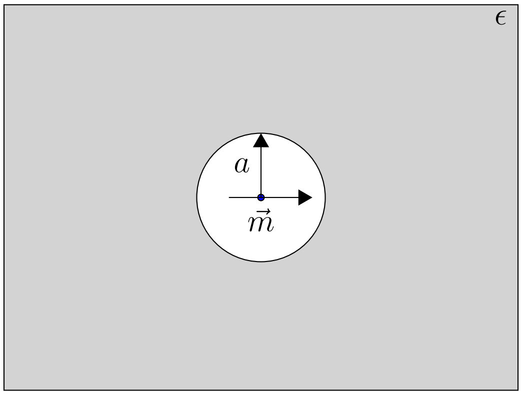

Figure C.1: Schematic showing the spherical cavity of radius a. For the first case, the dipole moment, $\vec{m}$, is zero.

where the coefficients A and B follow from the boundary conditions as

$$A = \frac{\epsilon - 1}{2\epsilon + 1} a^3 E \tag{C.7}$$

$$B = \frac{3\epsilon}{2\epsilon + 1} E. \tag{C.8}$$

The field inside the cavity is then given by

$$\vec{G} = -\frac{\partial}{\partial r}(\phi_i)\bigg|_{\cos\theta=1} \tag{C.9}$$

$$= \frac{3\epsilon}{2\epsilon + 1}\vec{E}. \tag{C.10}$$

Here, $\vec{G}$ is called the cavity field and is caused by and acts in the same direction as the applied field $\vec{E}$

C.2 Spherical Cavity with Point-Dipole in Dielectric

Suppose a spherical cavity of radius a exists in an otherwise homogeneous material of dielectric constant ϵ, and at the centre of the cavity is a point dipole $\vec{m}$ (Figure C.1), with $\vec{m}$ directed along the polar axis. Let the potential inside the cavity be given by $\phi_0 + \phi_p$, where by $\phi_0 = \frac{m}{r^2}\cos\theta$ is the potential that describes the field of a dipole in free space, with θ defining its direction with respect to the polar axis. Let the potential outside the cavity be given by ϕ_o.

The boundary conditions are:

$$\phi_0 + \phi_p = \phi_o \qquad (r = a) \tag{C.11}$$

$$\frac{\partial}{\partial r}(\phi_0 + \phi_p) = \epsilon\frac{\partial \phi_o}{\partial r} \qquad (r = a). \tag{C.12}$$

Since the form of ϕ_0 is known and the potential of the dipole is expected to decrease proportionally to the distance from the cavity as $\frac{1}{r^2}$, try a solution of the form:

$$\phi_p = -Ar\cos\theta \tag{C.13}$$

$$\phi_o = -\frac{B}{r^2}\cos\theta, \tag{C.14}$$

where the coefficients A and B follow form the boundary conditions as

$$A = -\frac{2(\epsilon - 1)}{2\epsilon + 1}\frac{m}{a^3} \tag{C.15}$$

$$B = \frac{3\epsilon}{2\epsilon + 1}m. \tag{C.16}$$

Then the field inside the cavity in the direction of the polar axis ($\cos\theta = 1$) is

$$-\frac{\partial}{\partial r}(\phi_0 + \phi_p)\bigg|_{\cos\theta = 1} = \frac{2m}{r^3} + \frac{2(\epsilon - 1)}{2\epsilon + 1}\frac{m}{a^3}, \tag{C.17}$$

where the second term is defined as the reaction field, $\vec{R}$, and tends to increase the dipole moment inside the cavity and acts in the same direction as the dipole.

C.3 Booth Dielectric Constant for Water using Onsager's Method

Now consider a polar molecule in a liquid, which is at the centre of a spherical cavity [166]. This molecule will become polarized under the influence of the reaction field, $\vec{R}$, and the cavity field, $\vec{G}$, so that the effective dipole moment of the molecule $\vec{m}$, which is not permanent, is given by $\vec{m} = \mu\vec{u} + \alpha(\vec{G} + \vec{R})$, where $\vec{u}$ is the unit vector in the direction of permanent dipole of the molecule, μ, and α is its polarizability. This relation is equivalent to:

$$\vec{m} = \mu_0\vec{u} + \left(\frac{3\epsilon}{2\epsilon+1}\vec{E} + \frac{2(\epsilon-1)}{2\epsilon+1}\frac{\vec{m}}{a^3}\right)\alpha, \tag{C.18}$$

where μ_0 is the permanent electric moment of the molecule. Solving this equation for $\vec{m}$ and substituting the polarizability α with the refractive index n given via the Clausius-Mossotti relation $\frac{n^2-1}{n^2+2} = \frac{4\pi}{3}N\alpha$ (N is the number density of molecules), gives

$$\vec{m} = \frac{(n^2+2)(2\epsilon+1)}{3(2\epsilon+n^2)}\mu_0\vec{u} + \frac{\epsilon(n^2+2)}{(2\epsilon+n^2)}\alpha\vec{E}, \tag{C.19}$$

using the fact that $\frac{4\pi}{3}a^3N = 1$. The torque acting on the dipole is $\vec{T} = (\vec{R}+\vec{G}) \times \vec{m}$. Since the reaction field is parallel to the dipole moment, $\vec{R} \times \vec{m} = 0$, the torque is

$$\begin{aligned}
\vec{T} &= \vec{G} \times \vec{m} && \text{(C.20)}\\
&= \frac{3\epsilon}{2\epsilon+1}\vec{E} \times \left(\frac{(n^2+2)(2\epsilon+1)}{3(2\epsilon+n^2)}\mu_0\vec{u} + \frac{\epsilon(n^2+2)}{(2\epsilon+n^2)}\alpha\vec{E}\right) && \text{(C.21)}\\
&= \frac{\epsilon(n^2+2)}{2\epsilon+n^2}\mu_0\vec{E} \times \vec{u} && \text{(C.22)}\\
&= \frac{\epsilon(n^2+2)}{2\epsilon+n^2}\mu_0 E\sin\theta\vec{\rho} && \text{(C.23)}\\
&= \mu^* E\sin\theta\vec{\rho}, && \text{(C.24)}
\end{aligned}$$

where $\vec{\rho}$ is the unit vector defining the axis about which the dipole rotates and

$$\mu^* = \frac{\epsilon(n^2+2)}{2\epsilon+n^2}\mu_0. \tag{C.25}$$

Then, the work done by the torque to reorient the dipole is found by solving the equation $\frac{\partial w}{\partial\theta} = \vec{T}\cdot\vec{\rho}$, so that $w = -\mu^* E\cos\theta$.

The component of $\vec{m}$ in the direction of the applied electric field is then given by

$$m_E = \frac{(n^2+2)(2\epsilon+1)}{3(2\epsilon+n^2)}\mu_0\cos\theta + \frac{\epsilon(n^2+2)}{(2\epsilon+n^2)}\alpha E. \tag{C.26}$$

To determine the average value of m_E, the average value of $\cos\theta$ is obtained using the

Boltzmann distribution of rotational energies of the dipole.

$$\overline{\cos\theta} = \frac{\displaystyle\int_0^{2\pi}\int_0^{\pi} e^{-\frac{w}{k_BT}}\cos\theta\sin\theta d\theta d\varphi}{\displaystyle\int_0^{2\pi}\int_0^{\pi} e^{-\frac{w}{k_BT}}\sin\theta d\theta d\varphi} \tag{C.27}$$

$$= \coth(x) - \frac{1}{x}, \tag{C.28}$$

where $x = \frac{\mu^* E}{k_B T}$. From the definition of polarization density,

$$\vec{P} = N\overline{\vec{m}_E} \tag{C.29}$$

$$= N\left(\frac{(n^2+2)(2\epsilon+1)}{3(2\epsilon+n^2)}\mu_0\left(\coth(x) - \frac{1}{x}\right) + \frac{\epsilon(n^2+2)}{2\epsilon+n^2}\alpha E\right)\vec{e}, \tag{C.30}$$

where $\vec{e} = \vec{E}/E$ is the unit vector pointing in the direction of the electric field. Using the electrostatic formula $(\epsilon - 1)\vec{E} = 4\pi\vec{P}$,

$$(\epsilon - 1)\vec{E} = 4\pi N\left(\frac{(n^2+2)(2\epsilon+1)}{3(2\epsilon+n^2)}\mu_0\left(\coth(x) - \frac{1}{x}\right) + \frac{\epsilon(n^2+2)}{2\epsilon+n^2}\alpha\right)\vec{e}. \tag{C.31}$$

Finally, rearranging and simplifying gives Booth's model for the dielectric permittivity:

$$\epsilon = n^2 + \frac{4\pi N(n^2+2)\mu_0}{3E}\left(\coth(x) - \frac{1}{x}\right). \tag{C.32}$$

Appendix D

Euler-Lagrange Formulation

In Lagrangian mechanics, the formulation comes from the principle of least action. To derive the Euler-Lagrange equation from Lagrangian mechanics, consider the Lagrangian functional, $L(q, \frac{dq}{dt}, t)$, and find a condition such that the action S becomes either maximal or minimal. This is done by considering small variation $\eta(t)$, with boundary conditions $\eta(t_1) = \eta(t_2) = 0$. For simplicity, denote $q' = \frac{dq}{dt}$. Then, the action S is

$$S = \int_{t_1}^{t_2} L(q + \varepsilon\eta(t), q' + \varepsilon\eta'(t), t)\, dt, \tag{D.1}$$

with extrema given by taking the derivative with respect to ε and setting the result equal to 0 [106].

$$
\begin{aligned}
\frac{d}{d\varepsilon}\int_{t_1}^{t_2} L(q+\varepsilon\eta(t),q'+\varepsilon\eta'(t),t)\,dt = \int_{t_1}^{t_2}\Bigg(&\frac{\partial}{\partial q}L(q+\varepsilon\eta(t),q'+\varepsilon\eta'(t),t)\,\delta(q+\varepsilon\eta(t))\\
&+\frac{\partial}{\partial q'}L(q+\varepsilon\eta(t),q'+\varepsilon\eta'(t),t)\,\delta(q'+\varepsilon\eta'(t))\\
&+\frac{\partial}{\partial \varepsilon}L(q+\varepsilon\eta(t),q'+\varepsilon\eta'(t),t)\Bigg)\,dt \qquad \text{(D.2)}\\
=\int_{t_1}^{t_2}\left(\frac{\partial L}{\partial q}\eta(t)+\frac{\partial L}{\partial q'}\eta'(t)\right)dt \qquad \text{(D.3)}\\
=\int_{t_1}^{t_2}\left(\frac{\partial L}{\partial q}-\frac{d}{dt}\frac{\partial L}{\partial q'}\right)\eta(t)\,dt=0 \qquad \text{(D.4)}\\
\Longrightarrow \frac{\partial L}{\partial q}-\frac{d}{dt}\frac{\partial L}{\partial q'}=0, \qquad \text{(D.5)}
\end{aligned}
$$

which is the well-known Euler-Lagrange equation.

D.1 Hamiltonian Mechanics

For a mechanical system, a Lagrangian, $L(q,q',t)$ can be constructed to describe the difference between the total kinetic energy and the potential energy. The generalized momentum for such systems is defend as

$$p=\frac{\partial L}{\partial q'}, \qquad \text{(D.6)}$$

which allows for the system to be solved for the generalized momentum. This connection is made through the Legendre transformation, $H = q'\frac{\partial L}{\partial q'} - L$, and provides a connection to Hamiltonian mechanics. The Legendre transform allows for a self-consistency check of each modification to the dielectric permittivity's first integral formulation.

The total derivative is of Legendre transformation is:

$$dH = p\,dq' + q'\,dp - \frac{\partial L}{\partial q}\,dq' - p'\,dq - \frac{\partial L}{\partial t}\,dt \qquad \text{(D.7)}$$

$$\Longrightarrow \; dH = q'\,dp - p'\,dq - \frac{\partial L}{\partial t}\,dt, \qquad \text{(D.8)}$$

which must be equivalent to $dH = \frac{\partial H}{\partial q}\,dq + \frac{\partial H}{\partial p}\,dp + \frac{\partial H}{\partial t}\,dt$. Matching the terms yields:

$$\frac{\partial H}{\partial p} = q' \tag{D.9}$$

$$\frac{\partial H}{\partial q} = -p' \tag{D.10}$$

$$\frac{\partial H}{\partial t} = -\frac{\partial L}{\partial t}. \tag{D.11}$$

In the context of the work here, the analogy comes from the 1D nature of the problem, with the spatial variable, x, taking the role of time, t, the potential ϕ taking the role of the generalized coordinate, q, and the conjugate momentum p being replaced by $\frac{D}{4\pi}$, where D is the dielectric displacement. Here, the standard relation of electromagnetism between dielectric displacement and electric field, $D = \epsilon_{\text{eff}} E$, is used, where $\epsilon_{\text{eff}} = \epsilon_{\text{Booth}}$ in the case of dielectric saturation and $\epsilon_{\text{eff}} = \epsilon_{\text{dec}}$ in the case of dielectric decrement. The Lagrangian is obtained as the negative of the functional U used in Chapter 3 to derive modifications to the Poisson-Boltzmann equation. By replacing the expressions for the ion concentrations into $L = -U$, the Lagrangian becomes now a function of $\phi(x)$ and $D(x)$, and the Hamilton equations are:

$$\frac{\partial H}{\partial D} = -E, \tag{D.12}$$

$$\frac{\partial H}{\partial \phi} = -4\pi\rho. \tag{D.13}$$

Note that since the "time" variable x is missing in the free energy functionals used in this work, the "conservation of energy" comes in the form $H(D, \phi) = \mathit{const}$, with the constant determined by the bulk values in the electrolyte. This conservation relation is equivalent to the first integrals obtained using Beltrami identity in Chapter 3 and expresses the fact that the osmotic pressure in the electrolyte is independent from the position x. In the following subsections, the Hamiltonian formulations will be derived for each modification to the Poisson-Boltzmann equation.

Dielectric Saturation

For the case of dielectric saturation, the Hamiltonian is obtained using the Legendre transformation to the Lagrangian $L = -U$ as,

$$H = -\Big[-4\pi w_e(|E|) + \epsilon_{Booth}(E)E^2 \Big] - \frac{8\pi c_\infty}{\beta\nu} \ln\left(1 + 2\nu \sinh^2\left(\frac{ze\beta\phi}{2}\right)\right), \tag{D.14}$$

$$= -\int_0^E \Big[\epsilon_{Booth}(\tilde{E}) + \tilde{E}\epsilon'_{Booth}(\tilde{E})\Big]\, \tilde{E}\, d\tilde{E} - 4\pi \int_0^\phi \rho(\tilde{\phi})\, d\tilde{\phi}, \tag{D.15}$$

using Equation (3.3). Equation (D.15) is written in integral form by replacing the expression in the second term with the expression for the charge density ρ (Equation (3.7)).

Utilizing the fact that $E = \frac{D}{\epsilon_{\text{Booth}}}$ and considering D to be a function of E and ϕ, the Hamilton's equations yield:

$$\frac{\partial H}{\partial D} = \frac{\frac{\partial H}{\partial E}}{\frac{\partial D}{\partial E}} \text{ (by chain rule and implicit differentiation)} \tag{D.16}$$

$$= \frac{-(\epsilon_{Booth}(E) + E\epsilon'_{Booth}(E))E}{\epsilon_{Booth}(E) + E\epsilon'_{Booth}(E)} \text{ (via Equation (D.15))} \tag{D.17}$$

$$= -E, \tag{D.18}$$

$$\text{and } \frac{\partial H}{\partial \phi} = -4\pi\rho, \text{ (via Equation (D.15))} \tag{D.19}$$

as desired. Rewriting the equations of motion (D.9) and (D.10) as $\frac{d\phi}{dx} = -E$ and $\frac{dD}{dx} = -4\pi\rho$ proves that the Hamilton's formalism yields the modified Poisson-Boltzmann equation for the case of dielectric saturation. Accordingly, the conservation principle $H(D, \phi) = const$ with H given in Equation (D.14) is indeed equivalent to the first integral in Equation (3.21) on Page 38 that was derived by the Beltrami's identity.

Dielectric Decrement

In the case of dielectric decrement, the Hamiltonian is

$$H = \frac{(\epsilon_w - 2\alpha\rho_+)E^2}{2} - \frac{2c_\infty(4\pi)}{\beta\nu} \ln(1 - \nu + \nu e^{-\frac{\alpha\beta}{8\pi}E^2} \cosh(ze\beta\phi)). \tag{D.20}$$

Again, utilizing the fact that $E = \frac{D}{\epsilon_{\text{dec}}}$, where D is now a function of E and ϕ, Hamilton's equations give:

$$\frac{\partial H}{\partial D} = \frac{\frac{\partial H}{\partial E}}{\frac{\partial D}{\partial E}} \text{ (by chain rule and implicit differentiation)} \tag{D.21}$$

$$= -\frac{-E\left(\epsilon_w - 2\alpha\rho_+\right) + E^2\alpha\frac{\partial \rho_+}{\partial E}}{\epsilon_w + \alpha\rho_+ + \frac{\partial \rho_+}{\partial E}} \text{ (from Equation (D.20))} \tag{D.22}$$

$$= -E, \text{(from Equation (3.28) on Page 39)} \tag{D.23}$$

$$\text{and } \frac{\partial H}{\partial \phi} = \frac{\partial H}{\partial E}\frac{\partial E}{\partial \phi} + \frac{\partial H}{\partial \phi} \tag{D.24}$$

$$= -4\pi\rho, \text{ (from Equation (D.20))} \tag{D.25}$$

as desired. The conservation relation $H(D, \phi) = \textit{const}$ with H given in Equation (D.20) is indeed equivalent to the first integral in Equation (3.26) on Page 39 for the case of dielectric decrement.